Dissertation thesis study:

SOLPS-ITER simulations of the COMPASS tokamak

Ing. Kateřina Hromasová

Supervisor: Mgr. Jakub Seidl, Ph.D.
Specialist supervisor: Mgr. Michael Komm, Ph.D.

March 31, 2021

Contents

Disclaimer

Owing to health problems which sprang up a few weeks before the completion of this study, this text is rough and unfinished at many places. It is a product of 2.5 years of hard efforts, so it is regrettable that it comes to you in a form which does not do its content and intent justice. However, I firmly believe that it fulfils its basic task — demonstrating my previous PhD progress and outlining my future goals.

Chapter 1

Introduction

Humanity's energy demands are rising exponentially as the average quality of life improves. Unfortunately, our chief energy source — fossil fuels — has a lasting impact on the Earth's climate and its supply is intrinsically limited. Consequently, new energy sources are sought. Among them is thermonuclear fusion.

There are several concepts of the fusion reactor, such as the tokamak, the stellarator and the inertial fusion reactor, but they all share a fundamental concern: heat exhaust. The fusion fuel, a 1:1 mixture of deuterium and tritium, burns in the plasma state at temperatures of approximately 150 million K. To achieve this temperature, the plasma is heated both externally by heating systems and internally by fusion reactions. From the conservation of energy it follows that the plasma concurrently releases the same amount of energy onto the walls of its container. This energy must be safely exhausted from the reactor without threatening the integrity of its internal components. This brings many challenges, some unique to one type of reactor, others shared. Reactors with inertially confined plasmas feature pulsed fusion power, so they must safely contain what amounts to several explosions in the reactor chamber per second. Reactors with magnetic confinement, on the other hand, face problems with heat flux localisation where the field lines connect the reactor chamber to the hot edge of the confined plasma. Ultimately, failing to resolve the problems tied to heat exhaust will shorten the reactor lifespan so drastically that building fusion power plants will not be economically feasible.

This study focuses on the steady-state heat fluxes under nominal tokamak operation and explores the energy transport occurring in the edge plasma region. We present simulations of the COMPASS tokamak, operated by the Institute of Plasma Physics in Prague, using the transport code SOLPS-ITER and gauge the modelled transport characteristics. In the future, these simulations will be expanded into impurity-seeded detachment models of the COMPASS edge plasma, elucidating the dynamics of radiative losses by impurities and, possibly, the effect of cross-field drifts on the divertor plasma parameters.

1.1 Heat exhaust in tokamak reactors

The energy and particle transport in the tokamak edge plasma is characterised by the interplay between the parallel and cross-field transport. Since charged particles can move freely along the magnetic field lines but their cross-field motion is severely hindered, the parallel transport is orders of magnitude more efficient than the cross-field transport. As a consequence, the parallel and cross-field transport can be, to a good degree of accuracy, decoupled and solved independently. The equations of parallel and cross-field physics are then naturally described using the field-aligned coordinates $[\|, r, \perp]$ rather than the usual torodial $[\phi, r, \theta]$ or cyllindrical $[\phi, R, Z]$ coordinates. The parallel coordinate $\|$ points along the magnetic field lines, the radial coordinate r points away from the magnetic axis and the bi-normal coordinate $\perp$ is perpendicular both to $\|$ and r. One can write that an arbitrary flux $\mathbf{\Gamma}$ associated with charged particles will usually satisfy $\Gamma_\| \gg \Gamma_r \approx \Gamma_\perp$.

The key role of edge plasma transport in the issue of heat exhaust can be illustrated by the following simplified calculation. Consider the baseline ITER scenario with 500 MW of fusion power and 50 MW of heating power. The shape of the ITER vessel may be approximated with a toroid whose major radius is $R = 6$ m and whose poloidal cross-section is an ellipse with the semi-major axis of $a = 3.5$ m and the semi-minor axis of $b = 2$ m. The area of this toroid is 663 m^2. 80 % of the fusion power is carried by neutrons, whose energy is deposited volumetrically and therefore does not contribute to the surface heat load calculation. Suppose that a third of the remaining 150 MW of power, introduced by heating systems and alpha particles, is released in the form of isotropic radiation. [1] This is absorbed by the chamber surface, introducing the heat load $q = 50$ MW/663 m$^2 = 0.075$ MW.m^{-2}. The remaining 100 MW is carried predominantly by the parallel transport and deposited in a narrow strip along the strike lines. The heat flux patterns are shown in Fig. 1.1. The plasma-wetted area may be estimated as [2, Sec. 6]

$$A_{wet} = 2\pi R_{sp} \lambda_q^{(OMP)} f_x, \tag{1.1}$$

where $R_{sp} \approx 6$ m is the strike point major radius, $\lambda_q^{(OMP)} = 3.4$ mm is the heat flux fall-off length for ITER H-mode at the outer midplane (OMP) [1, Sec. 3.1.2] and $f_x = 9$ is the poloidal magnetic flux expansion factor [2]. Counting both strike lines, the total plasma-wetted area is meager 2.31 m^2, which results in the divertor target heat load $q = 43$ MW.m^{-2}. By comparison, the heat flux on the surface of the Sun is 63 MW.m^{-2} and the highest steady-state heat flux the ITER divertor can accommodate in the long-term is 16 MW.m^{-2}. [1] This is one

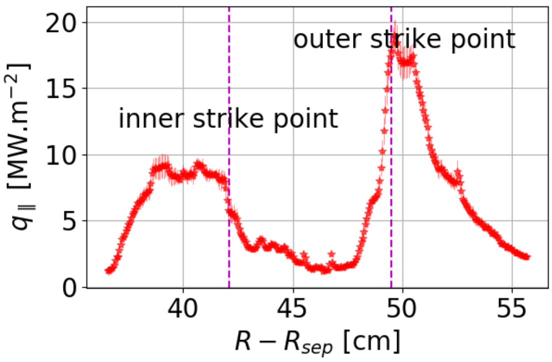

Figure 1.1: Heat flux deposition pattern along the target of the COMPASS tokamak. Measured by infrared thermography, discharge #17588.

of the reasons why the ITER divertor targets are tilted vertically, allowing the heat flux to distribute over a much larger area. For the impact angle $\alpha = 4.5\,^{\circ}$ [1], the factor is $1/\sin\alpha = 13$ and the average strike line heat load decreases to $q = 3.3$ MW.m^{-2}. There are many uncertainties and omissions in this calculation; it neglects $q_{\parallel}$ peaking near the strike points, radiation in the edge plasma and the shaping of the divertor tiles. However, it retains its illustrative value. A fraction of the power released from the plasma crosses the separatrix in the form of charged particles, is transported to the divertor targets via edge transport and finally deposited on a very small area near the divertor strike lines. One of the main goals of the edge transport research is to control this power channel and ascertain that it does not cause unacceptable damage to the divertor targets. [3]

The primary damage hazards which hot plasma particles pose to the divertor targets are recrystallisation and erosion. [1] The often-quoted melting is diminished by the choice of tungsten ($T_{melt} = 3400$ °C) as the divertor surface material, and it only occurs under off-normal events such as disruptions or unmitigated ELM instabilities. [4] Tungsten recrystallisation occurs when the monoblock surface temperature rises to approximately 1300-1700 °C [5] and it results in decreased thermal shock resistance and increased brittleness. When the layer of recrystallised tungsten reaches the thickness of ~ 2 mm, the thermal stress from further heating and cooling cycles causes it to crack. [6] Divertor target erosion is caused by prolonged periods of target sputtering, where high-energy ions knock a tungsten atom out of the target and into the plasma. The atom can be promptly ionised and, owing to Larmor rotation, redeposited on the target, but since ion fluxes tend to be localised and tungsten Larmor radii are large, erosion patterns form along the strike lines nevertheless. Both recrystallisation and erosion are long-term processes. They will slowly occur during the steady-state reactor operation and they will be exacerbated by the presence of ELMs. To ensure sufficient divertor lifetime, these processes must be mitigated by constraining the operating space of the divertor plasma parameters.

According to [7], the divertor can be sufficiently protected from recrystallisation and erosion under the following conditions: (i) the target electron temperature T_{et} does not exceed 10 eV, and (ii) the target electron density n_{et} attains an optimal value, which is of the order $\sim 10^{21}$ m^{-3} and depends on T_{et} and the field line incidence angle α. To test if these criteria can be met in ITER, one may perform a simple calculation using the two-point model (2PM). [8, Eq. (5.4)-(5.6)] We use the basic form of the 2PM, in which the total pressure is assumed constant along the flux tube (zero momentum losses) and all of the upstream energy is exhausted through the target sheath (zero power losses). To predict the target plasma parameters, the model requires the upstream (electron) density n_u, the parallel heat flux density $q_\parallel$ and the flux tube length L as input. SOLPS-ITER modelling of ITER H-mode indicates that the separatrix electron density is approximately $n_u = 3.5 \times 10^{19}$ m^{-3}. [9, Fig. 6.4] The parallel heat flux density can be calculated as $q_\parallel = P_{SOL}/A_\parallel$, where $P_{SOL} = 50$ MW is the power transported toward the outer target and

$$A_\parallel = 4\pi R \lambda_q^{(OMP)} \frac{B_\theta}{B} \tag{1.2}$$

is the area of the flux tube adjacent to the separatrix. [8, Eq. (5.59)] Here $R = 8.2$ m is the outer midplane major radius, $\lambda_q^{(OMP)} = 3.4$ mm is the heat flux fall-off length [1] and $B_\theta = 1.3$ T and $B = 4.2$ T [10] are the outer midplane poloidal and total magnetic fields, respectively. This yields $A_\parallel = 0.11$ m^2 and $q_\parallel = 461$ MW.m^{-2}. The flux tube length is $L = 40$ m. [10]. Injecting these values into 2PM, one obtains the upstream (electron) temperature $T_u = 187$ eV, the target temperature $T_t = 164$ eV and the target density $n_t = 2.0 \times 10^{19}$ m^{-3}. Evidently these values are not compatible with the ITER divertor, as the temperature is much too high and the density much too low. The reason for this result is the absence of momentum and power losses in the calculation. The other simplifying assumptions, such as the absence of impurity species, $T_i = T_e$ or neglecting the flux expansion, do not impact the result nearly as heavily as the absence of losses. This calculation illustrates the key role of momentum and power losses in the edge plasma. It has been shown that only a substantial reduction of the target plasma pressure accompanied by strong dissipation of power by radiation can usher in favourable divertor conditions in a burning plasma. [1] The key question of steady-state divertor operation in the desirable parameter window then becomes: What physics govern momentum and power losses in the edge plasma?

Experimental and modelling evidence suggest that the momentum and power loss factors,

$$f_{mom} = 1 - \frac{p_t}{p_u} \qquad (1.3) \qquad\qquad f_{pow} = 1 - \frac{q_{\parallel t} A_{\parallel t}}{q_{\parallel u} A_{\parallel u}} \qquad (1.4)$$

where p is the total pressure, are highly correlated with the target electron temperature T_{et}. [7] The evidence is especially compelling for pressure losses in cold dense plasmas, where it has been shown that the majority of the flux tube momentum is lost in a thin layer above the surface due to interaction of ions with neutral molecules. [11] This process is governed mainly by temperature and thus it is even possible to give a formula for $f_{mom}(T_{et})$. [12, Eq. (17)] Despite our lack of clear-cut physical understanding of *why* the losses are so dependent on T_{et}, it is certain that the target temperature is a pivotal quantity in edge momentum and power loss physics.

The coexistence of $\sim$ 150 eV upstream temperature, consistent with an H-mode pedestal needed for high fusion performance, and $\sim$ 5 eV target temperature, compatible with a long divertor life time, is the subject of study of edge transport regimes. The fundamental observation of the edge transport regimes is that the plasma ability to transport energy along the field lines is mediated mostly by electron heat conduction $q_\parallel = -\chi_e \mathrm{d}T_e/\mathrm{d}s$, and therefore it increases strongly with plasma temperature, $\chi_e = \chi_0 T_e^{5/2}$. This means that in a plasma which has, on average, high temperature, a small parallel gradient of T_e will suffice to transport P_{SOL} to the target. Conversely, in a cooler plasma a large parallel gradient of T_e will form to carry the same $q_\parallel$. The result of the first situation is isothermal, high-temperature SOL — the *sheath-limited regime*; the second situation will result in a SOL where upstream may be hot but the target is substantially (at least factor-of-three) cooler — the *conduction-limited regime*.[1] The loss-less example of ITER SOL given above was in the sheath-limited regime, with similar upstream and target temperatures. Evidently, the conduction-limited regime would be much more desirable as it allows the coexistence of high upstream and low target temperature. To transition into this regime in a given magnetic geometry, we would have to lower the overall SOL temperature. This can principally be done in three ways: increasing the upstream density (e.g. using gas puff), decreasing the upstream heat flux density (by lowering the fusion power or allowing more radiation in the core) or introducing/increasing momentum and power losses. Since the edge density is limited by the Greenwald limit and decreasing P_{SOL} degrades plasma performance, substantial parallel temperature gradients in the ITER SOL will be

[1]The regime names refer to the most prominent feature of the parallel energy transport. In the sheath-limited regime, it is the target sheath, which allows plasma cooling at the rate $q_\parallel = \gamma T_e n_e c_s$ where $\gamma \approx$ 7-11 is the total sheath heat transmission coefficient, $c_s = \sqrt{e(T_i + T_e)/m_i}$ is the sound speed and all of the quantities are measured at the sheath entrance. In the conduction-limited regime, it is the electron energy conduction with its strong dependence on the local electron temperature.

achieved by momentum and power losses, which cause the total plasma pressure to drop radically at the target compared to the upstream and which allow most of the power conducted through the SOL to be dissipated as radiation before it reaches the target. The regime where momentum and power losses are so strong that $T_{et} < 10$ eV across the entire divertor target is called *detachment*. [7]

Basic understanding of divertor detachment physics is listed in the recent review [1] as a key question regarding ITER divertor operation. Areas where further research is needed comprise not only the link between target quantities and distributed pressure/power losses, but also the precise role/importance of volume recombination in reducing target ion flux and the behaviour of upstream density with impurity concentration. Experimentally divertor detachment has been studied on a number of machines, but diagnostic limitations, involving for instance probe measurements at temperatures below 5 eV, measurements of the neutral pressure or measurements of upstream T_i, typically allow only a certain degree of insight. For this reason, experiments are often supplemented by extensive modelling efforts. To date, the work horse of detachment modelling have been transport codes, which accurately capture the interplay between parallel and cross-field physics, atomic and molecular processes (the main cause for momentum and power losses) and the plasma-wall interaction. To further the understanding and optimise the design of the ITER divertor, the SOLPS-ITER code has been developed by the ITER organisation. [13] In my future PhD thesis, SOLPS-ITER will used to model the divertor detachment in the COMPASS tokamak and explain the transport and divertor characteristics found experimentally.

1.2 Transport codes

Tokamak transport codes describe the plasma as a mix of charged ion fluids permeated by a weightless electron fluid, confined by a static magnetic field and surrounded by boundary regions. Their variables are the velocity-space-averaged moments of the velocity distribution function $f(t, \mathbf{r}, \mathbf{v})$: particle density $n_a(t, \mathbf{r})$, temperature $T_a(t, \mathbf{r})$ and flow velocity $\mathbf{u}_a(t, \mathbf{r})$ of each particle species a at time t and position $\mathbf{r}$, as well as the plasma potential $\Phi(t, \mathbf{r})$. The spatio-temporal evolution of these variables is governed by the transport equations, which are usually a variation of the Braginskii equations. [14] Depending on the user input, transport codes can provide steady-state solutions of the plasma state or its temporal development. There are many different implementations of transport codes, from the 1D SOLF1D [15], 1.5D ASTRA [16], 2D SOLEDGE2D [17] to the fully 3D EMC3 [18], and they are often supplemented with a Monte Carlo code for neutral particles modelling such as EIRENE [19].

The main competence of transport codes is, as the name suggests, transport. In the case of tokamak edge models, this can be the transport of impurities (impurity sputtering, radiation and exhaust), energy (heat exhaust) or the complex interplay of all of the above (atomic and molecular physics, divertor detachment). Transport codes, however, also have a number of limitations. In this section we will discuss two main transport code problems: the diffusive ansatz and the assumptions under which Braginskii equations were derived. To fully understand the latter, we will show the derivation of the fluid equations and discuss the Braginskii closure. The section will conclude with a brief contemplation of the transport code strengths and weaknesses.

1.2.1 The diffusive ansatz for the radial transport

It is known that the tokamak edge radial transport is largely turbulent. [20] However, self-consistent turbulence is so computationally demanding to model that transport codes instead assume that the particle and energy fluxes are purely diffusive, that is, described by the Fick's law:

$$\Gamma_r = -D\frac{\mathrm{d}n}{\mathrm{d}r} \qquad (1.5) \qquad\qquad q_r = -\chi\frac{\mathrm{d}T}{\mathrm{d}r} \qquad (1.6)$$

This is sometimes supplemented by a convective flux nu_r, allowing for inward transport of e.g. impurities. The assumption that the radial transport can be described by Fick's law is called the diffusive ansatz.

Evidently, the diffusive ansatz captures the physics of the tokamak edge poorly. It is a local description, where the flux at one point in space and time only depends strictly on the plasma parameters at that spatial and temporal point. Turbulent transport, in contrast, typically stems from events which happened prior and elsewhere, such as the formation of turbulent structures in a region susceptible to the interchange instability. Considering the irreconcilable difference between these two descriptions, it is surprising that in transport codes the diffusive ansatz yields results good enough to become widely used in the fusion community. In a recent work [21], Manz et al have suggested that this might be because the intermittent turbulent transport, in fact, averages to a diffusion-like transport at large time scales. By modelling ballistically propagating turbulent structures, they have recovered exponentially decaying SOL density profiles and shown that the resulting particle flux is diffusion-like. Its "diffusion" coefficient then relates directly to the turbulent structures properties, the typical radial velocity u_b and the correlation time τ of the radial velocity:

$$D_n = u_b^2\tau \qquad (1.7)$$

Let us calculate this diffusion coefficient for the tokamak COMPASS conditions. We employ the outer midplane reciprocating probe measurements in the

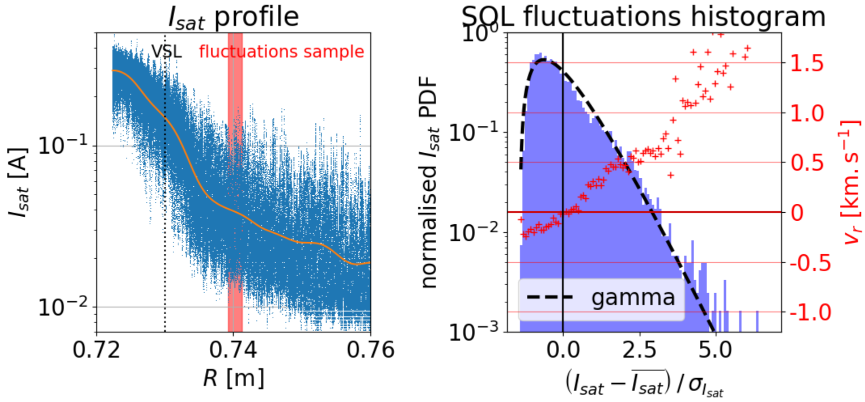

Figure 1.2: Ion saturated current I_{sat} profile in the COMPASS discharge #6878 and the histogram of its fluctuations approximately 1 cm outside the velocity shear layer (VSL, $E_r = 0$). The radial velocity (red crosses) was calculated for each bin of the I_{sat} signal, so it corresponds to the velocity of turbulent structures of various sizes.

D-shaped L-mode COMPASS discharge #6878. (Further information on COMPASS diagnostics is given in [22].) The probe delivers radial profile measurements of the radial plasma velocity v_r. This quantity is estimated from the simultaneous measurements of two poloidally spaced ball-pen probes, which measure the plasma potential Φ. [23] From their respective potentials and distance d, the poloidal electric field may be calculated.

$$E_p = \frac{\Phi_1 - \Phi_2}{d} \tag{1.8}$$

Dividing this by the total magnetic field, one obtains the turbulent structure radial $E \times B$ velocity

$$v_r = \frac{E_p}{B}. \tag{1.9}$$

In experiment, blob transport is not exactly ballistic, since the blobs slow down as their internal electric field is dissipated. This is one of the limitations of the calculations presented in this section and contributes to the results being rough estimates.

Figure 1.2 demonstrates the turbulent nature of the SOL radial transport. On the left, there is the profile of the ion saturated current I_{sat}, which is measured by a Langmuir probe biased to -240 V on the same probe head as the two ball-pen probes. Only the reciprocating probe movement inward is plotted. As is typical for the edge plasma, the I_{sat} profile decays exponentially, faster in the near SOL and slower in the far SOL. Approximately 1 cm outside the velocity shear layer (VSL,

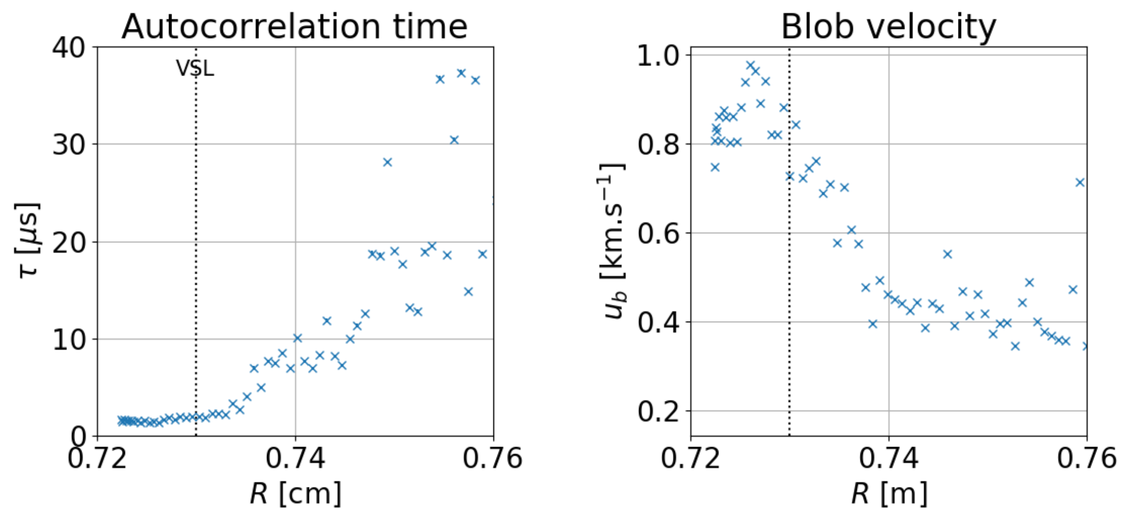

Figure 1.3: Estimation of turbulence properties in the COMPASS discharge #6878: autocorrelation time τ and blob velocity u_b and the particle diffusion coefficient $D_n = u_b^2\tau$. The velocity shear layer (VSL, $E_r = 0$) position is plotted in black.

$E_r = 0$), a 3ms window was chosen for sampling the I_{sat} and v_r fluctuations.[2] On the right, the I_{sat} histogram is plotted. As expected, a positively skewed distribution emerges, reminiscent of the gamma function as argued in [24]. For each I_{sat} histogram bin (plasma fluctuation of a certain magnitude), the average v_r was calculated and plotted into the same graph in red. One observes that positive fluctuations (the so-called blobs) propagate outward while the negative fluctuations ("holes") propagate inward, and that larger fluctuations move faster. Plotting the same histogram for other radial positions suggests that this is valid in the entire edge plasma (not shown here). This is consistent with the process of interchange turbulence. [20]

To estimate the blob velocity u_b and the correlation time τ from the v_r measurements, we adopt the following approach. We calculate the blob velocity u_b inside consecutive 1ms windows as the standard deviation of the radial velocity. This is in accord with [21], where $u_b^2 = C_0$ is the peak value of the v_r autocorrelation function, that is, the v_r variance. The correlation time τ is calculated inside the same consecutive 1ms windows by fitting the peak of the v_r autocorrelation function with the exponential $\mathrm{e}^{-|t|/\tau}$. The resulting profiles of blob velocity u_b and correlation time τ are plotted in figure 1.3. The correlation time spans an order of magnitude from 2 μs to 40 μs, indicating a large number of rapidly exchanging turbulent structures inside the VSL and a smaller number of longer lasting events in the far SOL. The blob velocity peaks at 1 km.s^{-1} inside the VSL and then quickly

[2] The velocity shear layer is used in favour of the separatrix position, which is rather uncertain.

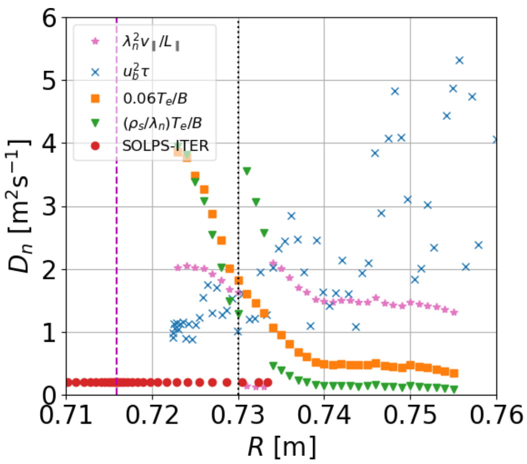

Figure 1.4: Particle diffusion coefficient D_n calculated with a number of techniques (see text).

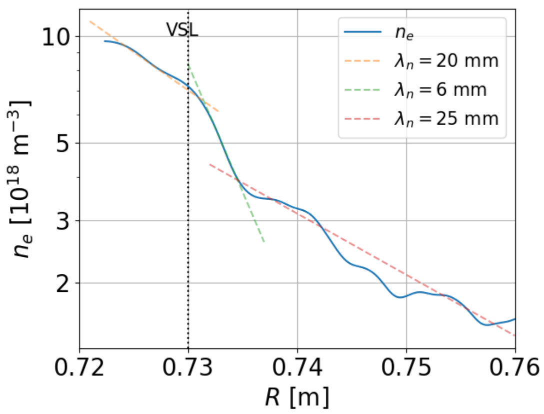

Figure 1.5: Electron density n_e profile at the outer midplane, COMPASS discharge #6878. Dashed lines denote different fall-off lengths.

decays to 0.4 km.s^{-1}, where it stabilises in the far SOL. These results support the idea of turbulent structures being mixed and torn in the VSL and then spreading through the SOL while slowly waning due to parallel losses.

To give context to the resulting $D_n = u_b^2\tau$, D_n is additionally calculated using the three methods discussed by [21]:

- the zeroth-order approximation of Fick's law $D_n = \lambda_n^2 v_\parallel / L_\parallel$, where λ_n is the density fall-off length, $v_\parallel = 0.2c_s = 0.2\sqrt{2eT_e/m_i}$ is the upstream parallel plasma flow velocity, a fraction of the ion sound speed, and $L_\parallel$ is the connection length to the outer target (calculated by EFIT)
- the Bohm diffusion coefficient $D_n = 0.06T_e/B$
- the gyro-Bohm diffusion coefficient $D_n = (\rho_s/\lambda_n)T_e/B$ where $\rho_s = \sqrt{m_i T_e/e}/B$ is the ion gyroradius

In all of the above, temperature is given in eV. The density fall-off length λ_n was approximated by a step function based on experimental n_e data, see figure 1.5. The electron density was calculated from horizontal reciprocating probe data as $n_e = I_{sat}/0.5eA_{probe}c_s$, where $A_{probe} = 4.9$ mm^{-2} is the effective Langmuir probe collecting area. The electron temperature was measured using the BPP-LP method. Combining these measurements, one may gain some insight into the expected D_n values and profile shape.

The perpendicular diffusion coefficients D_n profile is plotted in figure 1.4. The various methods yield an appreciable disagreement. The Bohm and gyro-Bohm diffusion coefficients fall from 4 m^2s^{-1} inside the VSL to 0.1-0.4 m^2s^{-1} in the far SOL. This trend is opposite to that calculated from turbulence properties. $D_n = u_b^2\tau$ rises from 1 m^2s^{-1} inside the VSL to approx. 4 m^2s^{-1} in the far SOL, indicating worse particle confinement outside the VSL. This result is similar to the low-density case studied in [21]; however, the COMPASS values of D_n are much larger than in ASDEX-Upgrade. Finally, complete disagreement is reached upon comparing these techniques to the perpendicular diffusion coefficient employed in SOLPS-ITER modelling of the COMPASS discharge #17588[3], $D_n = 0.2$ m^2s^{-1}. This value was reached by iterative model-experiment fitting, where it was found that a flat profile of D_n was sufficient to reproduce experimental profiles. It was attempted to utilise the turbulence-based D_n profile in the simulation: 1 m^2s^{-1} inside the separatrix and linearly rising in the SOL. However, this made experiment-code fit fall apart via the rise of the separatrix density. At this stage of research, it is not possible to reconcile these values of D_n within a self-consistent framework as done in [21]. The value of the perpendicular anomalous diffusion coefficient D_n at COMPASS is uncertain and should be subject to further research.

To sum up this section, the diffusive ansatz remains a difficult topic in transport code modelling. Anomalous diffusion is not the physics basis of the edge plasma radial transport, even if correspondence can be found with the time-averaged turbulent transport. In practice, transport codes can retain the experimental n_e profile shape by using ad-hoc D_n values, tailored to the specific simulation. This, however, obscures the physical meaning of the parameter outside the simulation. Hopefully, further insight can be reached by investigating discharges with better diagnostics coverage.

1.2.2 Transport equations

Transport equations lie at the heart of every transport code. They prescribe the plasma parameters, density n_a, temperature T_a and velocity u_a of each species a as well as the plasma potential Φ and provide formulas how to calculate all other quantities (drift velocities, heat fluxes, currents etc.) from them. Most sets of transport equations stem from the Braginskii equations [14], which describe a fully ionised plasma consisting of ions with the charge Z and electrons. The Braginskii equations were later generalised for multiple ion species. [25, 26] In this section, we follow the derivation of the fluid equations and discuss the Braginskii closure in order to grasp better the limitations of transport codes.

[3] In discharge #17588, reciprocating probe measurements are not available. Consequently, this section is a proof of concept rather than a basis for direct employment of experimental D_n in a SOLPS-ITER simulation. However, it is unlikely that the diffusion coefficient changes by orders of magnitude between COMPASS discharges.

The kinetic equation

The fluid equations are derived from the kinetic equation (also called the Boltzmann equation), which describes a population of interchangeable particles, such as electrons, C^{1+} atoms or NH_3 molecules, by prescribing the time evolution of their distribution function $f(t, \mathbf{r}, \mathbf{v})$. The distribution function f has 7 variables: time t, spatial position $\mathbf{r}$ and velocity $\mathbf{v}$.[4] The differential $f(t, \mathbf{r}, \mathbf{v})\mathrm{d}\mathbf{r}\mathrm{d}\mathbf{v}$ expresses the number of particles positioned inside the infinitesimal volume $(\mathbf{r}, \mathbf{r} + \mathrm{d}\mathbf{r})$ which have velocities within the interval $(\mathbf{v}, \mathbf{v} + \mathrm{d}\mathbf{v})$ at time t.

Each species a of interchangeable particles has its own distribution function f_a and the individual distributions influence each other via elastic and inelastic collisions. Generally speaking, elastic collisions preserve the number of particles of each species (the particles only exchange momentum and the associated kinetic energy), while inelastic collisions change the internal energy of the particles and therefore convert particles of one species into another. An example of an inelastic collision is charge exchange

$$D^{*1+} + D^0 \to D^{*0} + D^{1+}, \tag{1.10}$$

where the star denotes a high energy or excited particle. In total, this reaction sees the "destruction" of one neutral deuterium atom in the base state, "creation" of one excited neutral deuterium atom and the loss of energy of a deuterium ion. The distribution functions of charged particles are also affected by electromagnetic fields, which can exchange momentum and energy with the particles.

The kinetic equation of species a reads [27, Eq. (2.5)]:

$$\frac{\partial f_a}{\partial t} + v_\beta \frac{\partial f_a}{\partial x_\beta} + \frac{F_{a\beta}}{m_a}\frac{\partial f_a}{\partial v_\beta} = \frac{\partial f}{\partial t}_{coll} \tag{1.11}$$

where Einstein summation is carried out over the subscript β. $\frac{\partial}{\partial x_\beta}$ is the spatial derivative in the direction β, $F_{a\beta} = F_{a\beta}(t, \mathbf{r}, \mathbf{v})$ is the force acting upon species a in the direction β, m_a is the particle mass of species a and $\frac{\partial f}{\partial t}_{coll} = \frac{\partial f}{\partial t}_{coll}(t, \mathbf{r}, \mathbf{v})$ is the collision term of species a. The particular force form depends on the species; for instance, charged particles experience the Lorentz force $q_a(\mathbf{E} + \mathbf{v} \times \mathbf{B})$ most prominently. The collision term $\frac{\partial f}{\partial t}_{coll}$ describes changes in the distribution function caused by collisions with particles of all species in the system, including species a. To sum up the meaning of the equation, the time evolution of the distribution function $\frac{\mathrm{d}f_a}{\mathrm{d}t}$ is moderated by particle collisions.

The kinetic equation is an accurate and useful mathematical description of a

[4] Rotational degrees of freedom, which can be important in the description of molecules, are neglected here.

plasma, even if it does not capture the motion of each individual particle.[5] It can be solved numerically using kinetic codes, but this is very time-consuming due to its large 7D variable space. In many applications, the fluid description is adopted instead. The fluid approach removes 3 of the 7 variables — the velocity $\mathbf{v}$ — at the cost of losing the ability to describe phenomena stemming from the velocity distribution, such as sheath physics, non-Maxwellian parallel heat fluxes, the Landau damping or most wave-particle interactions. The fluid equations are an adequate substitute for the kinetic equations if the kinetic processes aren't expected to play a large role in the modelled plasma physics or their effect can be simulated ad hoc (using heat flux limiters, sheath boundary conditions etc.).

Fluid equations are typically derived by taking three *moments* of the kinetic equation. A moment in kinetic plasma physics is similar to a moment in statistics; the distribution function is multiplied by a power of one of its variables and then averaged over this variable. The three resulting equations represent the three basic laws of conservation, conservation of particles, momentum and energy, and they lay the ground for transport codes.

Zeroth moment of the kinetic equation: the continuity equation

The zeroth moment of the kinetic function, where the multiplication factor is $v^0 = 1$, is the particle conservation equation, also called the continuity equation:

$$\frac{\partial n_a}{\partial t} + \frac{\partial}{\partial x_\beta}(n_a u_{a,\beta}) = S_a, \tag{1.12}$$

where the particle density

$$n_a(t, \mathbf{r}) = \int_{\mathbb{R}^3} f_a(t, \mathbf{r}, \mathbf{v})\mathrm{d}\mathbf{v} \tag{1.13}$$

is the zeroth moment of the distribution function in the velocity space, the flow velocity

$$\mathbf{u}_a(t, \mathbf{r}) = \frac{1}{n_a(t, \mathbf{r})} \int_{\mathbb{R}^3} \mathbf{v} f_a(t, \mathbf{r}, \mathbf{v})\mathrm{d}\mathbf{v} \tag{1.14}$$

is the first moment of the distribution function in the velocity space. The particle source/sink term $S_a(t, \mathbf{r})$ then accounts for inelastic collisions as well external influences (gas puff, particle recycling etc.). The continuity equation says that the

[5] Not nearly all statistical properties of a particle system are captured by the kinetic equation. The distribution function is averaged over a large number of particles and time span comparable to the time of flight and therefore doesn't capture thermal fluctuations. The terms in the kinetic equation are likewise "smoothed"; the force $\mathbf{F}_a$ doesn't contain the microfields generated when particles come into close vicinity of one another and these effects are rather moved to the collision term $\frac{\partial f}{\partial t}_{coll}$. [14]

local changes in density n_a can be caused by the particles flowing elsewhere as they are carried by the flow velocity $\mathbf{u}_a$, or by locally adding or removing particles of species a.

The need for closure

The continuity equation shows a fundamental property of the moment equations: to describe one moment of the distribution function (here n_a), knowledge of the next moment is required (here $\mathbf{u}_a$). Incidentally, the next moment is always the flux of the prior: the flow velocity $\mathbf{u}_a$ is the flux of density n_a, the pressure tensor $p_a\delta_{\alpha\beta} + \pi_{a,\alpha\beta}$ is the flow of momentum $m_a\mathbf{u}_a$ etc. If one takes an infinite number of moment equations, the resulting system is equivalent to the original kinetic equation. In the fluid approach, however, usually only the first three moment equations are considered: the continuity equation (prescribes the density n_a), the equation of motion (prescribes the flow velocity $\mathbf{u}_a$) and the energy transport equation (prescribes the temperature T_a). To prescribe the third moment of the distribution function (energy flux $\mathbf{q}_a$), one does not use the third moment equation but rather an external formula which prescribes the flux in terms of n_a, $\mathbf{u}_a$, T_a and parameters such as heat conductivities or viscosities. A set of additional assumptions and formulas which substitutes all remaining moment equations and makes the lower moment system self-sufficient is called a *closure*.

Fluid equations closures can be empirical (such as Fourier's law) or derived from the lower moment equations using particular assumptions. In the Braginskii equations, for example, one assumes a particular ordering of scales which implies that the distribution function is locally Maxwellian, its shape determined by n_a, $\mathbf{u}_a$ and T_a. This allows the calculation of all the required moments and establishes n_a, $\mathbf{u}_a$ and T_a (along with the plasma potential Φ) as the principle variables of the fluid plasma description.

The fluid equations closure is one of the defining features of a transport code built upon these equations, since it ushers in further limitations to the modelled plasma physics. If, for instance, the closure assumes that electrons undergo many collisions in the SOL before they are deposited on the divertor target (their mean free path is much smaller than the connection length), the transport code employing it will predict unphysically high electron heat fluxes in low collisionality SOL plasmas. Many closures have been published (e.g. [25] and [26]), including the Braginskii closure which gave name to the Braginskii equations. In section 1.2.2, the Braginskii equations will be discussed to gauge the limitations of the simulations presented herein.

First moment of the kinetic equation: the equation of motion

(For clarity, in the rest of the chapter the subscript a will be omitted. The equations still, however, describe solely the particles of a particular species a.)

Taking the first moment of the kinetic equation by multiplying it with $m\mathbf{u}$ and averaging over the velocity space, one obtains the momentum conservation equation, also called the equation of motion or the momentum transport equation. It is a vector equation which applies individually for each component of the momentum $m\mathbf{u}$, so we write its α component:

$$mn\left(\frac{\partial}{\partial t}+u_\beta\frac{\partial}{\partial x_\beta}\right)u_\alpha=-\frac{\partial p}{\partial x_\alpha}-\frac{\pi_{\alpha\beta}}{\partial x_\beta}+qn\left(E_\alpha+(\mathbf{u}\times\mathbf{B})_\alpha\right)+R_\alpha. \tag{1.15}$$

To describe the terms we first define the chaotic velocity component

$$\mathbf{v}'=\mathbf{v}-\mathbf{u}(t,\mathbf{r}). \tag{1.16}$$

With it we can write the scalar pressure

$$p(t,\mathbf{r})=\int_{\mathbb{R}^3}\frac{1}{3}mv'^2f(t,\mathbf{r},\mathbf{v})\mathrm{d}\mathbf{v} \tag{1.17}$$

and the stress tensor

$$\pi_{\alpha\beta}(t,\mathbf{r})=\int_{\mathbb{R}^3}m\left(v'_\alpha v'_\beta-\frac{v'^2}{3}\right)f(t,\mathbf{r},\mathbf{v})\mathrm{d}\mathbf{v} \tag{1.18}$$

which are the two components of the second moment of the distribution function in the velocity space,

$$\int_{\mathbb{R}^3}mv'_\alpha v'_\beta f(t,\mathbf{r},\mathbf{v})\mathrm{d}\mathbf{v}=p(t,\mathbf{r})\delta_{\alpha\beta}+\pi_{\alpha\beta}(t,\mathbf{r}). \tag{1.19}$$

Finally,

$$R_\alpha(t,\mathbf{r})=\int_{\mathbb{R}^3}mv'_\alpha\frac{\partial f}{\partial t}_{coll}(t,\mathbf{r},\mathbf{v})\mathrm{d}\mathbf{v}+R_\alpha^{ext}(t,\mathbf{r}) \tag{1.20}$$

is the mean change of momentum due to collisions with other species and external momentum sources/sinks. Defining the local temperature as

$$T(t,\mathbf{r})=\frac{1}{n_a(t,\mathbf{r})}\int_{\mathbb{R}^3}\frac{1}{3}mv'^2f(t,\mathbf{r},\mathbf{v})\mathrm{d}\mathbf{v}, \tag{1.21}$$

one immediately has

$$p(t,\mathbf{r})=n(t,\mathbf{r})T(t,\mathbf{r}), \tag{1.22}$$

the ideal gas equation. Note that in this notation the unit of temperature are joules and the temperature represents the mean chaotic kinetic energy per particle. The static pressure p then represents the thermal energy density in the plasma.

The meaning of the momentum conservation equation is the following. The density-weighted momentum of species a can change through five means: flows driven opposite to the scalar pressure gradient (isotropic), viscous effects (anisotropic), the external Lorentz force acting on the particles, collisions with other species and external momentum sources and sinks.

Second moment of the kinetic equation: the energy transport equation

Finally, taking the second moment of the kinetic equation, one arrives at the energy conservation (or transport) equation:

$$\frac{\partial}{\partial t}\left(\frac{mn}{2}u^2+\frac{3}{2}nT\right)+\frac{\partial}{\partial x_\beta}\left\{\left(\frac{mn}{2}u^2+\frac{5}{2}nT\right)u_\beta+\pi_{\alpha\beta}\cdot u_\alpha+q_\beta\right\}=qn\mathbf{E}\cdot\mathbf{u}+\mathbf{R}\cdot\mathbf{u}+Q \tag{1.23}$$

Here the heat flux density

$$\mathbf{q}(t,\mathbf{r})=\int_{\mathbb{R}^3}\frac{1}{2}mv'^2\mathbf{v}f(t,\mathbf{r},\mathbf{v})\mathrm{d}\mathbf{v} \tag{1.24}$$

is a component of the third moment of the distribution function f and

$$Q(t,\mathbf{r})=\int_{\mathbb{R}^3}\frac{1}{2}mv'^2\frac{\partial f}{\partial t}_{coll}(t,\mathbf{r},\mathbf{v})\mathrm{d}\mathbf{v}+Q^{ext}(t,\mathbf{r}) \tag{1.25}$$

is the heat generated as a consequence of collisions with other species and external energy sources/sinks.

The meaning of the energy transport equation is the following. The local energy density, composed of the kinetic energy density $\frac{mn}{2}u^2$ and the thermal energy density $\frac{3}{2}nT$ changes due to eight different processes: flux of kinetic energy $\frac{mn}{2}u^2\mathbf{u}$, flux of thermal energy $\frac{5}{2}nT\mathbf{u}$, flux of pressure energy $\overleftrightarrow{\pi}\cdot\mathbf{u}$, heat flux $\mathbf{q}$, the Joule heating $qn\mathbf{E}\cdot\mathbf{u}$, friction with other species $\mathbf{R}\cdot\mathbf{u}$, collisions with other species where kinetic or internal energy is transferred and external energy sources/sinks.

The energy transport equation is commonly taken as the last moment equation among the fluid equations. To close the equation system, it is necessary to find formulas for $\pi_{\alpha\beta}(t,\mathbf{r})$, $\mathbf{q}(t,\mathbf{r})$, $\mathbf{R}(t,\mathbf{r})$ and $Q(t,\mathbf{r})$ in terms of $n(t,\mathbf{r})$, $\mathbf{u}(t,\mathbf{r})$ and $T(t,\mathbf{r})$. In a multi-particle system, the collision terms may, of course, depend on the parameters of other species as well. This is done using the aforementioned closure. As a result, the Braginskii equations are solved for five scalar variables in each species: the particle density $n(t,\mathbf{r})$, the three components of the flow velocity $u_\alpha(t,\mathbf{r})$ and the temperature $T(t,\mathbf{r})$.[6]

[6] Many transport codes including SOLPS-ITER assume toroidal symmetry, which removes

Braginskii closure and the final form of the Braginskii equations

Braginskii derives expressions for $\pi_{\alpha\beta}(t, \mathbf{r})$, $\mathbf{q}(t, \mathbf{r})$, $\mathbf{R}(t, \mathbf{r})$ and $Q(t, \mathbf{r})$ from the kinetic equation by making several assumptions:

- The system evolves on a much slower time scale than the particle collision time.
- Its typical gradient length is much smaller than the particle mean free path.
- The electron mass and inertia can be neglected compared to the ion mass and inertia.
- The only two particle species present in the plasma are singly-charged ions ($Z = 1$) and electrons (the so-called *simple plasma*).
- The plasma is quasineutral, and therefore $n_e(t, \mathbf{r}) = n_i(t, \mathbf{r}) = n(t, \mathbf{r})$.

The first two assumptions allow for solving the kinetic equation for states close to equilibrium. In equilibrium, the distribution function $f = f_0$ is Maxwellian. In states close to equilibrium which meet the first two assumptions, $f = f_0 + \delta f$ is a perturbed Maxwellian where δf is proportional to the gradients of plasma parameters. Specifically, the full solution is:

$$f_a(t, \mathbf{r}, \mathbf{v}) = \left(\frac{m_a}{2\pi T_a(t, \mathbf{r})} \right)^{3/2} n_a(t, \mathbf{r}) \exp \left(-\frac{m_a}{2T_a(t, \mathbf{r})} - (\mathbf{v} - \mathbf{u}_a(t, \mathbf{r}))^2 \right) \tag{1.26}$$

Note that the only parameters in this function are the particle density $n_a(t, \mathbf{r})$, flow velocity $\mathbf{u}_a(t, \mathbf{r})$ and temperature $T_a(t, \mathbf{r})$. This allows for eventually closing the fluid equations system.

Using perturbation analysis to find $f_a(t, \mathbf{r}, \mathbf{v})$ has the peculiar consequence that $\pi_{\alpha\beta}(t, \mathbf{r})$, $\mathbf{q}(t, \mathbf{r})$, $\mathbf{R}(t, \mathbf{r})$ and $Q(t, \mathbf{r})$ are directly proportional to the local plasma parameter gradients. [14, page 213] For instance, the ion heat flux is proportional to ∇T_i. The coefficients of proportionality are called the *transport coefficients* and their exact value depends on the type of closure one employs. All types of closure available within SOLPS-ITER (Braginskii, Balescu [25] and Zhdanov [26]) share the first two assumptions with the Braginskii closure, and thus their expressions for $\pi_{\alpha\beta}$, $\mathbf{q}$, $\mathbf{R}$ and Q share the same functional dependence but can differ in the value of the parallel transport coefficients. [28, Sec. B.2]

Using the ordering of temporal and spatial scales, further described in [14] and [29], separation of the perpendicular and parallel transport scales, the assumption of completely ionised hydrogen plasma ($Z = 1$) and $m_e \ll m_i$, one obtains the following expressions.[7]

The stress tensor $\pi_{\alpha\beta}(t, \mathbf{r})$ has the same form for electrons and ions, differing only in the viscosity coefficients η values. The tensor is symmetric and its 6

one component of $\mathbf{u}$, and prescribe the radial transport in terms of anomalous diffusion and drifts, removing another component of $\mathbf{u}$. This further reduces the variable number.

[7] We use formulas from [30, Sec. 2.3] instead of [14], since the former uses SI units.

independent components can be written using the rate-of-strain tensor,

$$W_{\alpha\beta} = \frac{\partial u_\alpha}{\partial x_\beta} + \frac{\partial u_\beta}{\partial x_\alpha} - \frac{2}{3}\delta_{\alpha\beta}\nabla\mathbf{u}. \tag{1.27}$$

In the orthogonal Cartesian coordinate system $[x, y, z]$ where z is parallel to the magnetic field:

$$\begin{aligned}
\pi_{zz} &= -\eta_0 W_{zz} \\
\pi_{xx} &= -\frac{1}{2}\eta_0\left(W_{xx} + W_{yy}\right) - \frac{1}{2}\eta_1\left(W_{xx} - W_{yy}\right) - \eta_3 W_{xy} \\
\pi_{yy} &= -\frac{1}{2}\eta_0\left(W_{xx} + W_{yy}\right) - \frac{1}{2}\eta_1\left(W_{yy} - W_{xx}\right) + \eta_3 W_{xy} \\
\pi_{xy} &= \pi_{yx} = -\eta_1 W_{xy} + \frac{1}{2}\eta_3\left(W_{xx} - W_{yy}\right) \\
\pi_{xz} &= \pi_{zx} = -\eta_2 W_{xz} - \eta_4 W_{yz} \\
\pi_{yz} &= \pi_{zy} = -\eta_2 W_{yz} + \eta_4 W_{xz}
\end{aligned} \tag{1.28}$$

The ion viscosity coefficients are:

$$\eta_0^i = 0.96 n T_i \tau_i \qquad \eta_1^i = \frac{3}{10}\frac{nT_i}{\omega_{ci}^2 \tau_i} \qquad \eta_2^i = 4\eta_1^i \qquad \eta_3^i = \frac{1}{2}\frac{nT_i}{\omega ci} \qquad \eta_4^i = 2\eta_3^i \tag{1.29}$$

where the ion collision time is

$$\tau_i = 12\pi^{3/2}\frac{\varepsilon_0^2 m_i^{1/2} T_i^{3/2}}{ne^4 \ln\Lambda} \tag{1.30}$$

($\ln\Lambda$ is the Coulomb logarithm) and the ion cyclotron frequency is

$$\omega_{ci} = \frac{eB}{m_i}. \tag{1.31}$$

The electron viscosity coefficients are:

$$\eta_0^e = 0.73 n T_e \tau_e \qquad \eta_1^e = 0.51\frac{nT_e}{\omega_{ce}^2 \tau_e} \qquad \eta_2^e = 4\eta_1^e \qquad \eta_3^e = -\frac{1}{2}\frac{nT_e}{\omega ce} \qquad \eta_4^e = 2\eta_3^e \tag{1.32}$$

where the electron collision time is

$$\tau_e = 3(2\pi)^{3/2}\frac{\varepsilon_0^2 m_e^{1/2} T_e^{3/2}}{ne^4 \ln\Lambda} \tag{1.33}$$

and the electron cyclotron frequency is

$$\omega_{ce} = \frac{eB}{m_e}. \tag{1.34}$$

The electron heat flux consists of two contributions, the heat flux due to friction

$$\mathbf{q}_u^e = nT_e \left(0.71\mathbf{u}_\parallel + \frac{3}{2|\omega_{ce}|\tau_e}\mathbf{b}\times\mathbf{u}\right), \tag{1.35}$$

where $\mathbf{b} = \mathbf{B}/B$, and the thermal heat flux

$$\mathbf{q}_T^e = \frac{nT_e\tau_e}{m_e}\left(-3.16\nabla_\parallel T_e - \frac{4.66}{\omega_{ce}^2\tau_e^2}\nabla_\perp T_e - \frac{5}{2|\omega_{ce}|\tau_e}\mathbf{b}\times\nabla T_e\right). \tag{1.36}$$

The ion heat flux is

$$\mathbf{q}_i = \frac{n_iT_i\tau_i}{m_i}\left(-3.9\nabla_\parallel T_i - \frac{2}{\omega_{ci}^2\tau_i^2}\nabla_\perp T_i - \frac{5}{2|\omega_{ci}|\tau_i}\mathbf{b}\times\nabla T_i\right). \tag{1.37}$$

The rate of momentum transfer from electrons to ions $\mathbf{R}_i$ is the same as the momentum transfer from ions to electrons $\mathbf{R}_e = -\mathbf{R}_i$. (Here external momentum sources are not considered.) Electrons and ions exchange momentum via two forces, the friction force and the thermal force. Writing $\mathbf{R}_e = \mathbf{R}_u^{(e)} + \mathbf{R}_T^{(e)}$, the friction force is

$$\mathbf{R}_u^{(e)} = -\frac{m_en}{\tau_e}\left(0.51\mathbf{u}_\parallel + \mathbf{u}_\perp\right) \tag{1.38}$$

where $\mathbf{u} = \mathbf{u}_e - \mathbf{u}_i$ is the mutual velocity of electrons and ions. Using the plasma current $\mathbf{j} = en\mathbf{u}$ and the parallel and perpendicular plasma conductivity

$$\sigma_\parallel = 1.96\frac{n_ee^2\tau_e}{m_e} \tag{1.39}$$

$$\sigma_\perp = \frac{n_ee^2\tau_e}{m_e}, \tag{1.40}$$

the friction force can also be written as

$$\mathbf{R}_u^{(e)} = ne\left(\frac{\mathbf{j}_\parallel}{\sigma_\parallel} + \frac{\mathbf{j}_\perp}{\sigma_\perp}\right). \tag{1.41}$$

The thermal force is

$$\mathbf{R}_T^{(e)} = -0.71n\nabla_\parallel T_e - \frac{3}{2}\frac{n}{|\omega_{ce}|\tau_e}\mathbf{b}\times\nabla T_e. \tag{1.42}$$

Finally, the ion heat source contains the energy transfer from electrons via collisions

$$Q_i = \frac{3m_en}{m_i\tau_e}(T_e - T_i), \tag{1.43}$$

while the electron heat source features the same term taken negatively and the Ohmic heating:

$$Q_e = -\mathbf{R}_e\cdot\mathbf{u} - Q_i = \frac{j_\parallel^2}{\sigma_\parallel} + \frac{j_\perp^2}{\sigma_\perp} + \frac{1}{ne}\mathbf{j}\cdot\mathbf{R}_T^{(e)} + \frac{3m_en}{m_i\tau_e}(T_i - T_e) \tag{1.44}$$

Thus, one obtains a closed equation system called the Braginskii equations. In transport codes, these are supplemented by the current equation $\nabla \mathbf{j} = 0$ which expresses the plasma quasineutrality. This allows the calculation of the plasma potential $\Phi(t, \mathbf{r})$, which then self-consistently yields the electric field $\mathbf{E} = -\nabla\Phi$.[8]

1.2.3 Transport code strengths and weaknesses

Noteworthy limitations of transport codes generally stem from three sources: the fluid equations (loss of velocity space information), their closure (assumptions on the scale ordering) and the diffusive ansatz (simplification of radial transport). An exact list of criteria can be found in [31, Sec. 2.1.4]. As a result of these limitations, modellers of the tokamak edge often face the following challenges.

The sheath cannot be described self-consistently within a transport code. The sheath violates the spatial ordering assumption, as the plasma parameters vary greatly over a small distance. As a result, the ion velocity distribution function at the sheath edge is, by far, not Maxwellian [Sec. 25.1][8] and the Braginskii closure fails. This is usually overcome by modelling the sheath in a separate kinetic simulation and implementing the results as a boundary condition (for instance, [32]). Essentially, the transport code knows nothing of what happens inside the sheath, only how the sheath *appears* from the outside. With regard to energy transport, the sheath is an energy sink which cools the plasma at the rate

$$q_\parallel = \gamma n_e T_e c_s \tag{1.45}$$

where γ is the sheath heat transmission coefficient, n_e and T_e are evaluated at the sheath edge and $c_s = \sqrt{e(T_e + T_i)/m_i}$ is the sound speed. How the cooling works, where the energy goes or why it has this exact magnitude and functional dependence is inconsequential to the transport code. Subsequently, is the modeller's responsibility to consider whether this boundary condition is physically acceptable and what the value of γ should be.

The parallel transport may not be collisional enough to employ classical heat conductivity and viscosity. This is, again, a violation of the ordering assumption. In high temperature or low density SOL, the mean free path can be comparable to the connection length and thus the gradient size. This has consequences for the part of energy and momentum transport which is mediated by collisions; in particular, the thermal conductivity $\kappa\nabla_\parallel T$ and the momentum transfer due to viscosity $\eta\nabla_\parallel V_\parallel$. In low collisionality plasma, these transports are not as efficient as the classical transport coefficients claim, and consequently the real heat and momentum fluxes, obtained in experiment or kinetic simulations, are much lower than the fluxes calculated by the classical formulas derived within the

[8] Most transport codes are electrostatic, with the magnetic field $\mathbf{B}$ imposed externally.

Braginskii equations. This issue is typically addressed by constraining the classical fluxes by *flux limiters*. A flux limiter is the constant α in the formula

$$q_\parallel^{(lim)} = \kappa_\parallel^{(lim)} \frac{\mathrm{d}T}{\mathrm{d}s} \qquad \text{where} \qquad \kappa_\parallel^{(lim)} = \frac{\kappa_\parallel^{(class)}}{1 + \left| \frac{q_\parallel^{(class)}}{\alpha q_\parallel^{(max)}} \right|}. \tag{1.46}$$

This equation gives the prescription for the flux-limited parallel heat flux $q_\parallel^{(lim)}$. The heat flux is still proportional to the parallel temperature gradient, but the heat conductivity $\kappa_\parallel^{(lim)}$ changes depending on the value of the classical (Spitzer-Härm) heat flux $q_\parallel^{(class)} = \kappa_\parallel \frac{\mathrm{d}T}{\mathrm{d}s}$ where $\kappa_\parallel$ is the classical heat conductivity. If the heat flux is relatively small, $\kappa_\parallel^{(lim)} \approx \kappa_\parallel$ and $q_\parallel^{(lim)} \approx q_\parallel^{(class)}$. However, if the heat flux reaches a substantial fraction of $\alpha q_\parallel^{(max)}$, $\kappa_\parallel^{(lim)}$ is reduced so that $q_\parallel^{(lim)} < \alpha q_\parallel^{(max)}$. The maximum heat flux is usually chosen as the free streaming heat flux [32, Eq. (2a)]

$$q_{\parallel a}^{(max)} = 0.8 n_a T_a v_{ta} \tag{1.47}$$

where $v_{ta} = \sqrt{eT_a/m_a}$ is the thermal speed of particle species a (T_a is, as elsewhere, given in eV). A similar flux limiter is employed for the parallel momentum flux $\Gamma_{\parallel m}$,

$$\eta_\parallel^{(lim)} = \frac{\eta_\parallel^{(class)}}{1 + \left| \frac{\Gamma_{m\parallel}^{(class)}}{\beta \Gamma_{\parallel m}^{(max)}} \right|} \tag{1.48}$$

where $\Gamma_{\parallel m}^{(max)} = n_a T_a$ for ion species a. Historically, heat flux limiters have received more attention than momentum flux limiters. While in SOLPS-ITER, for instance, $\beta = 3/8$ is a relatively uncontroversial choice [28, Eq. (C.92)], the choice of α remains disputed. A part of the problem is that heat flux limiters are not particularly efficient at reproducing the functional dependence seen in kinetic codes. As [32, 33] show, to perfectly match the kinetic heat fluxes, they must change with the plasma collisionality and, in the case of ELMs, also with time. The variation spans over an order of magnitude, indicating that no single choice of α will perfectly capture the kinetic effects. [34, Fig. 4] is especially salient in showing that using $\alpha = 0.3$ along an entire flux tube in COMPASS will bring the classical heat flux into rough agreement with the kinetic heat flux, but factor-of-two to factor-of-ten differences will remain due to functional dependence. Alternative models of parallel transport have been suggested for coupling with transport codes, such as the non-local model introduced in [35], but transport codes continue to rely mainly on flux limiters. Choosing their value is still at the modeller's discretion.

The value and profile shape for the perpendicular transport coefficients must be chosen ad-hoc. Since SOLPS-ITER models the perpendicular transport using the diffusive ansatz (Sec. 1.2.1) where the perpendicular transport coefficients are free input parameters, the modeller is faced with the choice which value to choose and whether to employ a profile. There have been efforts to tailor the $D_\perp$ and $\chi_\perp$ profile to exactly match the experimental upstream profile (for instance, [21]) but there are concerns if this could constitute overfitting [36]. Experimental profiles typically have an uncertainty in the temperature and density value and, more importantly, in the radial coordinate since the separatrix position is typically uncertain by at least a fraction of centimeter. (For more information see Sec. 2.3.2 and the attached paper in appendix A.) It can be tempting to ascribe the tailored $D_\perp$ or $\chi_\perp$ profile a physical meaning, but the uncertainty is typically so large that, according to [36], in L-mode flat profiles of $D_\perp$ and $\chi_\perp$ is the most suitable choice.

Steep gradients might develop in front of the divertor targets. As [31, Sec. 2.1.4] describes, low target temperatures (e.g. divertor detachment) may induce gradient lengths which violate the spatial scales ordering. This can be addressed by increasing the grid resolution, but at the cost of increasing the computation power demand.

Despite all of these limitations, transport codes are widely used for both interpretative and predictive modelling of the tokamak edge. Their usefulness and applicability are evidenced by the massive effort going into transport modelling of the ITER tokamak. [1, 37] To date, 2D transport codes remain the ideal compromise between physical faithfulness (two-dimensional, accommodate various divertor geometries, include drifts, precise treatment of atomic and molecular physics) and computation time. While transport code simulations can easily be time-demanding, 3D transport codes, turbulent codes and kinetic codes are significantly worse off. The limitations discussed in this chapter must always be kept in mind and it must be carefully considered whether they are addressed. However, thanks to the accumulated extensive experience with transport codes (the first predecessor of SOLPS-ITER, B2, was published in 1982 [38]) and their relentless innovation, these problems are generally well-explored, tame and predictable. This is why transport codes such as SOLPS remain the work horse of ITER edge plasma modelling and SOLPS-ITER modelling is sought also for the COMPASS and COMPASS-Upgrade tokamaks.

1.3 Modelling of COMPASS and COMPASS-U

The COMPASS tokamak is a small to middle-size machine hosted at the Institute of Plasma Physics, Prague. [39] It has ITER-like geometry in the scale 1:10: major radius $R = 0.56$ m, minor radius $a = 0.23$ m, elongation up to 1.8, plasma current $I_p < 400$ kA, toroidal magnetic field at the magnetic axis $B_t = 0.9 - 1.6$ T and pulse duration $t < 0.4$ s. It reaches central electron temperatures of $T_e < 1.5$ keV and densities of $n_e < 10^{20}$ m^{-3}. Its additional heating systems comprise two NBI beams, which facilitate NBI-assisted H-mode, but purely ohmic H-mode is also possible. It is equipped with a broad set of quality diagnostics [22], including high-resolution Thomson scattering, lithium beam emission spectroscopy, two divertor probe arrays, infrared thermography and four reciprocating probes. Its first wall is made of stainless steel and its divertor is made of carbon.

The COMPASS scientific program encompasses many areas. [40] Most prominently it is edge plasma physics, which is studied from many angles: H-mode physics [41, 42, 43, 44], pedestal width physics [45, 46, 47], L-H power threshold and isotope effects [48], ELMs and their control by resonant magnetic perturbations and vertical kicks [49, 50], zonal flows [51, 52], transport in the edge plasma [53, 54, 55, 56, 57] and edge plasma turbulence [58, 59, 60, 61]. Recently experiments with liquid lithium target have also been conducted. [2, 62] Additional COMPASS research areas are MHD equilibrium and instabilities [63], plasma-wall interaction [64, 65, 66] and physics of runaways and disruptions [67, 68, 69, 70, 71, 72].

COMPASS-Upgrade is the successor of COMPASS, featuring brand new hardware infrastructure (vacuum vessel, toroidal and poloidal coils, power supplies etc.) and partially adopting the existing diagnostics systems and software infrastructure. [73] At the time of writing, it is in the final design phase. COMPASS-U will be larger than COMPASS (major radius $R = 0.84$ m, minor radius $a = 0.28$ m) with a substantially higher magnetic field ($B_t \leq 5$ T, $I_p \leq 2$ MA). Its toroidal field coils won't be superconducting, however; they will be copper, cooled by liquid nitrogen to reduce their resistivity. The large magnetic field density will allow ITER- and DEMO-relevant experiments which are not possible on other currently operating tokamaks. In this sense, COMPASS-U will be a replacement for the decommissioned Alcator C-mod. COMPASS-U will reach central electron temperatures of $T_e = 2.5$ keV and densities $n_e = 8 \times 10^{20}$ m^{-3}. It will be equipped with 4-6 MW of NBI power and 2 MW of ECRH power. One of the key research topics of COMPASS-U will be divertor physics. Owing to its exchangeable divertor design, it will achieve not only the single null configuration but also the double null and snowflake configuration. The small predicted heat flux fall-off length $\lambda_q^{(OMP)} \approx 1$ mm [2] will mean very large power densities on the strike lines, similar to fusion reactors such as ITER, so divertor detachment studies will be crucial. Additionally, COMPASS-U will explore liquid divertor target operation. On the whole, COMPASS-U is a project of international importance which will facilitate studies in hitherto unexplored physics of high magnetic field, high power flux plasmas.

Both COMPASS and COMPASS-U would profit greatly from transport code simulations — both as interpretative and predictive modelling. Previous COMPASS experiments with impurity (argon, neon and nitrogen) injection suggest that the impurities are not well confined in the divertor volume but penetrate into the main plasma as well. [57, 74] As a result, the COMPASS SOL does not detach in the traditional sense, where a large pressure gradient along the field lines is formed. (Different, sometimes conflicting definitions of detachment are one of the reasons why [7] defines detachment as $T_e < 10$ eV.) It would be of great interest to reproduce this behaviour using a transport code. Another application of transport codes is found in modelling the edge plasma electric fields. Experiments and transport code modelling with drifts enabled suggest that changing the X-point height changes the electric field structure and thereby modifies the L-H transition threshold. [75, 76] Transport codes which incorporate drifts are able to self-consistently model the edge plasma electric field and would be ideal for verifying this conjecture. [77, 78] Drifts also modify the divertor density patterns, and therefore affect the temperature and heat flux profile. Changing the heat flux profile implies changing the heat flux fall-off length λ_q, a key parameter of power exhaust (Sec. 1.1); it has been theorised that this afflicts λ_q measurement using the Eich function at COMPASS. For COMPASS-U, transport code simulations would greatly help in predicting the edge plasma parameters, which are crucial for diagnostic and heating systems design and construction. In summary, transport codes are an ideal supplement for the COMPASS and COMPASS-U physics program.

1.4 Magnetic equilibrium reconstruction accuracy

Reconstructions of the magnetic equilibrium using the Grad-Shafranov equation are an invaluable tool in tokamak operation, diagnostic measurements, experimental data post-processing and plasma simulations. As discussed in section 1.1, the magnetic field topology is a basic defining feature of the tokamak operation. Magnetic equilibrium reconstructions are utilised in countless facets of tokamak data analysis. From the reconstructed magnetic axis position, one can judge in experiment whether the plasma column is moving and employ the appropriate feedback schemes to steady it. The tomographic reconstruction of plasma radiation is only possible with the magnetic equilibrium as input. Comparison of diagnostic measurements taken at different locations (e.g. the outer midplane and the divertor targets) are performed by mapping them along the magnetic field lines of a reconstructed equilibrium. Transport codes, among other instances of modelling software, construct their computing mesh on top of the equilibrium. The list continues indefinitely. In summary, it can be safely said that without equilibrium reconstructions, much of the present tokamak research would be impossible.

Regrettably, equilibrium reconstructions typically feature slight inaccuracies. The errors in the magnetic flux surface position can range from several mm to cm depending on the particular machine, discharge phase and the flux surface location in the vessel. This is negligible in some applications, but in edge plasma, where the SOL fall-off length is in the order of mm, a few millimeters can constitute an unacceptable uncertainty.

A classic example is the determination of the separatrix plasma parameters. Let us consider an example — the experimental assessment of the SOL transport regime by the way of measuring the upstream-to-target electron temperature ratio $T_{e,u}/T_{e,t}$ in the first SOL flux tube. In the absence of an accurate equilibrium reconstruction, the target temperature $T_{e,t}$ can be, with some allowances and in attached plasmas, taken as the peak target temperature. The upstream temperature profile, however, features no immediately apparent points of reference for $T_{e,u}$ estimation. (Attempts to find and justify such points of reference are described below.) Since uncertainties of one T_e fall-off length in the separatrix location translate into nearly factor-of-three uncertainties in the separatrix temperature, simply taking $T_{e,u}$ at the location indicated by the equilibrium reconstruction is not an option which would adequately illuminate the value of $T_{e,u}/T_{e,t}$. Thus, lacking credible equilibrium reconstruction leaves one unable to answer the simple question of the experimental parallel temperature gradient, despite having perfectly good temperature measurements both from upstream and downstream.

One can (and commonly does) address this showstopper by introducing additional assumptions. In this particular case, one might presume "$T_{e,u} = T_{e,t}$ in the far SOL" and "the reconstruction errors are not large enough to substantially affect flux expansion". This allows one to map the divertor measurements onto the upstream measurements, correct the mapping by aligning the far SOL T_e profiles and then taking $T_{e,u}$ from the same flux surface as the divertor T_e peak. Thus, $T_{e,u}/T_{e,t}$ has been determined.

Questions requiring precise equilibrium reconstructions can be — and often are — answered despite known faults in the reconstruction. However, the assumptions made during the process can be galling to prove and, as a result, are often left unproven. Hence, one typically mends the equilibrium inaccuracies by replacing them with physical and methodical inaccuracies. It bears scrutiny how trustworthy such answers actually are.

In addressing the problem of equilibrium reconstruction inaccuracies, two approaches have been adopted: correcting the equilibrium solver and correcting (or bypassing) the equilibrium reconstruction. The former approach deals with root causes of reconstruction errors, which can be numerous. Most equilibrium solvers, such as EFIT++ employed at COMPASS [79], fit a solution of the Grad-Shafranov equation to the experimental measurements of magnetic field around the tokamak.

Since the plasma is constantly changing, the equilibrium assumption $\frac{\partial}{\partial t} = 0$ can be violated, especially during fast electromagnetic transients such as ELMs or disruptions. [80] The magnetic coils can be placed on adjacent flux surfaces or be few in number, failing to properly constrict the solution. The coil signals can be noisy, introducing random error into the equilibrium reconstruction. Systematic errors can result from improperly aligned diagnostics. Fixing these problems is often machine-specific. On COMPASS, we have recently discovered that the 16 inner partial Rogowski coils, which form the ground basis of equilibrium constraint, are slightly misaligned. [81] Additionally, it was found that divertor Mirnov coils can provide valuable additional input, but that they have been set up improperly and their data has been severely lacking in quality. Thanks to these findings, systematic errors in the COMPASS equilibrium reconstructions were reduced. [82] Unfortunately, the retroactive employment of these correction is limited, in part because of the low quality of the divertor Mirnov coil data. Therefore, even after fixing the equilibrium solver to one's best ability, it remains an intriguing question whether one can correct the resulting equilibrium reconstructions — or bypass them entirely.

The search for corrections or alternatives to equilibrium reconstructions has a rich history which, interestingly, often concerns a particular machine. In DII-D, Porter et al [83] introduced a method which relates the separatrix to the area of profile steepening in the plasma edge. This technique has been referred to as the "standard DIII-D method" [84] and it has been routinely applied until the present day. [85, 86, 87] In ASDEX-Upgrade, calculating the separatrix temperature using the power balance in the two-point model has seen considerable popularity. [88, 89, 90, 91] In COMPASS, the separatrix has been identified with or related to the velocity shear layer, where the poloidal plasma rotation changes direction. [92, 93, 52] An interesting take on the subject was introduced at the JFT-2M tokamak, where a peculiar Langmuir probe design was put forth specifically for separatrix detection [94] and it was suggested that the geodesic acoustic eigenmode (GAEM) amplitude falls to zero at the separatrix in L-mode. [95, 96] To summarise, while fragmented knowledge is available, a rigorous analysis providing sound theoretical, modelling and experimental evidence for these alternatives to equilibrium reconstruction has not hitherto been conducted.

A secondary goal of my research is to propose and validate alternative methods of separatrix detection using edge plasma diagnostics. This is loosely connected to my primary goal, SOLPS-ITER simulations of COMPASS, since equilibrium reconstructions are used for building the computation grid and code-experiment comparison. The first results were presented already in my Master's thesis, where the assumption of poloidal symmetry of the electron temperature and plasma potential was employed to derive a correction of mapping to the outer midplane. [97]

A detailed comparison of probe measurements of the velocity shear layer, blob birth zone and near/far SOL boundary was presented at the Fusenet PhD Event 2018 and the 3rd European Conference on Plasma Diagnostics, Lisbon, Portugal, 2019. [98, 99] Finally, the velocity shear layer position was used to benchmark the aforementioned improvement of the COMPASS reconstructions in *K. Jirakova*[9] *et al, Systematic errors in tokamak magnetic equilibrium reconstruction: a study of EFIT++ at tokamak COMPASS, Journal of Instrumentation **14** (2019) C11020.* Although a peer-reviewed publication in an impacted journal may already be considered success in the frame of a PhD, much more work remains. The shutdown of the COMPASS tokamak will be an opportunity to develop data mining databases which can help answer the question of the separatrix position systematically and rigorously.

[9]My maiden name.

Chapter 2

The SOLPS-ITER code

2.1 Basic information

SOLPS-ITER [13] is a suite of several codes, most notably B2.5, a 2D multi-fluid transport code solving the plasma state [100], and EIRENE, a 3D multi-species Monte Carlo code solving the neutrals state [19]. SOLPS-ITER development is spearheaded by the ITER organisation and its main purpose is to model ITER plasmas. It is the current apex of a line of ever evolving transport codes: the earliest Braginskii equation solver B2 [38], the coupled B2+EIRENE code line SOLPS4.0, 4.1 and 4.3 [101, 102, 103] and the improved B2.5+EIRENE code line SOLPS5.0, 5.1 and 5.2 [104, 105, 106]. SOLPS-ITER is useful for modelling complex SOL processes such as impurity production, transport and deposition, divertor target detachment or patterns of electric field, drifts and currents in the divertor area thanks to its precise treatment of neutrals (including e.g. atomic and molecular physics and chemistry) and the transport processes in plasma.

By default SOLPS-ITER uses both B2.5 and EIRENE for simulating its plasmas ("coupled" simulations). The B2.5 code iteratively adjusts the plasma parameters on its computational grid to achieve a match between the left- and right-hand side of the Braginskii equations. The difference between the l.h.s. and r.h.s. for each equation is called the residuals of this equation, and it is formally equal to the $\mathrm{d}/\mathrm{d}t$ term in the equation, though the code iteration does not reproduce actual time evolution of a plasma. The EIRENE code calculates the paths and reactions of neutral atoms and molecules based on the current plasma background and passes the results to B2.5 as neutral sources. In the standard settings, 14 B2.5 runs are performed for every EIRENE run, as illustrated by Fig. 2.1. Beside the coupled version, it is also possible to run the standalone version of B2.5, where neutrals are treated as another plasma fluid with zero charge.[1] Standalone runs

[1]These so-called fluid neutrals are always present in B2.5 simulations. If EIRENE is used

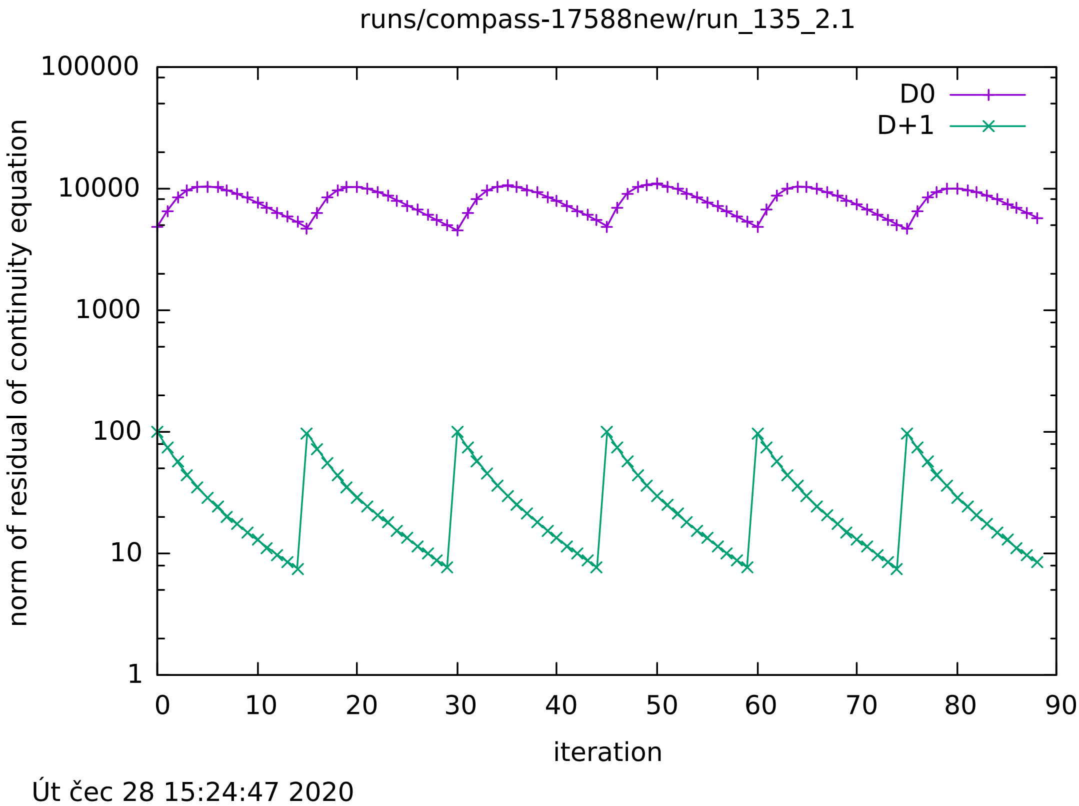

Figure 2.1: Continuity equation residuals plotted using the `resco` command. Every point where the D+1 residuals move downward corresponds to a B2.5 iteration while the spikes are EIRENE calls. Observe the noise this introduces into the simulation and prevents further residuals reduction.

typically converge faster since EIRENE calls introduce significant statistical noise into the simulation; however, they do not capture the neutral physics as well. In this study, only coupled simulations were performed.

It is possible to carry out both time-resolved and steady-state simulations using SOLPS-ITER. In this study, only steady-state simulations were performed.

Within this work, we will refer to the main directory of the local SOLPS-ITER installation as `$SOLPSTOP`. This is the name of the variable available in the SOLPS-ITER work environment which contains to path to the local SOLPS-ITER installation directory.

SOLPS-ITER is shipped with extensive documentation. The pivotal docu-

(file `b2mn.dat`, switch `'b2mndr_eirene' '1'`), they are downscaled to utter unimportance (file `b2mn.dat`, switch `'b2mndr_rescale_neutrals_sources' '1.0e-10'`).

ment, which we will refer to frequently over the course of this work, is the SOLPS-ITER user manual [28]. Compiled in `$SOLPSTOP/doc/solps/solps.pdf` every time SOLPS-ITER is updated, it is the primary source of information about the code and its properties. This documentation is, however, somewhat confusing for a complete beginner who is only getting started with SOLPS-ITER. To fill this gap in knowledge, and also to preserve my own know-how for the future years, I have written an extensive GitLab package `solps-doc` (available from `https://repo.tok.ipp.cas.cz/jirakova/solps-doc`). Much of the following information is paraphrased or elaborated in this comprehensive, easy-to-use package.

2.1.1 Braginskii equations implementation in B2.5

B2.5 is the transport code component of SOLPS-ITER, responsible for calculating the plasma state based on given boundary conditions and other parameters. Its equations and switches control which plasma physics phenomena the simulation will exhibit. For instance, drift terms may be activated or deactivated, introducing the $E \times B$ or diamagnetic drift, and various corrections to individual variables may be applied, such as limiting the total drift velocity by the value of the thermal velocity (refer to equations (C.22) and (C.6) in [28]).

B2.5 calculates the plasma state by solving a set of $2n_s + 3$ equations, where n_s is the number of ionic species including the fluid neutrals. For instance, in pure deuterium plasma $n_s = 2$, with species 0 being neutral deuterium atoms and species 1 being deuterium ions. For every species there is a continuity equation and a parallel momentum balance equation. (The full momentum balance equation has three components, corresponding to the parallel, radial and binormal momentum. In SOLPS-ITER, however, only the parallel component is solved. One degree of freedom is removed by assumption of toroidal symmetry and another by the diffusive ansatz for the radial transport, which turns the radial velocity/momentum into a dependent variable calculated from the local gradients.) In addition, there is the electron internal energy equation, the ion+neutral internal energy equation and the electric potential equation. [100] This makes for a total of 7 equations for the pure deuterium simulations performed in this work.

The equations of B2.5, however, resemble the Braginskii equations (section 1.2.2) only remotely and upon close inspection. The reader is invited to read the SOLPS-ITER documentation, path `$SOLPSTOP/doc/B2solps5.2_equations_2020.02.26.pdf` or appendix C of [28], *Model equations for B2.5*. In the appendix, there are over 200 scarcely annotated equations detailing the B2.5 implementation of the Braginskii equations and hundreds more describing the typical boundary conditions. The complexity is amazing and, to the beginning user of SOLPS-ITER, impenetrable. In this section, therefore, we describe the basic features of the Braginskii equations

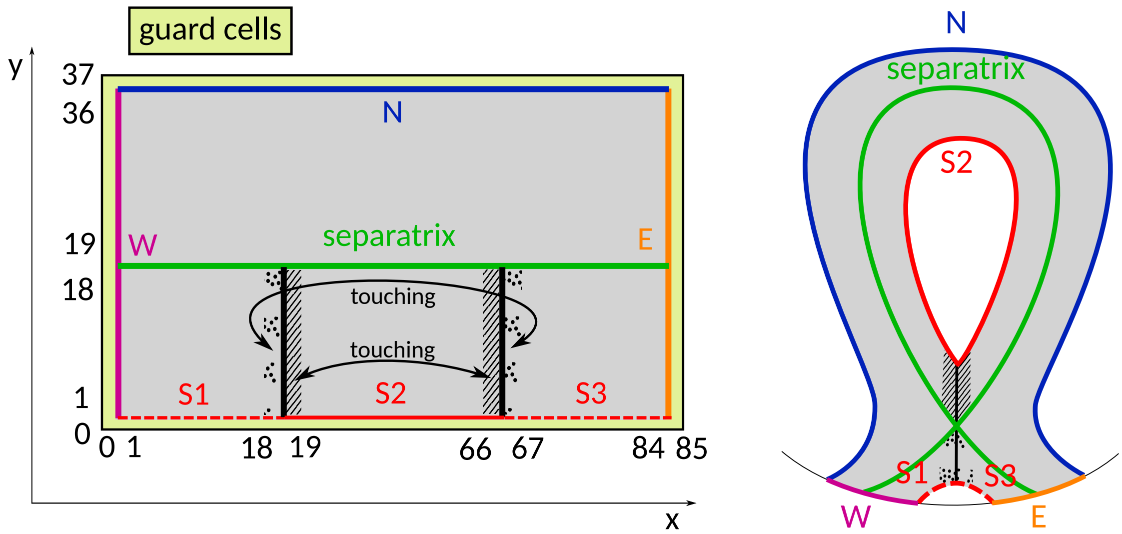

Figure 2.2: B2.5 grid scheme used in the simulations presented in this work. On the left, the rectangular representation including cell numbers. On the right, the physical 2D representation. Both the versions show the location of the boundary regions; more on boundary equations in section 2.1.2.

as implemented by B2.5. Only the most important equations and terms will be elucidated in detail so as not to take up 99 % of this work.

In spite of presenting only pure-D, drift-free simulations, where many terms of the B2.5 equations are zero, we shall describe the full form of these equations as available in the current (September 2020) release of SOLPS-ITER. This is an investment into the future. Before the end of my PhD, I am more than likely to run simulations with impurities and/or drifts.

Grid coordinates and sign convention

Figure 2.2 shows the general shape of the B2.5 grid for the lower single null (LSN) geometry. Of greatest importance here are the two axes: x going clock-wise in the poloidal direction and y going outward from the magnetic axis in the radial direction. These two directions comprise the 2D nature of B2.5.

Let us define geometric variables derived from this grid first. The cell size in the poloidal direction is denoted h_x, in the radial direction h_y. The cell volume is

$$\sqrt{g} = h_x h_y h_z$$

where $h_z = 2\pi R$ is the toroidal loop length at the major radius R and, effectively, the "toroidal cell size" [107]. An additional geometric variable is the magnetic field pitch,

$$b_x = \frac{B_x}{B} \qquad\qquad b_z = \frac{B_z}{B}.$$

These geometric quantities appear in all B2.5 expressions.

The (x, y) coordinates are used throughout the SOLPS-ITER documentation in favour of the more physical coordinates: the parallel direction $\|$, the radial direction r (coincident with y up to discretisation errors) and the binormal direction $\perp$, which is locally perpendicular both to the magnetic field lines and the radial direction. The majority of tokamak edge plasma physics is most readily expressed in the $(\|, y, \perp)$ coordinates. For instance, the sound speed c_s of the plasma achieved at the sheath entrance is directed along the magnetic field lines. To adapt these quantities to the (x, y) grid, projections using the local magnetic field are taken. The poloidal fluxes are composed of the binormal and parallel component [77]:

$$V_x = b_z V_\perp + b_x V_\|$$

Thus one expresses the flow from one cell to its next poloidal neighbour. The radial (y-directed) fluxes need no such projection since they already denote the fluxes between neighbouring cells.

Variables

The $2n_s + 3$ equations of B2.5 are solved for $2n_s + 3$ variables: n_s densities of each ion/neutral species (denoted n_a, `na` in the code), n_s parallel velocities of each ion/neutral species (denoted $V_\|$, `ua` in the code), the common ion temperature T_i (`ti`), the electron temperature T_e (`te`) and the plasma potential Φ (`pot`). All other quantities — poloidal and radial velocities, currents, heat fluxes etc. — are calculated from these basic plasma parameters and other, mostly geometry-related variables and constants.

Continuity equation

The continuity equation of ion/neutral species a in B2.5 (equation (C.1) in [28]) reads:

$$\frac{\partial n_a}{\partial t} + \frac{1}{\sqrt{g}}\frac{\partial}{\partial x}\left(\frac{\sqrt{g}}{h_x}\widetilde{\Gamma}_{ax}\right) + \frac{1}{\sqrt{g}}\frac{\partial}{\partial y}\left(\frac{\sqrt{g}}{h_y}\widetilde{\Gamma}_{ay}\right) = S_a^n \tag{2.1}$$

Here $\widetilde{\Gamma}_{ax}$ is the poloidal particle flux of species a, $\widetilde{\Gamma}_{ay}$ is the radial particle flux of species a and S_a^n is the total source/sink of particles of species a. We observe a form similar to equation (1.12): the number of particles a at a given location can change only due to their fluxes in the x and y direction or due to their creation at or removal from this location. In particular, the source term S_a^n comprises contributions from ionisation, recombination, charge exchange and interaction with EIRENE neutrals (section C.2.1 in [28]).

The tilde above the particle fluxes bears further explanation. In the B2.5 documentation, tildes usually denote some sort of correction. For instance, $\tilde{\tilde{\eta}}_{ax}^{(CL)}$ denotes the classical viscosity coefficient with two possible flux limiter corrections (refer to equations (C.90)-(C.94) in [28], to equation (4.3) in [108] and to [109]). Another frequent use of the tilde is to denote quantities whose divergence-free components have been removed. This is, in fact, the case for the particle fluxes in the continuity equation. Here the component which was reduced to its divergent part is the diamagnetic particle flux. The full poloidal component of this particle flux is

$$\Gamma_{ax}^{(dia)} = -\frac{B_z}{B^2 z_a e}\frac{\partial(n_a T_i)}{h_y \partial y}. \tag{2.2}$$

Unfortunately, inserting this flux into the continuity equation (2.1) leads to numerical instabilities. When Rozhansky et al [77] introduced drifts to the SOLPS code line, they addressed this issue by splitting the diamagnetic particle flux into two components: those whose divergence is zero and those whose divergence is finite. The only part of the diamagnetic flux with finite divergence is

$$\widetilde{\Gamma}_{ax}^{(dia)} = n_a \widetilde{V}_{ax}^{(dia)} = -n_a \frac{T_i B_z}{z_a e}\frac{\partial}{h_y \partial y}\left(\frac{1}{B^2}\right). \tag{2.3}$$

Substituting (2.3) for (2.2) into equation 2.1 does not change the result of the divergence $\partial/\partial x$ and it improves numeric stability of the code. However, one must bear in mind that expressions (2.2) and (2.3) have different values. Therefore, when real physical fluxes are sought, the "full" diamagnetic flux (2.2) should be used. This substitution is described in depth in [77] and it will be referred to again in the momentum balance equation.

Having commented on the abundance of tildes in the B2.5 documentation, let us write out the components of the particle fluxes $\widetilde{\Gamma}_{ax}$ and $\widetilde{\Gamma}_{ay}$. We will only describe them in broad strokes, as the details including tweaks and corrections can be very complicated. The inquisitive reader is invited to read to appendix C of [28].

The poloidal particle flux of ion/neutral species a is (Eq. (C.2) in [28])

$$\begin{aligned}\widetilde{\Gamma}_{ax} = \left(b_x V_{\parallel a} + V_{ax}^{(E)} + V_a^{corr\text{-}dpc}\right) n_a - D_{n,a}\frac{1}{h_x}\frac{\partial n_a}{\partial x} - \widetilde{D}_{p,ax}\frac{1}{h_x}\frac{\partial p_a}{\partial x} \\ + \frac{\delta_{1,a}}{e}\left(j_x^{(AN)} + j_x^{(in)} + \tilde{j}_x^{(vis\parallel)} + \tilde{j}_x^{(visq)}\right) - \widetilde{\Gamma}_{ax}^{(PSch)}\end{aligned} \tag{2.4}$$

In the first bracket, $b_x V_{\|a}$ is the poloidal projection of the parallel velocity, $V_{ax}^{(E)}$ is the poloidal $E \times B$ drift (non-zero only for ions, equation (C.44) in [28]) and $V_a^{corr\_dpc}$ a numerical correction without explicit physical meaning (equation (C.29) in [28], mentioned also in `$SOLPSTOP/doc/Output_description.pdf`). The next two terms represent anomalous diffusion. The Kronecker delta $\delta_{1,a}$ signifies that the second bracket is only present for the main ion species, deuterium D^+. In this bracket, $j_x^{(AN)}$ is some anomalous current which isn't featured in [77] (equation (C.191) in [28]), $j_x^{(in)}$ is the current driven by ion inertia (equation (C.184) in [28], notably disagrees with equation (19a) in [77]) and $\widetilde{j}_x^{(vis\|)}$ and $\widetilde{j}_x^{(visq)}$ are currents caused by plasma viscosity (equations (C.185) and (C.186) in [28], see also section 2.5 in [77]). Finally, $\widetilde{\Gamma}_{ax}^{(PSch)}$ is some weird-ass Pfirch-Schlütter particle flux which has apparently replaced the diamagnetic particle flux and beside...

"The divergent part of the diamagnetic current corresponds to the particle guiding centre vertical current. Its radial component is the largest in the system. On closed flux surfaces far from the separatrix this current is balanced by the parallel Pfirsch-Schlüter current." - excerpt from [77], section 3.

...I see no reason why it should be here instead of (2.3) (equation (C.5) in the manual).

One notes that the poloidal particle flux has both ambipolar components ($b_x V_{\|a}$, $V_{ax}^{(E)}$ and the anomalous diffusion terms) and non-ambipolar components expressed through currents.

The radial particle flux of ion/neutral species a (equation (C.3) in [28])

$$\widetilde{\Gamma}_{ay} = \left(V_{ay}^{(E)} + V_{ay}^{(AN)}\right) n_a - D_{n,a} \frac{1}{h_y} \frac{\partial n_a}{\partial y} - \widetilde{D}_{p,ay} \frac{1}{h_y} \frac{\partial p_a}{\partial y} + \frac{\delta_{1,a}}{e} \left(j_y^{(AN)} + j_y^{(in)} + \widetilde{j}_y^{(vis\|)} + j_y^{(vis\perp)} + \widetilde{j}_y^{(visq)} \right) - \widetilde{\Gamma}_{ay}^{(PSch)} \tag{2.5}$$

is similar to the poloidal particle flux with a few differences. Evidently, the parallel velocity $V_\|$ is missing since it has no component in the radial direction. The radial $E \times B$ drift is accompanied by $V_{ay}^{(AN)}$ (equation (C.48) in [28]), radial anomalous diffusion, which acts in addition to the next two diffusive terms. Lastly, one more viscosity term appears, $j_y^{(vis\perp)}$ (equation C.195 in [28]). Otherwise the two particle fluxes feature functionally similar terms.

Momentum balance equation

For simulations where hydrogen is the main ion species, the momentum balance equation of species a reads

$$m_a \frac{\partial n_a V_{\parallel a}}{\partial t} + \frac{1}{h_z\sqrt{g}} \frac{\partial}{\partial x}\left(\frac{h_z\sqrt{g}}{h_x}\Gamma^m_{ax}\right) + \frac{1}{h_z\sqrt{g}} \frac{\partial}{\partial y}\left(\frac{h_z\sqrt{g}}{h_y}\Gamma^m_{ay}\right) + \frac{b_x}{h_x}\frac{\partial n_a T_i}{\partial x} + Z_a e n_a \frac{b_x}{h_x}\frac{\partial \Phi}{\partial x} =$$
$$= S^m_{a\parallel} + S^m_{CF_a} + S^m_{fr_a} + S^m_{Therm_a} + S^m_{I_a} + S^m_{R_a} + S^m_{CX_a} + S^m_{AN_a} + S^m_{EIRENE_a}. \tag{2.6}$$

Comparing this to equation (1.15), one notes a term-by-term correspondence. The first term is the time derivative and the next two terms are the momentum flux Γ^m_a divergences in the poloidal and radial direction. The fourth term is the pressure gradient of species a and the fifth is the electric field term. The magnetic field term is zero since we are solving for the parallel velocity component and $\mathbf{V}_{\parallel a} \times \mathbf{B} = \mathbf{0}$. On the right-hand side we have the momentum source terms, defined in section C.3.1 of [28]. $S^m_{a\parallel}$ is the parallel component of the stress tensor divergence, which in B2.5 is considered only for the main ion species and it is zero otherwise. $S^m_{CF_a}$ represents the centrifugal force of the ion parallel motion. $S^m_{fr_a}$ is the sum of friction of ion species a with electrons and with other ion species, proportional to $V_{\parallel a} - V_{\parallel b}$. $S^m_{Therm_a}$ is the thermal force acting upon electrons and ions, proportional to the parallel gradients of T_e and T_i. $S^m_{I_a}$, $S^m_{R_a}$ and $S^m_{CX_a}$ are the ionisation, recombination and charge exchange momentum sources as calculated from B2.5 neutrals. In coupled runs, $S^m_{EIRENE_a}$ takes over this function. Finally, $S^m_{AN_a}$ is a numerical correction for the anomalous radial current.

The poloidal momentum flux of ion species a (equation (C.85) in [28]) is

$$\Gamma^m_{ax} = m_a V_{\parallel a}\Gamma^{Cor}_{ax} - \eta_{ax}\frac{\partial V_{\parallel a}}{h_x \partial x} + \delta_{a,1}\cdot \frac{4}{3}\tilde{\tilde{\eta}}^{(CL)}_{ax}\frac{\partial \ln h_z}{h_x \partial x}V_{\parallel a}. \tag{2.7}$$

The first term represents the parallel momentum $m_a V_{\parallel a}$ carried in the poloidal direction by the poloidal particle flux Γ^{Cor}_{ax}. (Note that this flux is different from $\widetilde{\Gamma}_{ax}$ as used in the continuity equation; refer to its definition in equation (C.9) in [28].) The second term corresponds to... some viscous momentum flux, I can't find any info on it. The third term is, again, only present for the main ions species and it represents some other viscous momentum flux. The viscosity coefficients η_{ax} and $\tilde{\tilde{\eta}}^{(CL)}_{ax}$ are defined in section C.3.3 of [28] and they contain both anomalous contributions and two switch-controlled flux limiters.

The radial momentum flux of ion species a (equation (C.86) in [28]) is

$$\Gamma^m_{ay} = m_a V_{\parallel a}\Gamma^{Cor}_{ay} - \eta_{ay}\frac{\partial V_{\parallel a}}{h_y \partial y}. \tag{2.8}$$

Except for the last term, which is now zero for all ion species, this has the same form as the poloidal momentum flux.

More details on the terms in equation (2.6) can be found in [77].

Electron energy equation

The electron energy transport equation is

$$\frac{3}{2}\frac{\partial n_e T_e}{\partial t} + \frac{1}{\sqrt{g}}\frac{\partial}{\partial x}\left(\frac{\sqrt{g}}{h_x}\widetilde{q}_{ex}\right) + \frac{1}{\sqrt{g}}\frac{\partial}{\partial y}\left(\frac{\sqrt{g}}{h_y}\widetilde{q}_{ey}\right) + \frac{n_e T_e}{\sqrt{g}}\frac{\partial}{\partial x}\left(\frac{\sqrt{g}}{h_x}b_x V_{e\|}\right) =$$

$$= Q_e + c_{E\times B} n_e T_e B_z \frac{1}{h_x h_y}\left[\frac{\partial \Phi}{\partial y}\frac{\partial}{\partial x}\left(\frac{1}{B^2}\right) - \frac{\partial \Phi}{\partial x}\frac{\partial}{\partial y}\left(\frac{1}{B^2}\right)\right] - \tag{2.9}$$

$$-\frac{j_y^{(ST)}}{e n_e}\frac{\partial n_e T_e}{h_y \partial y} + Q_{Fei} + Q_e^{\mathrm{EIRENE}} \tag{2.10}$$

There is only one ion energy transport equation since all ion species share the same temperature T_i.

2.1.2 Boundary conditions

While the Braginskii equations control the processes *inside* the plasma domain, the boundary conditions control its edges. Beside the boundary conditions the user must also specify other parameters (such as the perpendicular diffusion coefficient) which control either the plasma bulk or its boundary.

The standard B2.5 grid (lower single null geometry) has six regions for boundary conditions (see Figure 2.2): NORTH (far SOL), WEST (inner target), EAST (outer target), SOUTH2 (core) and the symmetric duo SOUTH1 and SOUTH3 (private flux region centre). In the standard boundary conditions, these six regions are typically sorted in the order SOUTH2, WEST, EAST, SOUTH1, SOUTH3, NORTH, corresponding to indices 1-6.

Let us list the boundary conditions which were adjusted in the course of this work. In the `b2.boundary.parameters` file:

- **SOUTH2 (S2)**: the "core" boundary conditions. They typically control the upstream temperature and density.
  - `BCENE(1)` and `BCENI(1)`, the electron and deuteron energy equation boundary conditions. Their typical value is 8 - "prescribe the total electron/ion heat flux with constant flux density". The parameters `ENEPAR(1,1,1)` and `ENIPAR(1,1,1)` then give the electron and ion power entering the edge plasma in W (roughly equal to the power crossing the separatrix P_{SOL}).
  - `BCCON(0,1,2)`, the main ion continuity equation boundary condition. Its typical value is 1, "prescribe the value of the density". The parameter `CONPAR(0,1,1)` then gives the density value in m^{-3}.

- **WEST** (**W**) and **EAST** (**E**): the inner and outer target boundary conditions. They typically control the sheath properties and are changed both at once.
  - `BCENE(2)` and `BCENE(3)`, the electron energy equation boundary conditions. Their typical value is 3 - "sheath conditions". The parameters `ENEPAR(1,1,2)`, and `ENEPAR(1,1,3)` then give the electron sheath heat transmission coefficient γ_e.
  - `BCENI(2)` and `BCENI(3)`, the ion energy equation boundary conditions. Their typical value is 3 - "sheath conditions". The parameters `ENIPAR(1,1,2)` and `ENIPAR(1,1,2)` then give the ion sheath heat transmission coefficient γ_i.

In the `b2.transport.parameters` file:

- `cflmi` and `cflme`: the ion and electron flux limiters. They control the magnitude of the target heat flux. Following the work of D. Tskhakaya [], I use the value 0.3 for both these flux limiters.
- **Perpendicular diffusion coefficients**. They control the slope of density and temperature profiles. A single value of this coefficient was used in all the simulations presented here, meaning a flat profile of the diffusion coefficients.
  - `parm_dna`: the perpendicular ion particle diffusion coefficient. It controls the slope of the ion density profile. The typical value was 0.2 $\mathrm{m^2s^{-1}}$.
  - `parm_hce`: the perpendicular electron heat diffusion coefficient. It controls the slope of the electron temperature profile. The typical value was 3 $\mathrm{m^2s^{-1}}$.
  - `parm_hci`: the perpendicular ion heat diffusion coefficient. It controls the slope of the ion temperature profile. The typical value was 3 $\mathrm{m^2s^{-1}}$.

Sheath heat transmission coefficient γ

The sheath heat transmission coefficient, also called the sheath energy transmission coefficient, is a parameter relating the particle heat flux lost through the sheath around a solid surface to the local plasma parameters, density n and temperature T. In accordance with [Stangeby, chapter 25.5, equations (25.41)-(25.43)], we define three sheath heat transmission coefficients.

The *electron* sheath heat transmission coefficient γ_e is defined through the equation

$$q_{e,\mathrm{cooling}} = \gamma_e T_e j^+ \tag{2.11}$$

where $q_{e,\mathrm{cooling}}$ is the power electrons entering the sheath remove from the electron population in $\mathrm{Wm^{-2}}$, T_e is the electron temperature at the sheath edge in eV and j^+ is the current density of the ions entering the sheath in $\mathrm{Am^{-2}}$.

The *ion* sheath heat transmission coefficient γ_i is defined through the equation

$$q_{i,\mathrm{cooling}} = \gamma_i T_e j^+ \tag{2.12}$$

where $q_{i,\mathrm{cooling}}$ is the power ions entering the sheath remove from the ion population in Wm^{-2}.

The *total* sheath heat transmission coefficient γ is defined through the equation

$$q_{e,\mathrm{cooling}} + q_{i,\mathrm{cooling}} = \gamma T_e j^+ \tag{2.13}$$

and therefore $\gamma = \gamma_e + \gamma_i$.

Notice that in all three cases, the sheath heat transmission coefficients are defined relative to the *electron* temperature and *ion* current density.

There are two ways to gauge the value of the sheath heat transmission coefficients: experimentally and through theoretical calculations.

In experiment, one may take advantage of the fact that the power lost from the ion and electron populations is equal to the power received by the target, minus the contribution of radiation and the recombination potential energy. In other words,

$$q_{i,\mathrm{cooling}} + q_{e,\mathrm{cooling}} = q_{\mathrm{tot}} - q_{\mathrm{rad}} - q_{\mathrm{rec}}.$$

In the case of an attached plasma, the radiative heat flux q_{rad} may be neglected. The recombination potential energy, which is the energy released by every ion-electron pair which recombine on the target surface and thus lose the ionisation energy of the electron, is roughly 13 eV. At temperatures above 10 eV, the resulting heat flux q_{rec} becomes negligible compared to the kinetic energy of the impinging particles [source, or explain in more detail] and it can be neglected as well.

In [Adámek and Vondráček], divertor infrared camera measurements of q_{total} were compared to the divertor probe measurements of T_e and j^+ in attached COMPASS conditions. The result was that along the entire outer divertor target, the total sheath heat transmission coefficient $\gamma = 11$. A similar result was achieved at Alcator C-mod [Brunner, 2011], where the total sheath heat transmission coefficient was found to have a profile varying from ~ 5 in the far SOL to ~ 15 at the strike point.

While the commonly cited theoretical value of γ is 7–8 [Stangeby, chapter 2.8], this is only the case for ambipolar flows to the divertor, that is, for floating divertor tiles. In COMPASS conditions, the divertor tiles are typically grounded, meaning they can conduct away an arbitrary divertor current (in floating conditions, in contrast, the divertor current is zero). These non-ambipolar conditions are described in [Stangeby, chapter 25.5] including the secondary electron emmission accounting for electrons travelling from the solid surface back into the plasma. The resulting ion sheath heat transmission coefficient is derived to be

$$\gamma_i = 2.5 \frac{T_i}{T_e} \tag{2.14}$$

while the electron sheath heat transmission coefficient is

$$\gamma_e = \frac{2}{1-\delta_e} - 0.5 \ln\left[\left(2\pi\frac{m_e}{m_i}\right)\left(1+\frac{T_i}{T_e}\right)(1-\delta_e)^{-2}\right] + 0.5 \tag{2.15}$$

where δ_e is the secondary electron emission coefficient including both true secondary electron emission and electron back-scatter [Stangeby, chapter 3.1].

2.1.3 Other input parameters

2.2 Installation

The SOLPS-ITER code is available upon request from the ITER Organisation, more precisely from Xavier Bonnin. Following the granting of access, the code can be downloaded from the ITER Github [110] and installed on any local machine which meets its library specifications.

The "one user - one installation" scheme is rather cumbersome for first-time users since installing SOLPS-ITER from scratch takes a few hours at best. At worst, the many required libraries have to be collected one by one, which can take up to a few months. On clusters such as the Marconi Gateway [111], where SOLPS-ITER is run by multiple users, central installations would technically be possible. The main reason against it is that SOLPS exists in multiple releases and some users may want to keep up-to-date with the develop branch while others prefer using an older release whose behaviour they can reliably predict. Advanced users may even want to alter the source code itself, which would impact all other users in a central installation. Other factors include, for instance, that SOLPS-ITER does not consistently separate the user data from the code data. Grids generated by Carre are stored in the Carre submodule rather than in the `baserun` folder, which can create confusion when multiple users create and access these grids. In summary, it is more convenient in the long run that each user download and compile the code individually.

The simulations presented here were performed partially on the Marconi Gateway cluster and partially on the COMPASS Soroban cluster. In both cases, SOLPS-ITER version `3.0.6-503-g48a0460` was used. SOLPS-ITER was installed on the Soroban cluster by Aleš Podolník; his notes on the process are accessible upon request (`podolnik@ipp.cas.cz`). A detailed tutorial how to install SOLPS-ITER is given in `solps-doc`, tutorial *Installing SOLPS-ITER*.

2.3 Creating a new simulation

Creating a new drift-free, pure-D, coupled SOLPS-ITER simulation consists, in broad strokes, of the following steps:

1. create a new, arbitrarily named directory in `$SOLPSTOP/runs/` with a subdirectory `baserun/`
2. procure the wall shape file `*.ogr` and the plasma magnetic equilibrium reconstruction file `*.equ` and place them both into the `baserun/` directory
3. using DivGeo, create a `*.dg` file in `baserun/` containing the simulation geometry needed for building the B2.5 and EIRENE grids
4. using Carre, create the rectangular grid for B2.5
5. using Triang, create the triangular grid for EIRENE
6. rename the stencils generated in `baserun/` to create the boundary conditions file `b2.boundary.parameters` and the transport parameters file `b2.transport.parameters`
7. create a `run/` subdirectory parallel to `baserun/`
8. procure the simulation control file `b2mn.dat` and place it into `run/`
9. in `run/`, run the command `setup_baserun_eirene_links`
10. in `run/`, run SOLPS-ITER using the `b2run` command

The detailed instructions are attached in Appendix ??.

Most of these steps are rather mechanical. Usually, the most time is taken up by step 3, creating a DivGeo file, but this is owed to the countless opportunities for mistakes rather than physical complexity. The process of creating a new simulation therefore doesn't warrant a very deep discussion within the scope of this work, save for three points: choosing input parameters, equilibrium reconstruction accuracy and choosing a discharge for interpretative modelling.

2.3.1 SOLPS-ITER input parameters

The principal input of SOLPS-ITER comprises the wall shape `*.ogr`, the equilibrium reconstruction `*.equ`, a set of specifications in the `*.dg` file (such as the wall material, sputtering coefficients, cell size and many more), the boundary conditions `b2.boundary.parameters` and the transport coefficients `b2.transport.parameters`.

In the presence of other transport codes, such as SOLEDGE2D or EMC3-EIRENE, confusion arises as to which quantities act as SOLPS-ITER input and which come as its output. A typical point of contention is the upstream T_e profile. In other codes, the user may set the profile shape as input and allow the code to adjust the perpendicular heat conductivity χ_e profile to achieve a match. The resulting χ_e profile is sometimes interpreted as a proxy for the actual anomalous perpendicular transport. In SOLPS-ITER, however, it's the perpendicular transport coefficients which act as input. If a flat, single-value profile of χ_e does not perform well (for instance in H-mode), a step-like profile can be specified by hand.

Subsequently the code is run again and the transport coefficient profile is adjusted iteratively until a satisfactory match is obtained. There are concerns how far this can be taken until the χ_e tailoring becomes overfitting with no inherent information about the underlying physics [36], but the use of transport codes to gauge cross-field transport coefficients remains popular nonetheless. In this context and many others, it is important to keep in mind what constitutes input and output of the code, as it may affect the underlying physics the code is able to capture and reproduce.

The discussion surrounding the choice of input parameters is often fascinating as well. SOLPS-ITER offers an abundance of parameters which can be tuned ad libitum, and ad absurdum. From simplifying or sophisticating the wall shape in DivGeo (affects the reflection angle of neutrals) to tweaking the heat flux limiter values (affects the parallel heat flux magnitude), there are uncountable knobs whose turning can yield, conceivably, any result at all. In such a situation, the modeller's task is not only to choose the best option for each parameter but also to provide an explanation why they deem that option as the best and to attempt to quantify the uncertainty introduced to the simulation by the input parameter confidence interval. Unfortunately, SOLPS-ITER offers no built-in feature for errorbar tracking and the default approach remains not to discuss the uncertainties at all. This is not as crucial in interpretative modelling, where the modeller attempts to reproduce existing experimental results. However, predictive modelling of ITER, COMPASS-U and other future machines is, to some degree, a venture into the unknown. In this work, it was attempted to constrain the number of free parameters and use default values whenever possible; refer to section 2.1.2.

2.3.2 Equilibrium reconstruction accuracy

The equilibrium reconstruction is one of the SOLPS-ITER inputs which can, so to say, make or break the resulting simulation. The X-point area geometry can affect the drift patterns and neutral penetration depth. Unrealistic wall-SOL clearances may poorly capture the cooling effect of the wall on the far SOL and, consequently, the downstream temperature and heat flux profile shape. But most importantly, using inaccurate equilibrium reconstructions lowers the credibility of interpretative modelling by introducing substantial uncertainties into the comparison of code results and edge diagnostics measurements.

Take, for instance, one of the key simulation parameters, the separatrix electron density $n_{e,sep}$. In SOLPS-ITER this is almost directly controlled by the boundary condition `BCCON(0,1,2)=1` which sets the electron density at the innermost flux surface. If the separatrix outline provided by the reconstruction is inaccurate, there is no direct way to stipulate the value of the boundary condition from the experimental profile alone. A scan in the boundary condition values may be performed, but the combined uncertainty in many input parameters afflicted by the reconstruction inaccuracy can render a full scan unfeasible, even more so for complex simulations with impurities and/or drifts which take a long time to converge. The careful gauging of underlying equilibrium reconstruction quality consequently constitutes an important step in producing high quality SOLPS-ITER results.

In the first year of my PhD studies, I developed the concept of using electric probe measurements to gauge the equilibrium reconstruction quality on a systematic basis. The results were published in the Journal of Scientific Instruments. [82] The article is attached in appendix A. In summary, it was found that should one accept the edge velocity shear layer ($E_r = 0$) location as a proxy for the separatrix location, then one observes marked systematic differences between EFIT reconstructions before and after the measuring coils positions were corrected. In particular, it was found that in the original reconstructions the distance of the separatrix from the velocity shear layer $R_{sep} - R_{VSL}$ depended systematically on the plasma geometry (its Pearson correlation coefficient with the upper triangularity was 88 %). This dependence was still present after the positions of the measuring coils were corrected, but it was much weaker. Thus it was concluded that the correction did, in fact, improve the accuracy of the equilibrium reconstructions.

Interestingly, it was also found that in the improved reconstructions the velocity shear layer lay consistently outside the separatrix by 1-2 cm. This seems so be consistent with some experimental and simulation results of other machines [112, 113, 114, 115, 116] and inconsistent with others [77, 117]. Insight into the formation of the velocity shear layer and its modelling with drift-enabled SOLPS-ITER would, therefore, be of great interest and it is an intended direction for my future work.

2.3.3 Choosing a discharge for interpretative modelling

All simulations presented within this work comprise interpretative modelling, where experimental plasma conditions are imitated and reproduced as faithfully as possible. Compared to predictive modelling, this is the safer and easier approach since it's easy to tell when the modelling result is wrong and in the case of a mistake the stakes are lower. However, interpretative modelling has a drawback which I, coming from a diagnostics background, did not expect. Choosing a specific discharge to model is difficult.

A discharge best suited for interpretative SOLPS-ITER modelling meets two criteria: 1) it explores interesting physics which can be captured by a transport code, such as divertor detachment, and 2) it features outstanding diagnostics coverage. The latest review of COMPASS diagnostics is given in [22]. Table B.1 lists these diagnostics and comments on their availability and usefulness for SOLPS-ITER modelling. In summary, the most important diagnostics are the horizontal reciprocating probe, the ”new” divertor probe array, the divertor infrared camera, the Thomson scattering diagnostic, bolometry, charge exchange spectroscopy and C-III line spectroscopy. The latter two are currently not producing usable results, and so the former five make up a foundation for the interpretative modelling of COMPASS. Ideally, the discharges best suited for modelling would be found by intersecting the sets of discharges where these diagnostics are active and provide data of high quality.

The problem with this top-down approach is that it is very time-consuming for the diagnosticians, which can result in a refusal to cooperate. During my undergraduate studies I constructed databases of the horizontal and vertical reciprocating probe measurements, with the goal of fast systematic access to high quality data. From this experience I know that such a database cannot be constructed on demand. As of August 2020, there are over 20700 discharges in the COMPASS database. Unless the responsible diagnostician is already maintaining and updating a database of their measurements, it is all but impossible to ask for all the discharges where the diagnostic provides good data. Such a question simply has no sense.

Under these conditions, a bottom-up approach has to be adopted. First, one asks an experiment leader for a recent campaign where relevant physics was investigated. This could be, for instance, a deuterium density scan without NBI heating, performed a few weeks after the last chamber opening and preceded by chamber boronisation. RMP (Resonant Magnetic Perturbation) campaigns are ill-suited for SOLPS-ITER modelling because of the effect of time-dependent magnetic field. Nitrogen seeding campaigns then aren't suited for pure deuterium modelling, obviously. A key factor is that the campaign is recent. This maximises the probability that the diagnostic measurements will be of high quality (as every diagnostic on COMPASS is gradually improved over time; the alternative is falling into obscurity) and that if there was any problem with the measurement (such as the reciprocating manipulator position being shifted by 1 cm), the diagnostician will remember it. This serves the overall strategy to do as much work by oneself and demand as little as possible from the busy diagnosticians.

Once an appropriate campaign is found, one chooses a suitable discharge from it. First one sets apart the ”bad shots”, where the plasma disrupted prematurely. Then, one checks whether the raw signals of the five principal diagnostics were collected. If, for instance, the signal `FIRCAM_RAW` (raw IR camera data) is not present in CDB (COMPASS database) for the investigated discharges, one must move on to another campaign. If all the required raw signals are present, an arbitrary discharge is chosen from the campaign and the responsible diagnosticians are inquired about its experimental data quality. Usually the tokamak diagnostics either do or do not work for the entire campaign, so if one discharge is viable, so are all its brethren. Finally, one chooses a concrete discharge number and a time in which to model it. This choice can be motivated by the available heating (NBI on/off), discharge density (low-density discharges might violate the assumptions of transport codes with their low collisionality), equilibrium stability and accuracy and other factors. The result is a particular discharge number (in this work, discharge #17588) and time ($t = 1100$ ms).

2.4 Running a simulation

Running a time-independent, coupled SOLPS-ITER simulation means to iterate over the following cycle: 1) calculate all the terms in the Braginskii equations using the existing plasma state, 2) calculate a new plasma state from these terms using a discretisation scheme, 3) occasionally interject the B2.5 calls with an EIRENE call. In the EIRENE call, neutrals are injected into the existing plasma and their reactions are compiled into source terms, which are then inserted into the Braginskii equations on the next B2.5 call. A stable, converged solution is reached when iterating over this cycle no longer changes the overall plasma state (more in section 2.4.2.)

The individual calls of B2.5 or EIRENE are set apart by a time interval Δt, but it would be misleading to attribute t the meaning of actual temporal evolution of the simulated plasma. Rather, Δt is a parameter controlling the temporal resolution of the simulation, similar to the number of cells controlling the spatial resolution. The longer Δt is, the faster the simulation can converge if it's stable, but the easier it will diverge if it isn't stable enough (more can be found in section 5.3 of [28]).

In the context of the SOLPS-ITER work environment, the simulations are run using the `b2run` command or using the predefined submission scripts, such as `itmsubmit`, in the `run/` subdirectories. The former is preferable for dry runs (flag `-n`) and very short runs, the latter is preferable for submitting a number of cases at once (parameter scans) or for long-running simulations. How long the simulation should run is specified in the `b2mn.dat` file; it can involve a target number of iterations (switch `'b2mndr_ntim'`), target clock time (switch `'b2mndr_elapsed'`), target magnitude of the residuals and others. Detailed instructions how to run the simulations are given in appendix **??**.

(Possible mention how SOLPS-ITER eats up its node's computational power and how we couldn't deal with that on COMPASS for the time being.)

We will discuss two aspects in depth: the general workflow of SOLPS-ITER and convergence criteria.

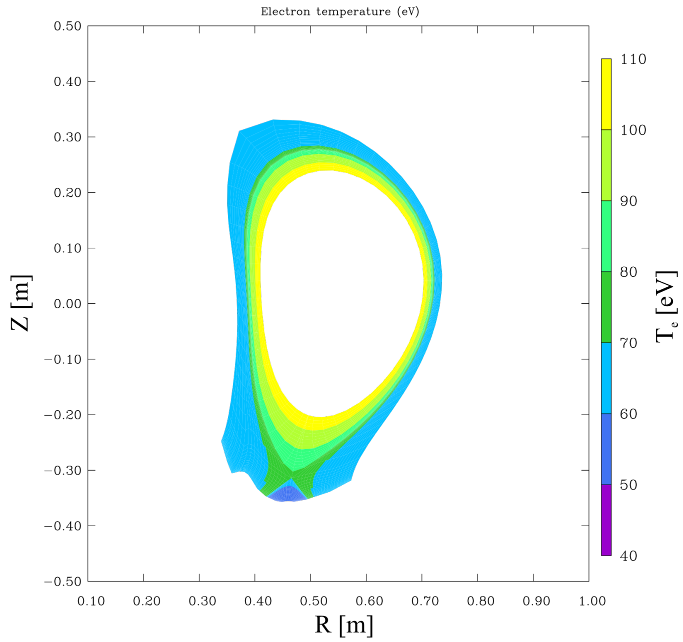

Figure 2.3: "Flat profile" starting state for solving the plasma state by SOLPS-ITER.

2.4.1 General workflow

Running SOLPS-ITER consists of creating new simulations, running them, evaluating the results, tweaking the simulation input and running them again, branching out converged simulations to explore the parameter space, backtracking in case the simulation diverges, cross-checking with experimental measurements and many other processes. In this section we expand on several aspects of the SOLPS-ITER workflow.

In a fresh new simulation created using the instructions in the previous section, the plasma state is predefined as the "flat profiles" state. An example of this initial state is shown in figure 2.3, where a run was initiated for the COMPASS geometry and a single iteration of SOLPS-ITER (to obtain the output files) was performed. The "flat profiles" aren't flat, as the name suggests, and their values are roughly realistic. However, this state is far from the actual solution and the simulation must be run for quite some time before a physical solution is obtained. To hasten the convergence, it is recommended to start with a simpler version of the intended simulation and gradually increase the complexity. A run with drifts may, for example, be initially run without drifts until a drift-free solution has been obtained. Only subsequently are the drift terms turned on. In some cases, it may even be desirable to import the result of a different simulation (different equilibrium, cell number etc.) using the `b2yt` command (section 3.14 of [28]) rather than to start from the "flat profiles" state.

A defining feature of the SOLPS-ITER workflow is relaunching finished simulations. The two most common reasons for this are (i) the simulation has not completely converged yet, and (ii) the simulation result is not satisfactory and the input parameters need to be modified. A practical application of relaunching a simulation comes if the user knows the converged state will take a long time to reach. In this case, it is convenient to split the simulation up into smaller segments (for instance 8 hours long) which are then run in a series. One advantage is that each end state can be archived and if the simulation starts to diverge, it is possible to regress to an earlier version. Another advantage is that 63 8-hour jobs allow for more efficient resource management than one 3-week job. Relaunching a simulation also comes into play when a user wants to check on the results of an ongoing simulation. To use the default plotting tool `b2plot`, the simulation output must be written, which means the simulation has to be interrupted. This is done by the command `touch b2mn.exe.dir/.quit`. Following its call in the `run/` folder, the simulation will end and write its output files. After the user checks the simulation state, they can start it up again as if nothing has happened. In summary, relaunches of earlier runs comprise a majority of the runs a SOLPS-ITER user performs.

The possibility to relaunch finished simulations also allows for the branching of one solution into multiple variants, for instance when performing a parameter scan. First, a common ancestor, located approximately in the centre of the explored parameter space, is created and it is run until it converges. Then, its `run/` directory is duplicated as many times as needed and each of the new directories receives a different set of boundary conditions which override the `baserun/` directives. All of the runs refer to the same `baserun` and, therefore, use the same grids. (If a different grid is needed, a whole new simulation in `$SOLPSTOP/runs/` is needed.) Finally, each simulation is run individually, producing unique results. The total CPU time is consequently significantly shorter than if each simulation was run independently.

The convergence time scale also impacts the workflow. A different approach is needed if a simulation converges within 8 hours than when it takes 6 months. In general, factors which prolong the convergence are machine size, grid resolution, using EIRENE rather than fluid neutrals, using multiple ions species and turning on drift terms. The latter is especially demanding, since it requires a significant reduction in the time step Δt. In the case of the COMPASS simulations presented herein, convergence was reached within a matter of hours at maximum (starting from the "flat profile" state) and 10 minutes at minimum (fine-tuning the target boundary conditions). The time step used was $\Delta t = 10^{-4}$ s. This time scale resulted in a dynamic approach where the trial-and-error method was still very much viable.

A special mention in the SOLPS-ITER workflow belongs to using external clusters for running the simulations. When I began using SOLPS-ITER in a new user training in October 2018, I obtained the login credentials to the Marconi Gateway cluster in Italy and was instructed to user SOLPS-ITER there. This was a quick and easy solution since Gateway already had all the packages SOLPS-ITER requires and the installation took only a few hours, most of that source code compilation. This solution, ideal for a week-long training course, unfortunately gives poorer performance in the long-term perspective. COMPASS experimental data can only be accessed from within the COMPASS network, which means that to compare the simulation and experimental results, the finished runs (comprising hundreds of megabytes and more) had to be copied from Gateway to the COMPASS servers. I wrote post-processing routines which, using SOLPSpy [118], extracted only a handful of relevant information (grid coordinates, plasma parameters etc.) from the hefty SOLPS-ITER output and subsequently only copied that, yet the workflow remained clumsy. The real solution came when SOLPS-ITER was finally installed on COMPASS by Aleš Podolník in April 2020.

2.4.2 Convergence criteria

Convergence is achieved when the plasma state solver reaches the globally optimal solution of the discretised Braginskii equations. Residuals remain finite because of the finite spatial and temporal resolution, but they are reduced to a minimum value. Such a plasma state is stable — further running SOLPS-ITER on it does not change it. Whether or not it has been reached can by gauged by convergence criteria.

Complete convergence criteria applicable to SOLPS-ITER are described in section 4 of [13]. We simplify these criteria to the following:

- The residuals plotted with the `resall_D` command are stable.
- The separatrix temperature (command `2dt tesepm`) and density (command `2dt nesepm`) are stable.
- Basic plasma and input parameters have believable values. This includes both a sanity check (perpendicular particle diffusion coefficient $D_\perp = 10^6$ m^2s^{-1} probably isn't right) and a comparison to experiment (order of magnitude difference of far SOL target T_e might be a problem).

2.5 Post-processing a simulation

The results of a SOLPS-ITER simulation are saved in several files of the `run/` folder, most importantly in the file `b2fstate`. This is a text file containing the basic plasma parameters such as the density of each ion species `na`, electron and temperatures `te` and `te`, parallel velocity of each ion species `ua` and others (refer to appendix A.3 in [28]). To read these files and transform them into a Python object called `RunDir`, the package SOLPSpy has been developed at the Max Planck Institute for Plasma Physics, Garching. [118] Within this work, this package has been used to access the SOLPS-ITER output data.

To compare the experimental and simulation data, a set of Python routines has been written accessing both SOLPS-ITER results through SOLPSpy and the COMPASS database through pyCDB [119]. It is planned to publish this code using the institute GitLab under the name solps-compass. [120]

Chapter 3

Interpretative modelling results

3.1 The modelled discharge and its diagnostics

We present simulations of the COMPASS tokamak discharge #17588 at the time $t = 1100$ ms. Its basic parameters are plotted in figure 3.1; the simulated time, marked with a vertical line, is just before the neutral beam injection begins. It is a deuterium Ohmic L-mode plasma in the divertor configuration, with the ion grad-B drift directed toward the divertor. The plasma current is $I_p = 180$ kA, the toroidal magnetic field is $B_t = 1.38$ T, the safety factor is $q_{95} = 4.2$ and the line-averaged density is $\overline{n}_e = 5 \times 10^{19}$ m^{-3}. The ohmic heating power is $P_{ohmic} = 200$ kW, of which $P_{rad} = 65$ kW is radiated in the core according to bolometer measurements. The power crossing the separatrix is thus $P_{SOL} = 135$ kW.

Out of the five principal diagnostics listed in section 2.3.3, four deliver data of good quality.

- The **combined BPP+LP divertor array** provides target measurements of the target electron temperature T_e and ion saturated current I_{sat}. From these two, the target electron pressure p_e is calculated as well as the total parallel heat flux $q_{\|}$. Only the outer target values are usable; the reason might be connected to magnetic shadowing. [43]
- The **divertor infrared camera** provides divertor measurements of the parallel heat flux $q_{\|}$.
- The **Thomson scattering diagnostic** provides measurements of the electron temperature T_e and density n_e at the plasma top.
- The **bolometer array** provides measurements of the total power radiated in the core plasma. Unfortunately, because of poor line-of-sight coverage of the divertor area, it is impossible to gauge the divertor radiation as well.

The horizontal reciprocating probe is offline. Its measurements would be useful

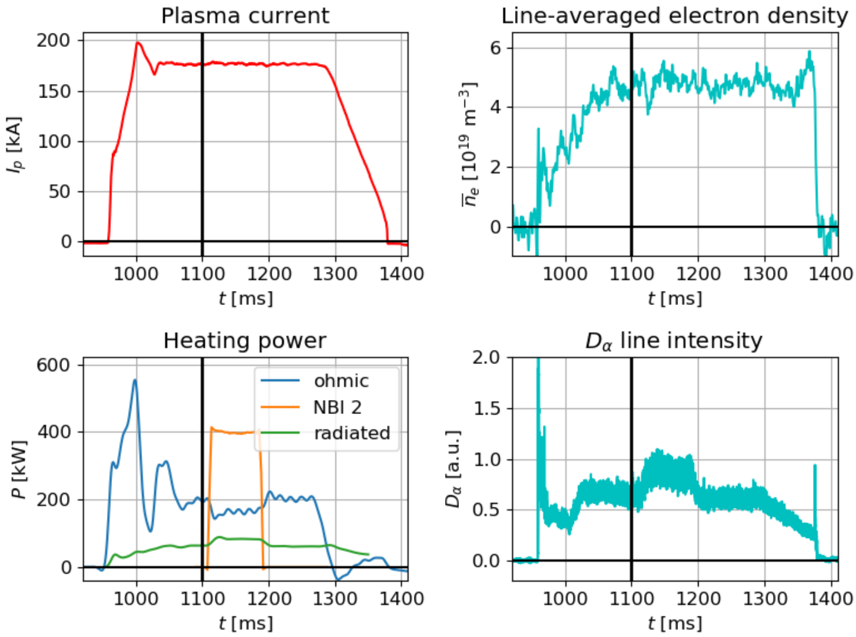

Figure 3.1: Basic characteristics of COMPASS discharge #17588: the plasma current I_p, line-averaged density $\overline{n}_e$, heating power P and the D_α line intensity. The vertical black lines denote $t = 1100$ ms, the time at which the plasma was simulated.

to double-check upstream values of temperature and plasma potential, but they are not strictly necessary for gauging the experiment-code agreement.

The discharge #17588 is representative of a typical COMPASS Ohmic divertor plasma with intrinsic carbon impurities and no impurity seeding, see figure 3.2. The results of its simulations are thus indicative of the typical conditions and physical processes of COMPASS plasmas. As we will see, these conditions correspond to the simple SOL, or sheath-limited regime with small to no T_e gradients along the flux tubes and high divertor temperatures. Given the omission of carbon and, more importantly, drifts, the simulations presented in this chapter cannot fully capture the COMPASS edge physics. However, they are still useful in exploring the application of SOLPS-ITER to COMPASS, provide interesting information which cannot be easily gleaned from experiment (such as T_i values) and form a foundation for later simulations in my PhD thesis.

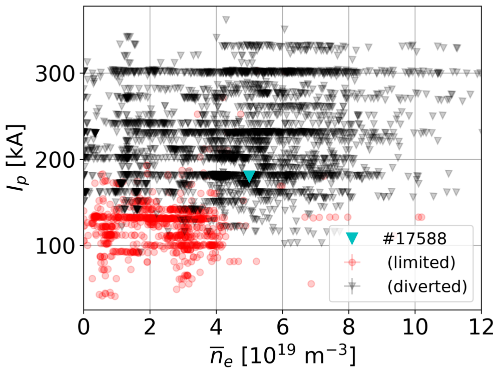

Figure 3.2: COMPASS tokamak operational space. Every point corresponds to a successful discharge. Discharge #17588 is plotted in cyan.

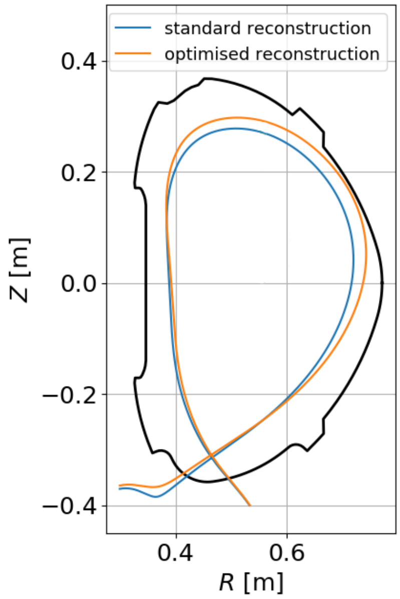

Figure 3.3: Equilibrium reconstructions of discharge #17588 at $t = 1100$ ms: the standard EFIT reconstruction and the reconstruction after O. Kovanda's optimisation. [81]

3.2 Choice of equilibrium reconstruction

To explore the effect of inaccurate equilibrium reconstructions on SOLPS-ITER simulations, two equilibria, shown in Fig. 3.3, were used as bases for the grid construction. The one marked as "standard reconstruction" is the EFIT reconstruction stored in the COMPASS database. This is the default equilibrium one would use for data processing. Conversely, the "optimised equilibrium" was calculated using O. Kovanda's optimised reconstruction [81], which also utilises EFIT but supplies it with different constraints. In particular, corrected inner partial Rogowski coil positions and signals from the divertor Mirnov coils and flux loops were used. Beside the different input, the reconstruction algorithm is exactly the same, so the differences in the reconstruction quality translate directly into the input data quality.

From the perspective of the edge plasma spatial scale, the two equilibria differ substantially. The placement of the outer midplane ($Z = 0$ m) separatrix is 2.1 cm more inward for the standard reconstruction. At the plasma top along the

Thomson scattering laser chord, $R = 0.557$ m, the same difference again makes for 2.1 cm. The largest difference between flux surface placement is on the "top right" of the equilibrium reconstruction, where the limiter clearance of the optimised reconstruction is vanishing. This creates several problems in the simulation and, if reflective of reality, also in the experiment.

The simulation effect stems from the rectangularity of the B2.5 mesh, see figure 2.2. The mesh must avoid scraping any solid surface beside the target, and so its width is extremely limited in this case. This means that only a small part of the SOL is modelled and diagnostics measurements cannot be exploited fully; additionally, it may drive code instabilities caused by tightly spaced cells. After consulting [36], it was decided to side-step the issue by moving the offending limiter part out of the way manually during geometry manipulation with DivGeo. As a consequence, SOLPS-ITER will not capture the particular effect such low clearance would have on the SOL plasma.

If the separatrix is truly this near the limiter, experimental data interpretation becomes complicated. The out-thrust limiter "scrapes off" the Scrape-Off Layer, shadowing part of the inner divertor from the plasma flowing along the field lines from the outer midplane source. The connection length is severely lowered by this, resulting in overall SOL cooling due to more efficient parallel electron power removal. The increased plasma-wall interaction also locally releases neutrals, which increases impurity content in the plasma and further enhances electron power losses. The overall result is that the SOL physics model becomes much more complicated than the simple parallel losses to the targets assumed by B2.5, the two-point model and other commonly used SOL physics models. Experimental observations support the finding that the far SOL is scraped off along the way from the outer midplane to the plasma top and inner target. Figures 3.4 and 3.5 show the (standard EFIT) equilibrium reconstruction of discharge #8870, the measurement trajectories of the horizontal and vertical reciprocating probes (HRCP and VRCP, respectively) and the measured T_e profiles. Long T_e decay is observed at the outer midplane, where the majority of plasma transport is driven outward by ballooning, whereas sharp decline to zero is seen on the plasma top, where profiles are sustained by parallel transport from the outer midplane. This corresponds to the short distance of the top limiters and the separatrix. Low clearance has a constant presence in COMPASS divertor plasmas, even though it is not clear whether it can be as low as figure 3.3 indicates.

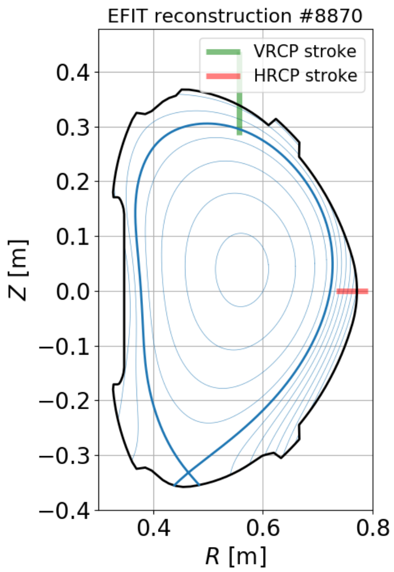

Figure 3.4: Standard EFIT equilibrium reconstruction of COMPASS discharge #8870. Vertical (VRCP) and horizontal (HRCP) reciprocating probe head trajectories marked in green and red, respectively.

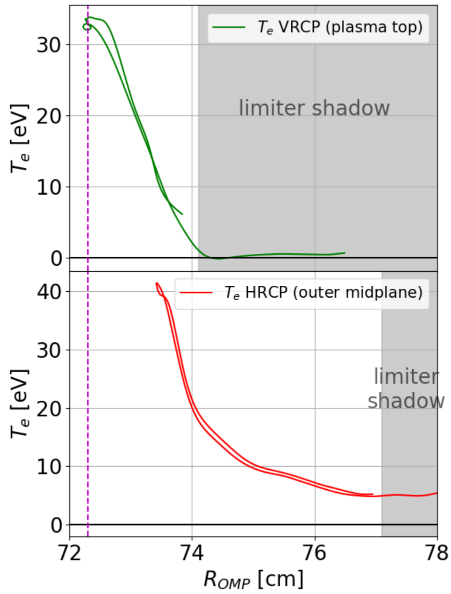

Figure 3.5: T_e profiles measured by the vertical (VRCP) and horizontal (HRCP) reciprocating probe in COMPASS discharge #8870, mapped to the outer midplane using the equilibrium to the left. The dashed vertical line denotes the EFIT separatrix.

3.3 SOLPS-ITER simulations based on different equilibria

A similar set of boundary conditions and input parameters were used for the simulations based on the two equilibria; they are given in Table 3.1. The parameters were chosen manually to yield the best possible agreement to the experimental measurements while leaving other parameters at the default value. Figures 3.6 and 3.6 present the experiment-modelling comparison to the measurements of the Thomson scattering upstream T_e and n_e, outer target T_e, I_{sat}, $q_{||}$ and static electron pressure $p_e = en_eT_e$ measured by the divertor probe array and the target $q_{||}$ measured by the IR camera.

The overall results is such: the simulation based on the optimised equilibrium reconstruction replicates the experiment with reasonable accuracy, showing almost no T_e gradient from upstream to the outer target and thus being representative of

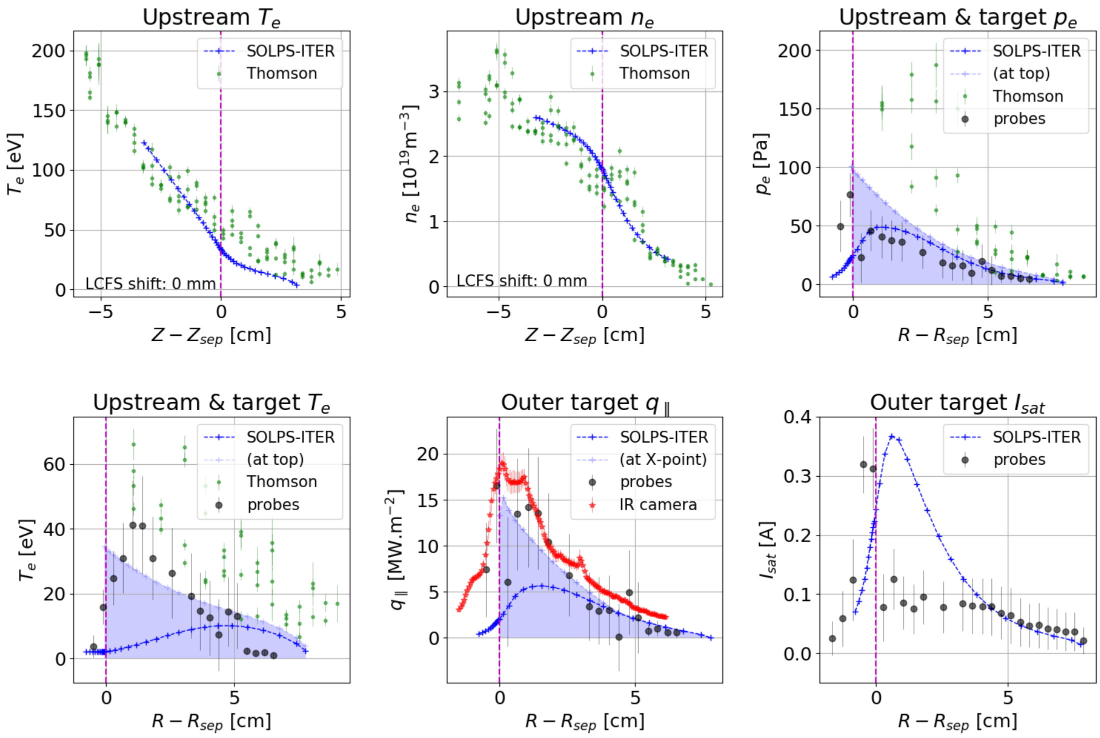

Figure 3.6: Experiment-modelling comparison of the SOLPS-ITER simulation based on the standard EFIT equilibrium reconstruction.

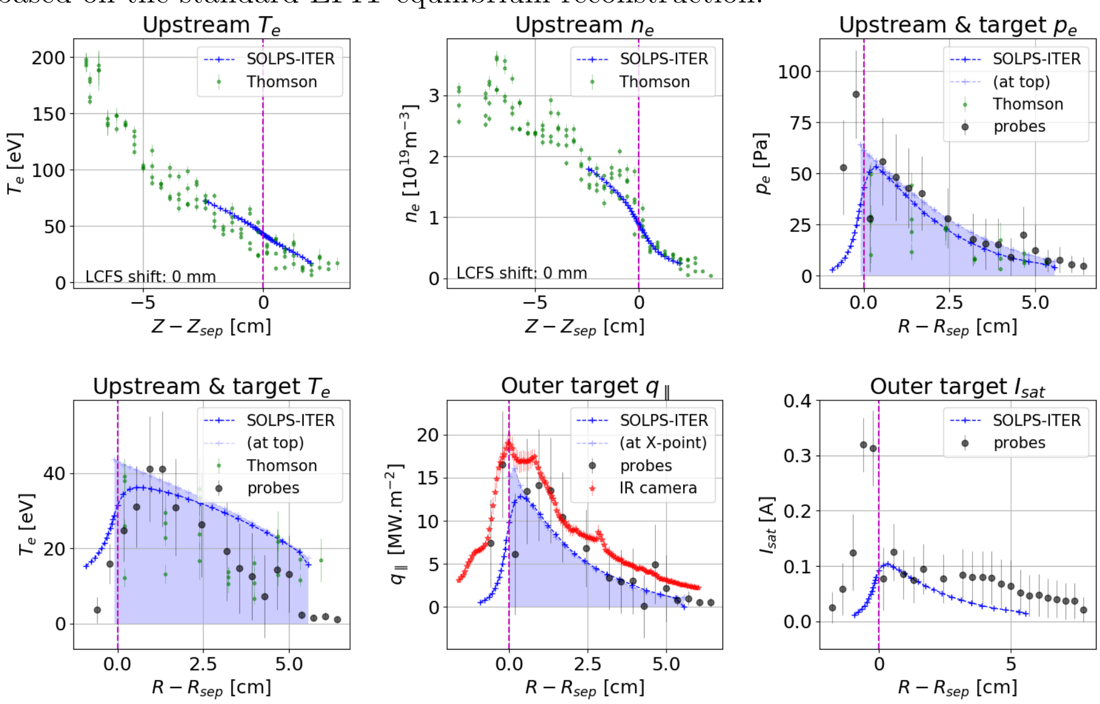

Figure 3.7: Experiment-modelling comparison of the SOLPS-ITER simulation based on the optimised equilibrium reconstruction.

Parameter	Value (stand. eq.)	Value (optim. eq.)
Electron and ion heat transmission coefficient (both targets), `bcene=bceni=3`	`enepar=1.00` `enipar=1.50`	`enepar=1.00` `enipar=1.50`
Total heat transmission coefficient		
Electron and ion heat flux limiter	$\alpha_e = \alpha_i = 0.3$	$\alpha_e = \alpha_i = 0.3$
Upstream density boundary condition, `bccon=1`	$n = 2.6 \times 10^{19}$ m^{-3}	$n = 1.8 \times 10^{19}$ m^{-3}
Upstream electron and ion energy boundary condition, `bcene=bceni=8`	$P_{SOL,e} = 70$ kW, $P_{SOL,i} = 65$ kW	$P_{SOL,e} = 70$ kW, $P_{SOL,i} = 65$ kW
Particle diffusion coefficient, `flag_dna=1`	$D_n = 0.4$ m^{2}s^{-1}	$D_n = 0.15$ m^{2}s^{-1}
Electron and ion thermal diffusivity, `flag_hci=flag_hce=1`	$\chi_i = \chi_e = 1$ m^{2}s-1	$\chi_i = \chi_e = 4$ m^{2}s-1
Electron and ion temperature fall-off length, `bcene=bceni=9`	$\lambda_{T_e} = \lambda_{T_i} = 1$ cm	$\lambda_{T_e} = \lambda_{T_i} = 1$ cm

Table 3.1: Boundary conditions and input parameters of the presented simulations. The parameters represent best fit to the experimental data within physics and engineering constraints.

attached, sheath-limited plasma; conversely, the simulation based on the standard EFIT reconstruction features collapsed outer target T_e profile indicative of the conduction-limited regime and even detachment ($T_e < 10$ eV according to the definition given in section 1.1). This stark difference is driven by the density profile. To replicate the Thomson scattering n_e profile, the "standard EFIT" simulation employs higher n_e boundary condition and higher diffusion coefficient D_n, raising the separatrix density from 0.9×10^{19} m^{-3} to 1.8×10^{19} m^{-3}. Raising the upstream temperature profile was found to be difficult. Its main two drivers are the heat diffusivity χ_e and the input power P_{SOL}, and neither is very efficient at raising the T_{sep} value. The experimental T_e profile was retained for $\chi_e = \chi_i = 7$ and $P_{SOL} = 600$ kW, which is clearly not realistic in an Ohmic plasma with $P_{ohm} = 200$ kW. The temperature boundary condition can alternatively be chosen in a similar manner to density, by fixing the T_e value at the innermost flux surface, but this would arguably still retain high P_{SOL} needed to drive such high separatrix temperature. In summary, the 2.1 cm shift in the separatrix position raises n_{sep} and, thus, the SOL collisionality so much that the near-zero T_e gradient observed in experiment cannot be achieved in the "standard EFIT" reconstruction. This is a clear indication that the magnetic reconstruction is not correct.

It can be argued that there still remain several unused boundary conditions and input parameters which could "fix" the simulation based on the standard EFIT equilibrium. Beside the aforementioned choice of energy boundary condition, one can also tailor the diffusion coefficient and heat diffusivity profile, raise and lower the input power and density boundary condition within bounds given by experimental measurement errors, and add drift or impurity physics into the simulation. A peculiarly common solution is to assume the equilibrium reconstruction is erroneous and shift the modelled profiles by an arbitrary amount in order to produce a good match; more on those later. I would like to argue, instead, that while all of these solutions may work, they can all be supplanted by something much more elegant and first-principle based: basing the simulation upon a better equilibrium reconstruction. In the "optimised equilibrium" simulation, experimental profiles are reproduced with reasonable accuracy *without* tailoring diffusivity profiles, changing boundary condition form from the commonly used alternatives or employing *ad hoc* profile shifts. Its quantitative accuracy is, admittedly, still lacking, but the qualitative property of edge transport regime is undeniable. Provided that improving the equilibrium reconstruction quality is a feasible, I would heavily recommend any SOLPS-ITER user to pursue this venue rather than to invent complex and difficult-to-justify ways to improve the experiment-model fit.

As a final thought, it should be stressed that interpretative modelling requires comparing simulation and experimental results *as a whole*, that is, including every usable diagnostic and discussing every major parameter. Sometimes it is possible to reach good agreement in one area, while another betrays that the experimental plasma is not reproduced well, such as the target temperature profile in figure 3.6. Since target plasma parameters are typically more sensitive than upstream plasma parameters, they can play the role of a canary in a coal mine. The separatrix position is in a similar position in the problem of equilibrium reconstruction; it is a small part of the overall reconstruction, but its inaccuracy has far-reaching consequences in a number of edge physics areas. In practice, setting the input parameters often involves a trade-off between all the involved parameters. Perfect code-experiment agreement is neither sought nor expected, even in a code with as many free parameters as SOLPS-ITER (especially in the beginner stage). Good interpretative modelling then requires finding a suitable compromise between all the forces involved: uncertainties in diagnostics measurement values and positions, errors in the equilibrium reconstruction, transport model input parameters and others.

3.3.1 Employing radial shifts in interpretative modelling

In this section, the "standard EFIT" simulation, presented in figure 3.6, is rerun while allowing the resulting modelled profiles to be radially shifted with regard to the experimental profiles before their match is gauged. The shift makes for $\Delta Z = 1.8$ cm at the plasma top along the Thomson scattering measuring chord and $\Delta R = 0$ cm at the divertor, where no shifting was deemed necessary.

ΔZ was chosen based on several considerations. The Thomson scattering profile of T_e is almost linear in the edge plasma, possessing no distinctive features and quite considerable datapoint scatter (± 15 eV). Considering that the code-experiment agreement in not expected to be perfect, the upstream T_e profiles were considered to match when the SOLPS-ITER profile lies within the datapoint cloud of the Thomson scattering measurements; not necessarily in its middle. The Thomson scattering profile of n_e, conversely, shows distinctive steepening 1.8 cm outside the "standard EFIT" separatrix. Such a steepening is typically retained in SOLPS-ITER results as well, in the area around the separatrix. Although the Thomson scattering data do not provide as high spatial resolution as reciprocating probe measurements, it can be proposed that this steepening is, in fact, the near SOL and its extension with similar fall-off length into the confined plasma. It is therefore reasonable to choose ΔZ as the shift which will match the position of the upstream density profile steepening.

The input parameters of this simulation were the same as listed in table 3.1, except for the upstream density boundary condition $n = 2.1 \times 10^{19}$ m^{-3}, the particle diffusion coefficient $D_n = 0.2$ and the electron and ion thermal diffusivity $\chi_i = \chi_e = 3$ m^{2}s-1. The experiment-code comparison is shown in figure 3.8. The fit is very good. The results resemble the simulation based on the optimised equilibrium; even the employed shift $\Delta Z = 1.8$ mm is similar to the distance between the separatrix position in the standard and optimised equilibrium.

These results show that allowing for profile shifts in interpretative modelling, motivated by inaccuracies in the underlying equilibrium reconstruction, can lead to success in reproducing the experimental results. The size of the shift can be supported by features in the edge plasma. For instance, drift-enabled SOLPS-ITER runs have routinely reproduced the velocity shear layer, where the plasma potential profile peaks and the radial electric field profile passes through zero. This edge plasma phenomenon can be detected with probes and other diagnostics with good spatial accuracy, allowing physics-informed and not just *ad hoc* choice of the shift size. In a sense, the profile shift becomes another input parameter of SOLPS-ITER modelling, adjusted on a spectrum from "freely" to "use a value given by external considerations" in order to achieve the best result. However, it should be kept in mind that an accurate equilibrium reconstruction is much more valuable than shifting the modelled profiles, no matter how well informed the process is.

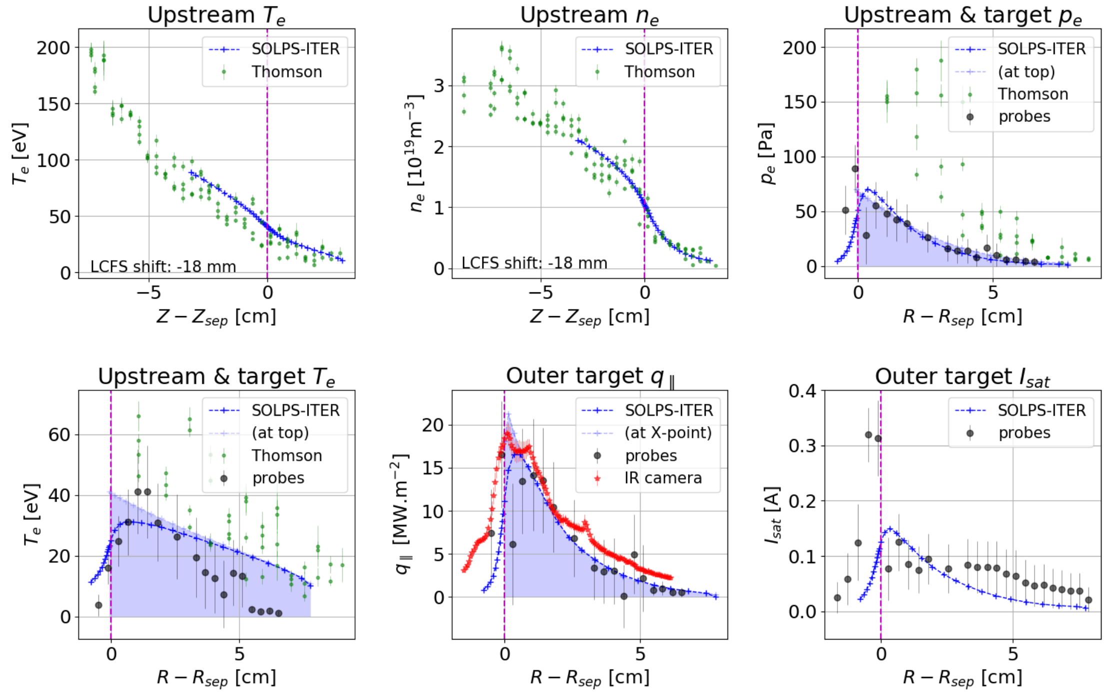

Figure 3.8: Experiment-modelling comparison of the SOLPS-ITER simulation based on the standard EFIT equilibrium reconstruction, allowing for a $\Delta Z = -1.8$ cm shift in the upstream separatrix position.

Equilibrium reconstruction quality impacts more aspects of interpretative modelling than just profile matching; it may be needed to process the diagnostics data or affect the location and magnitude of plasma-wall interaction. Profile shifting may be easier than looking to correct the entire equilibrium reconstruction, which is typically out of the scope of a SOLPS-ITER modeller's expertise, but it is a tool of limited effectiveness and typically low transparency.

An intriguing possibility of future research is reversing the thought process behind shifting profiles to procure code-experiment agreement, and instead using simple SOLPS-ITER simulations to gauge the equilibrium reconstruction quality. Pure deuterium, drift-free SOLPS-ITER simulations seem to capture the physics of simple attached plasmas with low impurity content adequately, while being computationally inexpensive to set up and run. Comparisons such as those in figures 3.6-3.8 can be made for any tokamak to assess its equilibrium reconstruction quality. It is not evident whether such modelling can provide directions *how* to fix the equilibrium reconstruction, but it can be used to compare various reconstruction techniques and choose the more accurate alternative. It is currently planned to perform such modelling for the MAST-U tokamak within the EuroFusion work

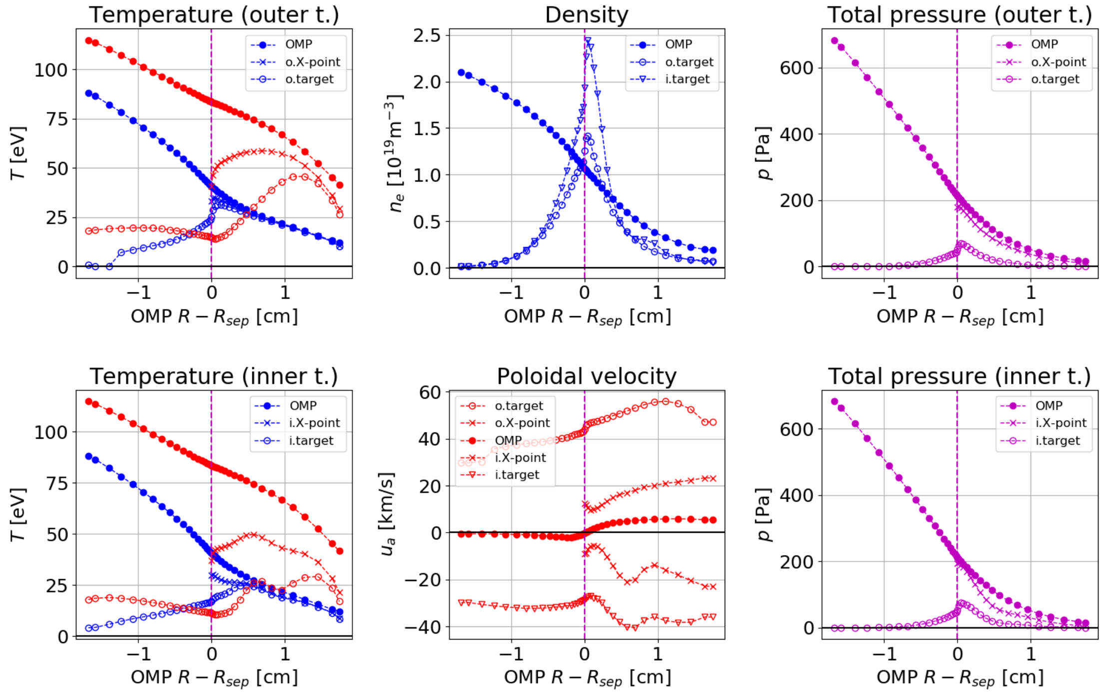

Figure 3.9: Exploration of basic SOLPS-ITER results. Electron = blue, ion = red, both = purple.

package Tokamak Exploitation.

3.4 Interpretative modelling of COMPASS plasma

This section further elaborates details of the simulation based on the optimised equilibrium and its comparison to experiment, see figure 3.7.

The modelled time instance is $t = 1100$ ms, but diagnostic data suitable for the code-model comparison was collected over a longer period, from 1080 ms to 1105 ms. During this time, major plasma parameters (plasma current, line-averaged density, heating power, separatrix position) as well as the diagnostics measurements themselves were checked to be constant. The Thomson scattering diagnostic collected 3 profiles, which are all shown including error bars provided by the spectrum fit procedure. The divertor probe array collected a total of 100,000 samples, which reduces the mean value uncertainty to a value invisible compared to the datapoint size in the plot. Consequently, the plotted errobars were chosen as the fluctuation standard deviation.

Figure 3.9 is a plot of basic SOLPS-ITER results which can be used to quickly gauge the simulation output. It includes temperature and density profiles, poloidal

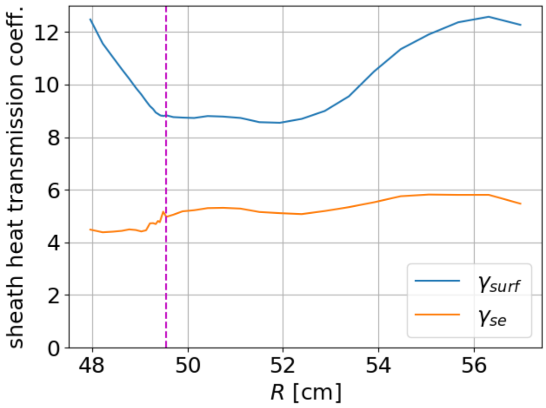

Figure 3.10: Sheath heat transmission coefficient profile.

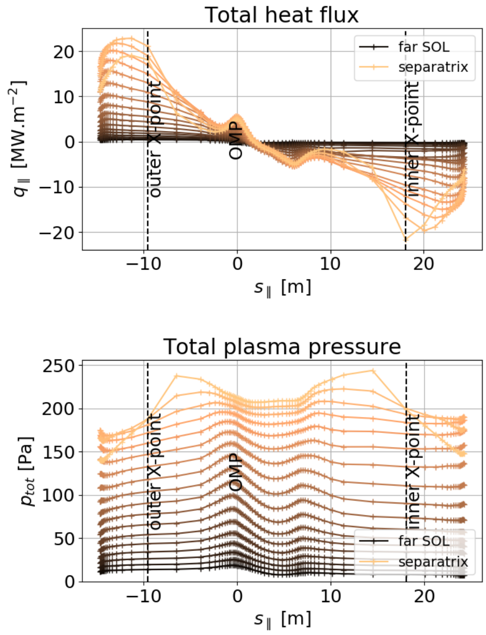

Figure 3.11: Parallel heat flux and total pressure along the SOL flux tubes.

variation of the parallel velocity and total pressure profiles. One observes, for example, that despite electrons and ions having similar boundary conditions (P_{SOL} and χ), $T_i > T_e$ across the entire upstream. There is only a little parallel temperature gradient in electrons, owing to their thermal conductivity even though their overall temperature is lower. Ions, however, feature substantial temperature gradients both to the outer and inner target. This is consistent with their lower thermal conductivity; even though energy convection is relatively more important for ions than for electrons, low thermal conductivity still gives rise to parallel temperature gradients.

Figure 3.10 shows the profile of the sheath heat transmission coefficient calculated from simulation results in two way: as $\gamma_{se} = q_{\parallel}/(en_e c_s)$ and using the non-ambipolar sheath flow [84, Eq. (25.54)] (γ_{surf}). The non-ambipolar γ_{surf} values are close to the value used in processing the divertor probe data, $\gamma = 11$.

Figure 3.11 shows the evolution of the parallel heat flux and total plasma pressure along the SOL flux tubes. These results are interesting for the comparison of kinetic and transport codes and discussing the heat flux limiter value. Here, it informs the choice of "upstream". In the following section, the two-point model analysis is carried out between the outer X-point and the outer target.

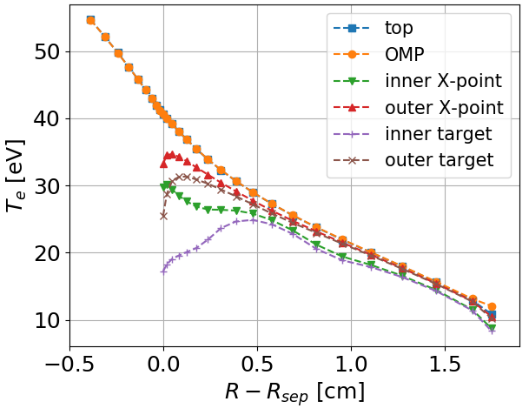

Figure 3.12: Electron temperature poloidal variation.

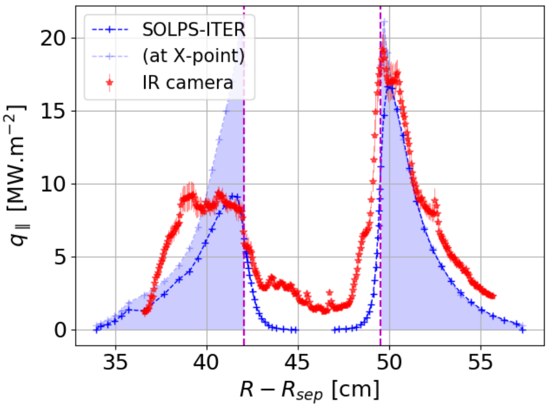

Figure 3.13: Heat flux comparison across the entire divertor target.

Figure 3.12 shows the profiles of electron temperature across several poloidal locations. Evidently, the outer midplane and the plasma top are equivalent choices for the upstream location, and there is little T_e gradient toward the outer target. There is some T_e fall toward the inner target, which is a consequence of the longer connection length. The isothermal SOL corresponds to the sheath-limited regime.

Figure 3.13 shows the experiment-model comparison of the total heat flux to the heat flux measured by the IR camera. One observes a reasonable agreement, with the outer target peak heat flux being about a factor of two higher than the inner target peak heat flux. It is possible that the inner target profile shape was affected by drifts in the divertor area.

3.5 Transport processes in the COMPASS edge plasma

In this section, two-point model formatting (2PMF) [7] is used to gauge the transport processes in the COMPASS edge SOLPS-ITER simulation based on the standard EFIT equilibrium reconstruction employing $\Delta Z = 1.8$ mm shift of the upstream profiles. A parameter scan in P_{SOL} and the upstream density boundary condition n centred around this simulation is presented and the present pressure and power losses are calculated and discussed.

2PMF is a framework which lends basic insights into a transport simulation by providing simple algebraic relations of the simulated plasma parameters and allowing the calculation of pressure and power losses in the SOL. At its heart lies the two-point model [8, Sec. 4], an elementary 0D model concerned with only two locations in the SOL: the upstream, where power enters the SOL via cross-field transport across the separatrix, and the target or downstream, where power is depleted via the sheath encompassing the divertor target. The two-point model does not describe what happens between these two locations (radial transport, atomic processes, plasma species interaction etc.), and in its basic form, it assumes that particles and energy cannot escape the flux tube except at upstream and target. Consequently, the total upstream and downstream pressure are equal $p_u = p_t$ and the total upstream and downstream energy flux in W are also equal, $Q_{\|u} = Q_{\|t}$. (Total means summing over all plasma species and pressure/heat flux types: static and dynamic/convective, conductive and kinetic.) The two-point model is then extended by defining power and pressure losses as a measure of how much these equalities are broken:

$$f_{mom} = 1 - \frac{p_t}{p_u} \qquad (3.1) \qquad\qquad f_{pow} = 1 - \frac{Q_{\|t}}{Q_{\|u}} \qquad (3.2)$$

The momentum loss factor f_{mom} and the power loss factor f_{pow} are opaque, complex variables which contain a wide array of tokamak edge physics but provide no physics explanation of their origin or interaction. Nonetheless, it has been argued based on first principles that the loss factors have at least some physical meaning and predictive function. [7] For instance, momentum losses largely occur by charge exchange, which requires a substantial neutral density. Neutral density peaks just above the divertor target, hence most momentum losses take place here, and hence f_{mom} depends on the plasma parameters just above the target. In particular, when calculated from simulation results using equation (3.1), f_{mom} shows a very strong dependence on the target electron temperature. Thus, one can predict momentum losses based on T_{et}. Although this is far from the complex predictive capabilities needed to design future fusion reactors, the loss factors are useful in simplifying and interpreting results of experiment and interpretative modelling.

Figure 3.14 shows the profiles of $1 - f_{mom}$ and $1 - f_{pow}$, based on the profiles of the total pressure p and parallel heat flux $Q_\|$ at the outer X-point and at the outer target. (The strike point is chosen as the "upstream" location in this case because it features higher p and $Q_\|$ than the outer midplane, which is the other common choice.) The losses are low in both cases, with only exception near the strike point, where the power losses rise up due to radial transport into the private flux region. Flow reversal is observed in the pressure profile near the strike point, with $p_t > p_u$ due to the build-up of particle density. [7] The low losses together with vanishing parallel temperature gradient, apparent in figure 3.8, imply that the plasma is in the sheath-limited regime.

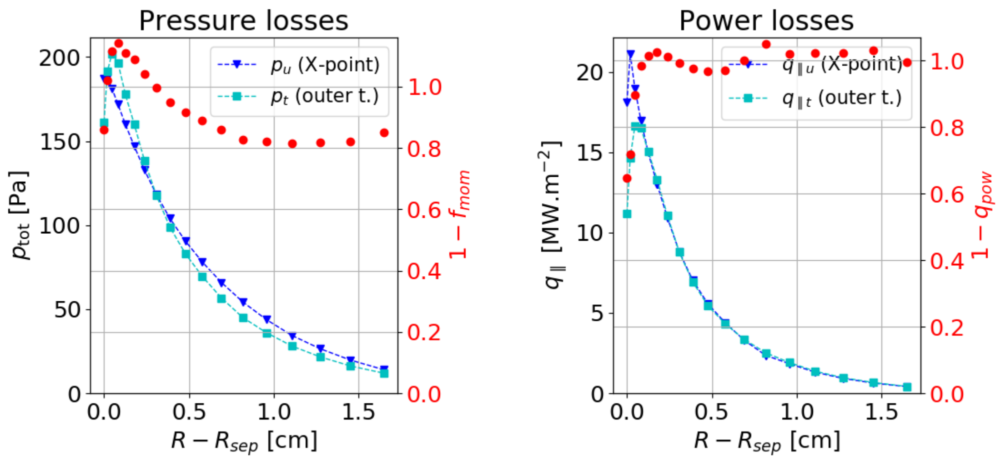

Figure 3.14: Upstream and target profiles of the total pressure p and the total parallel heat flux $q_\parallel$, together with the pressure and power loss factors (in red).

A parameter scan centred around this simulation was carried out, where P_{SOL} and the core flux surface density boundary condition n were varied by -50 %, -20 %, 0 %, +20 % and +50 %. Other boundary conditions and input parameters were left unchanged. The simulations constitute a sensitivity study of the two input parameters and do not replicate the available COMPASS parameter space. Nevertheless, the variation of power and momentum losses within them can be indicative of the plasma states the COMPASS tokamak can be expected to achieve, while being significantly computationally cheaper than choosing individual discharges covering the COMPASS parameter space and performing modelling of each of them.

Figure 3.15 shows the momentum and power losses achieved in the parameter scanned, coded by the upstream-target electron temperature gradient. The greatest T_e gradients are observed at the strike point when momentum and power losses are great. However, as figure 3.16 shows, rollover in the target particle flux is not achieved. This is one of the features of detachment, though according to the $T_{et} < 10$ eV the outer target is already well detached.

2PMF is not only suitable for gauging the transport conditions, but also for making sure one understands the simulation output. Equations (15)-(17) in [7] provide the formulas for recalculating the target electron temperature, electron density and ion flux using the extended two-point model from other simulation outputs. Figure 3.17 reproduces figure 31 in [7] using the parameter scan results. While striving for agreement (aligning the blue points along the 1:1 axis), it was indeed discovered that my understanding of the SOLPS-ITER output was inadequate. This is not only a useful exercise in investigating simulation output

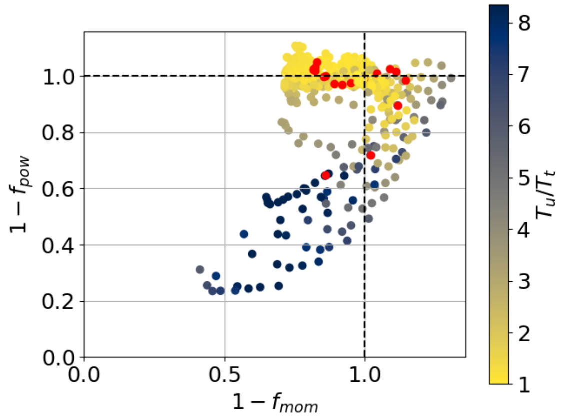

Figure 3.15: Momentum and power losses in the parameter scan.

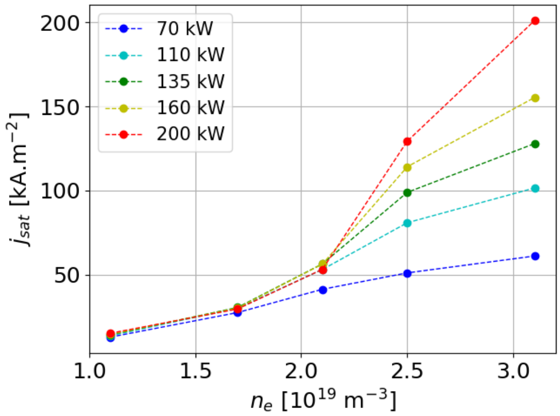

Figure 3.16: Dependency of target flux on the upstream density boundary condition.

composition and meaning, but also demonstrates some usefulness of the two-point model itself, after incorporating corrections for momentum losses, power losses, Mach number variation, ion-electron temperature ratio and flux expansion.

Figure 3.18 shows the electron-ion temperature ratio in the parameter scan, as dependent on the upstream collisionality and the distance from the separatrix. One generally observes hotter electrons near the strike points and hotter ions in the SOL. The difference is up to factor of three. It is yet to be confirmed whether these results are realistic; however, they are consistent with theoretical considerations.

Figure **??** addresses the question whether transport regimes can be reliably gauged using the upstream collisionality criterion: $\nu^* < 10$ means the sheath limited regime and $\nu^* > 15$ means the conduction-limited regime. The blue curve, labeled 2PM, shows the relationship between the upstream collisionality and the parallel temperature gradient derived within the basic two-point model. This curve was used to define the transport regimes in [84]. However, the parameter scan of SOLPS-ITER simulations does not, generally, lie along this line. Depending on the boundary conditions, even large collisionality can feature small temperature gradients and vice versa. The figure shows that the far SOL is generally isothermal no matter its upstream collisionality, while substantial temperature gradients are found near the strike point. Thus, one should keep in mind that transport regimes including detachment have multiple features and complicated structure. Though it is tempting to define a single criterion (collisionality, j_{sat} rollover, substantial pressure losses, $T_{et} < 10$ eV, parallel temperature gradient...), it seems more likely like transport in the tokamak edge must always be assessed from multiple points

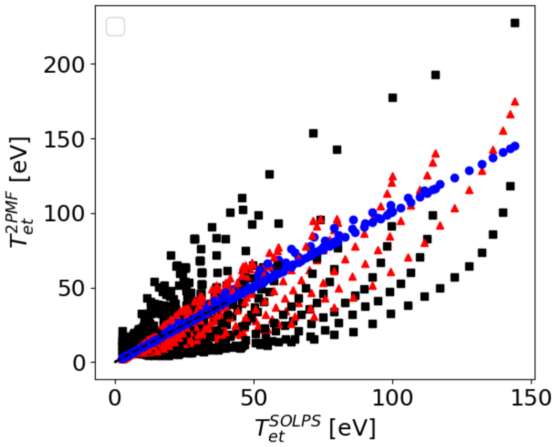

Figure 3.17: 2PMF calculation of the target electron temperature.

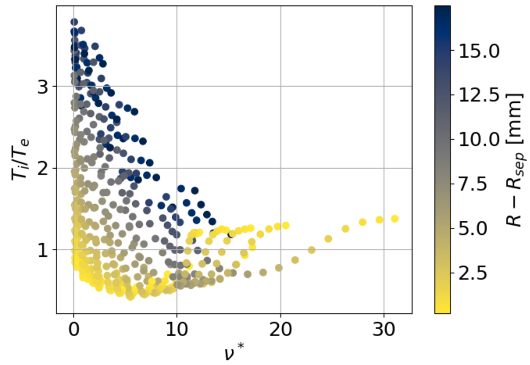

Figure 3.18: Dependency of electron and ion temperature ratio at outer target on the upstream collisionality.

of view.

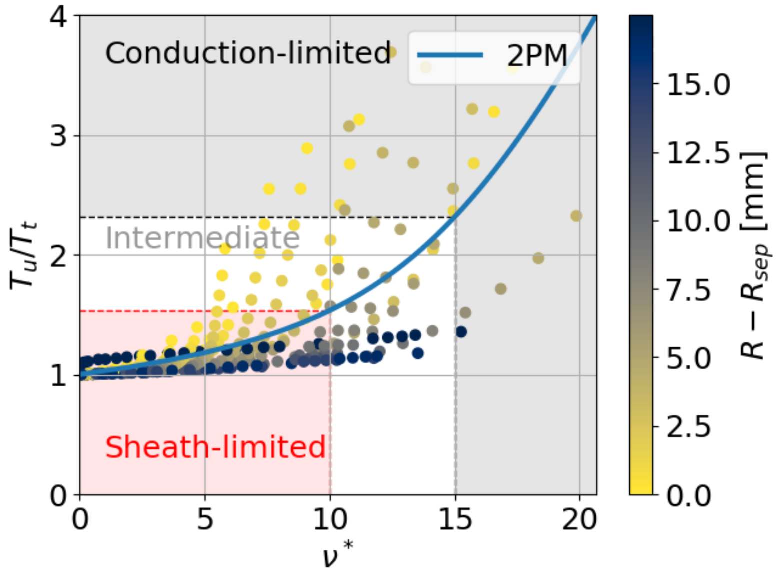

Figure 3.19: Scatterplot of the upstream-downstream electron temperature gradient and the upstream collisionality.

Chapter 4

Conclusion

The subject of this study were SOLPS-ITER simulations of the COMPASS tokamak edge plasma. During the first 5 semesters of my PhD studies, I have learned using the SOLPS-ITER code and interpreting its results in the frame of edge transport. Simple deuterium simulations without drifts have been conducted, demonstrating that SOLPS-ITER has been successfully benchmarked against simple COMPASS plasma and is ready for further employment.

So far the topic of my PhD studies has been "Transport in the COMPASS tokamak edge". Under this umbrella, investigations of equilibrium reconstruction have been conducted and published in the form of a peer-reviewed article. The SOLPS-ITER code has been brought to COMPASS and a small user base has been established. A major step in this direction was the construction of the `solps-doc` GitLab documentation, which contains nearly all of my personal SOLPS-ITER know-how. This not only allows other team members to share the knowledge, but it is also a solid platform to fall back upon in the case of future PhD interruption (which seems likely). SOLPS-ITER has furthermore been calibrated against experimental results and a strong base was setup for performing future simulations of COMPASS and COMPASS Upgrade alike. The next step is to use this base for investigating particular physics of the COMPASS edge plasma.

In the future, it is intended to continue this research in the following manner. Firstly, simulations with intrinsic carbon impurities of the COMPASS discharge #16908 shall be performed, aiming at a comparison of kinetic and transport codes and discussion of the heat flux limiters. Secondly, discharges from a COMPASS nitrogen seeding campaign shall be modelled, aiming to investigate nitrogen radiation and transport and the energy and power losses induced in the edge plasma. If enough time is available, drift simulations will also be set up and divertor drift patterns and edge electric field will be investigated. Since COMPASS is an ITER-like machine and has been employed in scaling studies toward ITER, these investigations should yield valuable insights into the conventional divertor physics.

Bibliography

[1] R.A. Pitts et al. "Physics basis for the first ITER tungsten divertor". In: *Nuclear Materials and Energy* 20 (2019), p. 100696. ISSN: 2352-1791. URL: http://www.sciencedirect.com/science/article/pii/S2352179119300237.

[2] J. Horacek et al. "Modeling of COMPASS tokamak divertor liquid metal experiments". In: *Nuclear Materials and Energy* 25 (2020), p. 100860. ISSN: 2352-1791. DOI: https://doi.org/10.1016/j.nme.2020.100860. URL: http://www.sciencedirect.com/science/article/pii/S2352179120301277.

[3] H. Zohm et al. "On the physics guidelines for a tokamak DEMO". In: *Nuclear Fusion* 53.7 (June 2013), p. 073019. DOI: 10.1088/0029-5515/53/7/073019. URL: https://iopscience.iop.org/article/10.1088/0029-5515/53/7/073019.

[4] J.P. Gunn et al. "Surface heat loads on the ITER divertor vertical targets". In: *Nuclear Fusion* 57.4 (Mar. 2017), p. 046025. DOI: 10.1088/1741-4326/aa5e2a. URL: https://doi.org/10.1088/1741-4326/aa5e2a.

[5] G De Temmerman, T Hirai, and R A Pitts. "The influence of plasma-surface interaction on the performance of tungsten at the ITER divertor vertical targets". In: *Plasma Physics and Controlled Fusion* 60.4 (Mar. 2018), p. 044018. DOI: 10.1088/1361-6587/aaaf62. URL: https://iopscience.iop.org/article/10.1088/1361-6587/aaaf62.

[6] Muyuan Li and Jeong-Ha You. "Interpretation of the deep cracking phenomenon of tungsten monoblock targets observed in high-heat-flux fatigue tests at 20MW/m2". In: *Fusion Engineering and Design* 101 (2015), pp. 1–8. ISSN: 0920-3796. DOI: https://doi.org/10.1016/j.fusengdes.2015.09.008. URL: http://www.sciencedirect.com/science/article/pii/S0920379615302775.

[7] P C Stangeby. "Basic physical processes and reduced models for plasma detachment". In: *Plasma Physics and Controlled Fusion* 60.4 (Mar. 2018), p. 044022. DOI: 10.1088/1361-6587/aaacf6. URL: https://iopscience.iop.org/article/10.1088/1361-6587/aaacf6/meta.

[8] P. Stangeby. *The plasma boundary of magnetic fusion devices*. Philadelphia: Institute of Physics Pub., 2000. ISBN: 07-503-0559-2.

[9] E Sytova. “Modélisation du détachement du plasma ITER et ASDEX Upgrade en utilisant le code SOLPS-ITER avec dérives et courants”. PhD thesis. Aix Marseille Universitè; Ghent University, 2020. URL: https://hal.archives-ouvertes.fr/tel-02617025/document.

[10] ITER Organisation. *SOLPS-ITER example tutorial-DivGeo_ITER_baseline_scenario-InitializeRun*. Sept. 2020.

[11] V. Kotov and D. Reiter. “Two-point analysis of the numerical modelling of detached divertor plasmas”. In: *Plasma Physics and Controlled Fusion* 51.11 (Oct. 2009), p. 115002. DOI: 10.1088/0741-3335/51/11/115002. URL: https://iopscience.iop.org/article/10.1088/0741-3335/51/11/115002/meta.

[12] M Siccinio et al. “A 0D stationary model for the evaluation of the degree of detachment on the divertor plates”. In: *Plasma Physics and Controlled Fusion* 58.12 (Nov. 2016), p. 125011. DOI: 10.1088/0741-3335/58/12/125011. URL: https://iopscience.iop.org/article/10.1088/0741-3335/58/12/125011.

[13] S. Wiesen et al. “The new SOLPS-ITER code package”. In: *Journal of Nuclear Materials* 463 (2015). PLASMA-SURFACE INTERACTIONS 21, pp. 480–484. ISSN: 0022-3115. DOI: https://doi.org/10.1016/j.jnucmat.2014.10.012. URL: http://www.sciencedirect.com/science/article/pii/S0022311514006965.

[14] S. I. Braginskii. “Transport Processes in Plasma”. In: *Reviews of Plasma Physics* 1 (1965), p. 205.

[15] E Havlickova et al. “Benchmarking of a 1D scrape-off layer code SOLF1D with SOLPS and its use in modelling long-legged divertors”. In: *Plasma Physics and Controlled Fusion* 55.6 (May 2013), p. 065004. DOI: 10.1088/0741-3335/55/6/065004. URL: https://iopscience.iop.org/article/10.1088/0741-3335/55/6/065004.

[16] G. V. Pereverzev and P. N. Yushmanov. *ASTRA - Automated System for TRansport Analysis*. Max Planck Institut für Plasmaphysik. Feb. 2002.

[17] H. Bufferand et al. “Implementation of drift velocities and currents in SOLEDGE2D-EIRENE”. In: *Nuclear Materials and Energy* 12 (2017). Proceedings of the 22nd International Conference on Plasma Surface Interactions 2016, 22nd PSI, pp. 852–857. ISSN: 2352-1791. DOI: https://doi.org/10.1016/j.nme.2016.11.031. URL: http://www.sciencedirect.com/science/article/pii/S2352179116301946.

[18] Y. Feng et al. "3D Edge Modeling and Island Divertor Physics". In: *Contributions to Plasma Physics* 44.1-3 (2004), pp. 57–69. DOI: 10.1002/ctpp.200410009. eprint: https://onlinelibrary.wiley.com/doi/pdf/10.1002/ctpp.200410009. URL: https://onlinelibrary.wiley.com/doi/abs/10.1002/ctpp.200410009.

[19] P. Borner. *EIRENE*. accessed on 5 August 2020. URL: http://eirene.de/.

[20] D. A. D'Ippolito, J. R. Myra, and S. J. Zweben. "Convective transport by intermittent blob-filaments". In: *Physics of Plasmas* 18.6 (2011). ISSN: 1070664x. DOI: 10.1063/1.3594609. URL: http://scitation.aip.org/content/aip/journal/pop/18/6/10.1063/1.3594609.

[21] P. Manz et al. "The diffusion limit of ballistic transport in the scrape-off layer". In: *Physics of Plasmas* 27.2 (2020), p. 022506. DOI: 10.1063/1.5133839. eprint: https://doi.org/10.1063/1.5133839. URL: https://doi.org/10.1063/1.5133839.

[22] V. Weinzettl et al. "Progress in diagnostics of the COMPASS tokamak". In: *Journal of Instrumentation* 12.12 (2017), p. C12015. URL: http://stacks.iop.org/1748-0221/12/i=12/a=C12015.

[23] J. Adamek et al. "A novel approach to direct measurement of the plasma potential". In: *Czechoslovak Journal of Physics* 54.3 (2004), pp. 95–99. ISSN: 00114626. DOI: 10.1007/BF03166386. URL: http://link.springer.com/10.1007/BF03166386.

[24] J. P. Graves et al. "Self-similar density turbulence in the TCV tokamak scrape-off layer". In: *Plasma Physics and Controlled Fusion* 47.3 (Feb. 2005), pp. L1–L9. URL: https://iopscience.iop.org/article/10.1088/0741-3335/47/3/L01.

[25] R. Balescu. *Transport processes in plasmas I*. North Holland, New York, 1998.

[26] V. Zhdanov. *Transport Processes in Multicomponent Plasma*. Taylor, Francis, New York, and London, 2002.

[27] P. Kulhanek. *Úvod do teorie plazmatu*. Aldebaran Group for Astrophysics, 2011.

[28] D. P. Coster et al. *SOLPS-ITER manual*. SOLPS-ITER version 3.0.6-490-g76379a8.

[29] F. I. Parra. *Braginskii fluid equations*. Rudolf Peierls Centre for Theoretical Physics, University of Oxford. 2019. URL: http://www-thphys.physics.ox.ac.uk/people/FelixParra/CollisionalPlasmaPhysics/notes/lecIV%5C_braginskii.pdf.

[30] J. Wesson and D. Campbell. *Tokamaks*. 4th ed. New York: Oxford University Press, 2011. ISBN: 0199592233.

[31] R. Schneider et al. “Plasma Edge Physics with B2-Eirene”. In: *Contributions to Plasma Physics* 46.1-2 (2006), pp. 3–191. DOI: 10.1002/ctpp.200610001. eprint: https://onlinelibrary.wiley.com/doi/pdf/10.1002/ctpp.200610001. URL: https://onlinelibrary.wiley.com/doi/abs/10.1002/ctpp.200610001.

[32] W Fundamenski. “Parallel heat flux limits in the tokamak scrape-off layer”. In: *Plasma Physics and Controlled Fusion* 47.11 (Oct. 2005), R163–R208. DOI: 10.1088/0741-3335/47/11/r01. URL: https://doi.org/10.1088/0741-3335/47/11/r01.

[33] D. Tskhakaya et al. “On Kinetic Effects during Parallel Transport in the SOL”. In: *Contributions to Plasma Physics* 48.1-3 (2008), pp. 89–93. DOI: https://doi.org/10.1002/ctpp.200810015. eprint: https://onlinelibrary.wiley.com/doi/pdf/10.1002/ctpp.200810015. URL: https://onlinelibrary.wiley.com/doi/abs/10.1002/ctpp.200810015.

[34] D. Tskhakaya et al. “Kinetic model of the COMPASS tokamak SOL”. In: *Nuclear Materials and Energy* 26 (2021), p. 100893. ISSN: 2352-1791. DOI: https://doi.org/10.1016/j.nme.2020.100893. URL: http://www.sciencedirect.com/science/article/pii/S2352179120301551.

[35] J T Omotani and B D Dudson. “Non-local approach to kinetic effects on parallel transport in fluid models of the scrape-off layer”. In: *Plasma Physics and Controlled Fusion* 55.5 (Apr. 2013), p. 055009. DOI: 10.1088/0741-3335/55/5/055009. URL: https://doi.org/10.1088/0741-3335/55/5/055009.

[36] D. Coster. *Personal communication*. Oct. 2019.

[37] Jae-Sun Park, Xavier Bonnin, and Richard Pitts. “Assessment of ITER divertor performance during early operation phases”. In: *Nuclear Fusion* 61.1 (Dec. 2020), p. 016021. DOI: 10.1088/1741-4326/abc1ce. URL: https://doi.org/10.1088/1741-4326/abc1ce.

[38] B. J. Braams. “Computational studies in tokamak equilibrium and transport”. PhD thesis. Rijksuniversiteit Utrecht (Netherlands), 1982.

[39] R. Panek et al. “Reinstallation of the COMPASS-D tokamak in IPP ASCR”. In: *Czechoslovak Journal of Physics* 56.S2 (2006), B125–B137. ISSN: 0011-4626. DOI: 10.1007/s10582-006-0188-1. URL: http://link.springer.com/10.1007/s10582-006-0188-1.

[40] IPP Prague. *Tokamak COMPASS Parameters*. URL: http://www.ipp.cas.cz/vedecka%5C_struktura%5C_ufp/tokamak/tokamak%5C_compass/.

[41] R. Panek et al. "Status of the COMPASS tokamak and characterization of the first H-mode". In: *Plasma Physics and Controlled Fusion* vol. 58.issue 1 (Jan. 1, 2016), p. 014015. ISSN: 07413335. DOI: 10.1088/0741-3335/58/1/014015. URL: http://stacks.iop.org/0741-3335/58/i=1/a=014015?key=crossref.cbd9509a544f4d9eb76fe62b71a66a58.

[42] M. Spolaore et al. "Electromagnetic ELM and inter-ELM filaments detected in the COMPASS Scrape-Off Layer". In: *Nuclear Materials and Energy* 12 (2017). Proceedings of the 22nd International Conference on Plasma Surface Interactions 2016, 22nd PSI, pp. 844–851. ISSN: 2352-1791. DOI: https://doi.org/10.1016/j.nme.2016.12.014. URL: https://www.sciencedirect.com/science/article/pii/S2352179116301934.

[43] J. Adamek et al. "Electron temperature and heat load measurements in the COMPASS divertor using the new system of probes". In: *Nuclear Fusion* 57.11 (2017), p. 116017. URL: http://stacks.iop.org/0029-5515/57/i=11/a=116017.

[44] D. Carralero et al. "Implications of high density operation on SOL transport: A multimachine investigation". In: *Journal of Nuclear Materials* 463 (2015). PLASMA-SURFACE INTERACTIONS 21, pp. 123–127. ISSN: 0022-3115. DOI: https://doi.org/10.1016/j.jnucmat.2014.10.019. URL: https://www.sciencedirect.com/science/article/pii/S002231151400703X.

[45] E. Stefanikova et al. "Fitting of the Thomson scattering density and temperature profiles on the COMPASS tokamak". In: *Review of Scientific Instruments* 87.11 (2016), 11E536. DOI: 10.1063/1.4961554. eprint: https://aip.scitation.org/doi/pdf/10.1063/1.4961554. URL: https://aip.scitation.org/doi/abs/10.1063/1.4961554.

[46] M. Komm et al. "First detachment studies on COMPASS tokamak using nitrogen seeding". In: *44th EPS Conference on Plasma Physics*. 2017.

[47] E. Stefanikova et al. "Effect of the relative shift between the electron density and temperature pedestal position on the pedestal stability in JET-ILW and comparison with JET-C". In: *Nuclear Fusion* 58.5 (Mar. 2018), p. 056010. DOI: 10.1088/1741-4326/aab216. URL: https://doi.org/10.1088/1741-4326/aab216.

[48] O. Grover et al. "Limit cycle oscillations measurements with Langmuir and ball-pen probes on COMPASS". In: *Nuclear Fusion* 58.11 (Oct. 2018), p. 112010. DOI: 10.1088/1741-4326/aabb19. URL: https://doi.org/10.1088/1741-4326/aabb19.

[49] J. Adamek et al. "Fast measurements of the electron temperature and parallel heat flux in ELMy H-mode on the COMPASS tokamak". In: *Nuclear Fusion* 57.2 (Sept. 2016), p. 022010. DOI: 10.1088/0029-5515/57/2/022010. URL: https://doi.org/10.1088/0029-5515/57/2/022010.

[50] T. Markovic et al. "Measurements and modelling of plasma response field to RMP on the COMPASS tokamak". In: *Nuclear Fusion* 56.9 (July 2016), p. 092010. DOI: 10.1088/0029-5515/56/9/092010. URL: https://doi.org/10.1088/0029-5515/56/9/092010.

[51] F. Camilo de Souza et al. "Geodesic mode instability driven by electron and ion fluxes during neutral beam injection in tokamaks". In: *Physics Letters A* 381.36 (2017), pp. 3066–3070. ISSN: 0375-9601. DOI: https://doi.org/10.1016/j.physleta.2017.07.033. URL: https://www.sciencedirect.com/science/article/pii/S0375960117306989.

[52] J. Seidl et al. "Electromagnetic characteristics of geodesic acoustic mode in the COMPASS tokamak". In: *Nuclear Fusion* 57.12 (Dec. 1, 2017), p. 126048. ISSN: 0029-5515. DOI: 10.1088/1741-4326/aa897e. URL: http://stacks.iop.org/0029-5515/57/i=12/a=126048?key=crossref.8e41de493084efddc3884bd2b69878d2.

[53] R. Dejarnac et al. "Understanding narrow SOL power flux component in COMPASS limiter plasmas by use of Langmuir probes". In: *Journal of Nuclear Materials* 463 (2015). PLASMA-SURFACE INTERACTIONS 21, pp. 381–384. ISSN: 0022-3115. DOI: https://doi.org/10.1016/j.jnucmat.2014.12.100. URL: https://www.sciencedirect.com/science/article/pii/S0022311514010538.

[54] M. Kocan et al. "Modelling ELM heat flux deposition on the ITER main chamber wall". In: *Journal of Nuclear Materials* vol. 463.1 (2015), pp. 709–713. ISSN: 00223115. DOI: 10.1016/j.jnucmat.2014.11.130. URL: http://linkinghub.elsevier.com/retrieve/pii/S0022311514009374.

[55] J. Horacek et al. "Narrow heat flux channels in the COMPASS limiter scrape-off layer". In: *Journal of Nuclear Materials* 463 (2015). PLASMA-SURFACE INTERACTIONS 21, pp. 385–388. ISSN: 0022-3115. DOI: https://doi.org/10.1016/j.jnucmat.2014.11.132. URL: https://www.sciencedirect.com/science/article/pii/S0022311514009398.

[56] J. Horacek et al. "Multi-machine scaling of the main SOL parallel heat flux width in tokamak limiter plasmas". In: *Plasma Physics and Controlled Fusion* vol. 58.issue 7 (July 1, 2016), p. 074005. ISSN: 07413335. DOI: 10.1088/0741-3335/58/7/074005. URL: http://stacks.iop.org/0741-3335/58/i=7/a=074005?key=crossref.82c59846a9ca0582d8eea37c24368b57.

[57] M. Komm et al. "Divertor impurity seeding experiments at the COMPASS tokamak". In: *Nuclear Fusion* 59.10 (Sept. 2019), p. 106035. DOI: 10.1088/1741-4326/ab34d2. URL: https://doi.org/10.1088/1741-4326/ab34d2.

[58] C Silva et al. "Comparison of fluctuations properties measured by Langmuir and ball-pen probes in the ISTTOK boundary plasma". In: *Plasma Physics and Controlled Fusion* 57.2 (Dec. 2014), p. 025003. DOI: 10.1088/0741-3335/57/2/025003. URL: https://doi.org/10.1088/0741-3335/57/2/025003.

[59] N. R. Walkden et al. "Profile measurements in the plasma edge of mega amp spherical tokamak using a ball pen probe". In: *Review of Scientific Instruments* 86.2 (2015), p. 023510. DOI: 10.1063/1.4908572. eprint: https://doi.org/10.1063/1.4908572. URL: https://doi.org/10.1063/1.4908572.

[60] Jordan Cavalier et al. "Tomographic reconstruction of tokamak edge turbulence from single visible camera data and automatic turbulence structure tracking". In: *Nuclear Fusion* 59.5 (Apr. 2019), p. 056025. DOI: 10.1088/1741-4326/ab0d4c. URL: https://doi.org/10.1088/1741-4326/ab0d4c.

[61] O. Grover et al. "First simultaneous measurements of Reynolds stress with ball-pen and Langmuir probes". In: *Review of Scientific Instruments* 88.6 (2017). ISSN: 0034-6748. DOI: 10.1063/1.4984240. URL: http://aip.scitation.org/doi/10.1063/1.4984240.

[62] R. Dejarnac et al. "Overview of power exhaust experiments in the COMPASS divertor with liquid metals". In: *Nuclear Materials and Energy* 25 (2020), p. 100801. ISSN: 2352-1791. DOI: https://doi.org/10.1016/j.nme.2020.100801. URL: http://www.sciencedirect.com/science/article/pii/S2352179120300776.

[63] A V Melnikov et al. "Quasicoherent modes on the COMPASS tokamak". In: *Plasma Physics and Controlled Fusion* 57.6 (Apr. 2015), p. 065006. DOI: 10.1088/0741-3335/57/6/065006. URL: https://doi.org/10.1088/0741-3335/57/6/065006.

[64] I. Borodkina et al. "An Analytical Expression for the Electric Field and Particle Tracing in Modelling of Be Erosion Experiments at the JET ITER-like Wall". In: *Contributions to Plasma Physics* 56.6-8 (2016), pp. 640–645. DOI: https://doi.org/10.1002/ctpp.201610032. eprint: https://onlinelibrary.wiley.com/doi/pdf/10.1002/ctpp.201610032. URL: https://onlinelibrary.wiley.com/doi/abs/10.1002/ctpp.201610032.

[65] Jordan Cavalier et al. "Strongly emissive plasma-facing material under space-charge limited regime: Application to emissive probes". In: *Physics of Plasmas* 24.1 (2017), p. 013506. DOI: 10.1063/1.4973557. eprint: https://doi.org/10.1063/1.4973557. URL: https://doi.org/10.1063/1.4973557.

[66] R. Dejarnac et al. "Heat loads on poloidal and toroidal edges of castellated plasma-facing components in COMPASS". In: *Nuclear Fusion* 58.6 (Apr. 2018), p. 066003. DOI: 10.1088/1741-4326/aab973. URL: https://doi.org/10.1088/1741-4326/aab973.

[67] O. Ficker et al. "Runaway electron beam stability and decay in COMPASS". In: *Nuclear Fusion* 59.9 (Aug. 2019), p. 096036. DOI: 10.1088/1741-4326/ab210f. URL: https://doi.org/10.1088/1741-4326/ab210f.

[68] O. Ficker et al. "Losses of runaway electrons in MHD-active plasmas of the COMPASS tokamak". In: *Nuclear Fusion* 57.7 (May 2017), p. 076002. DOI: 10.1088/1741-4326/aa6aba. URL: https://doi.org/10.1088/1741-4326/aa6aba.

[69] S.N. Gerasimov et al. "JET and COMPASS asymmetrical disruptions". In: *Nuclear Fusion* 55.11 (Sept. 2015), p. 113006. DOI: 10.1088/0029-5515/55/11/113006. URL: https://doi.org/10.1088/0029-5515/55/11/113006.

[70] J Mlynar et al. "Runaway electron experiments at COMPASS in support of the EUROfusion ITER physics research". In: *Plasma Physics and Controlled Fusion* 61.1 (Nov. 2018), p. 014010. DOI: 10.1088/1361-6587/aae04a. URL: https://doi.org/10.1088/1361-6587/aae04a.

[71] Milos Vlainic et al. "Post-disruptive runaway electron beams in the COMPASS tokamak". In: *Journal of Plasma Physics* 81.5 (2015), p. 475810506. DOI: 10.1017/S0022377815000914.

[72] V.V. Plyusnin et al. "Comparison of runaway electron generation parameters in small, medium-sized and large tokamaks - A survey of experiments in COMPASS, TCV, ASDEX-Upgrade and JET". In: *Nuclear Fusion* 58.1 (Nov. 2017), p. 016014. DOI: 10.1088/1741-4326/aa8f05. URL: https://doi.org/10.1088/1741-4326/aa8f05.

[73] Radomir Panek et al. "Conceptual design of the COMPASS upgrade tokamak". In: *Fusion Engineering and Design* 123 (2017). Proceedings of the 29th Symposium on Fusion Technology (SOFT-29) Prague, Czech Republic, September 5-9, 2016, pp. 11–16. ISSN: 0920-3796. DOI: https://doi.org/10.1016/j.fusengdes.2017.03.002. URL: http://www.sciencedirect.com/science/article/pii/S0920379617302053.

[74] Michael Komm et al. “Power exhaust by core radiation at COMPASS tokamak”. In: *Nuclear Fusion* (2020). URL: http://iopscience.iop.org/article/10.1088/1741-4326/abd3ea.

[75] A.V. Chankina et al. “Possible influence of near SOL plasma on the H-mode power threshold”. In: *Nuclear Materials and Energy* 12 (2017). Proceedings of the 22nd International Conference on Plasma Surface Interactions 2016, 22nd PSI, pp. 273–277. ISSN: 2352-1791. DOI: https://doi.org/10.1016/j.nme.2016.10.004. URL: http://www.sciencedirect.com/science/article/pii/S2352179116300382.

[76] J. Seidl et al. “Dependence of the L-H power threshold on the X-point height in the COMPASS tokamak”. In: *17th International Workshop on H-mode Physics and Transport Barriers*. Oct. 11, 2019.

[77] V. Rozhansky et al. “Modeling of electric fields in tokamak edge plasma and LH transition”. In: *28th European Physical Society Conference on Controlled Fusion and Plasma Physics, Funchal, Madeira* (Jan. 2001).

[78] V. Rozhansky et al. “Currents structure in the scrape-off layer of a tokamak”. In: *Nuclear Materials and Energy* 25 (2020), p. 100840. ISSN: 2352-1791. DOI: https://doi.org/10.1016/j.nme.2020.100840. URL: http://www.sciencedirect.com/science/article/pii/S2352179120301095.

[79] L.C Appel, M.K Bevir, and M.J Walsh. “Equilibrium reconstruction in the START tokamak”. In: *Nuclear Fusion* 41.2 (Feb. 2001), pp. 169–180. DOI: 10.1088/0029-5515/41/2/303. URL: https://doi.org/10.1088/0029-5515/41/2/303.

[80] Josef Havlicek. “Study of Equilibrium Magnetic Configuration in Tokamak Type Devices”. PhD thesis. Faculty of Mathematics and Physics, Charles University in Prague, Sept. 1, 2015.

[81] O. Kovanda et al. “Dependence of reconstructed equilibria on input data sets using EFIT onCOMPASS and comparison with experimental observations”. In: *46th EPS conference on plasma physics proceedings*. July 8, 2019. URL: http://ocs.ciemat.es/EPS2019PAP/pdf/P4.1032.pdf.

[82] K. Jirakova et al. “Systematic errors in tokamak magnetic equilibrium reconstruction: a study of EFIT++ at tokamak COMPASS”. In: *Journal of Instrumentation* 14.11 (Nov. 2019), pp. C11020–C11020. DOI: 10.1088/1748-0221/14/11/c11020. URL: https://iopscience.iop.org/article/10.1088/1748-0221/14/11/C11020.

[83] G. D. Porter et al. "Characterization of the separatrix plasma parameters in DIII-D". In: *Physics of Plasmas* 5.5 (1998), pp. 1410–1422. ISSN: 1070-664X. DOI: 10.1063/1.872830. URL: http://aip.scitation.org/doi/10.1063/1.872830.

[84] P.C. Stangeby et al. "Identifying the location of the OMP separatrix in DIII-D using power accounting". In: *Nuclear Fusion* 55.9 (Aug. 2015), p. 093014. DOI: 10.1088/0029-5515/55/9/093014. URL: https://doi.org/10.1088/0029-5515/55/9/093014.

[85] K. McCormick et al. "ITER edge database investigations of the SOL width". In: *Journal of Nuclear Materials* 266-269 (1999), pp. 99–108. ISSN: 0022-3115. DOI: https://doi.org/10.1016/S0022-3115(98)00521-2. URL: https://www.sciencedirect.com/science/article/pii/S0022311598005212.

[86] J.D. Callen et al. "Analysis of pedestal plasma transport". In: *Nuclear Fusion* 50.6 (May 2010), p. 064004. DOI: 10.1088/0029-5515/50/6/064004. URL: https://doi.org/10.1088/0029-5515/50/6/064004.

[87] J. Boedo et al. "A review of direct experimental measurements of detachment". In: *Plasma Physics and Controlled Fusion* 60.4 (2018), p. 044008. URL: http://stacks.iop.org/0741-3335/60/i=4/a=044008.

[88] A Kallenbach et al. "EDGE2D modelling of edge profiles obtained in JET diagnostic optimized configuration". In: *Plasma Physics and Controlled Fusion* 46.3 (Jan. 2004), pp. 431–446. DOI: 10.1088/0741-3335/46/3/001. URL: https://doi.org/10.1088/0741-3335/46/3/001.

[89] M Kocan and J P Gunn. "Comparison of scrape-off layer profiles in outboard-versus inboard-limited plasmas in Tore Supra". In: *Plasma Physics and Controlled Fusion* 52.4 (Mar. 2010), p. 045010. DOI: 10.1088/0741-3335/52/4/045010. URL: https://doi.org/10.1088/0741-3335/52/4/045010.

[90] D.L. Rudakov et al. "SOL width in limited versus diverted discharges in DIII-D". In: *Journal of Nuclear Materials* 415.1, Supplement (2011). Proceedings of the 19th International Conference on Plasma-Surface Interactions in Controlled Fusion, S387–S390. ISSN: 0022-3115. DOI: https://doi.org/10.1016/j.jnucmat.2010.10.036. URL: https://www.sciencedirect.com/science/article/pii/S0022311510006161.

[91] H. J. Sun et al. "Study of near SOL decay lengths in ASDEX Upgrade under attached and detached divertor conditions". In: *Plasma Physics and Controlled Fusion* 59.10 (2017), p. 105010. URL: http://stacks.iop.org/0741-3335/59/i=10/a=105010.

[92] J. Brotankova et al. "Measurement of sheared flows in the edge plasma of the CASTOR tokamak". In: *Plasma Physics Reports* 35.11 (2009), pp. 980–986. ISSN: 1063780x. DOI: 10.1134/S1063780X09110087. URL: http://link.springer.com/10.1134/S1063780X09110087.

[93] J. Adamek et al. "Direct Plasma Potential Measurements by Ball-Pen Probe and Self-Emitting Langmuir Probe on COMPASS and ASDEX Upgrade". In: *Contributions to Plasma Physics* 54.3 (2014), pp. 279–284. ISSN: 08631042. DOI: 10.1002/ctpp.201410072. URL: http://doi.wiley.com/10.1002/ctpp.201410072.

[94] K. Uehara et al. "Direct Identification of Magnetic Surface by a Differential Double Probe in JFT-2M". In: *Japanese Journal of Applied Physics* 45.No. 24 (June 2006), pp. L630–L633. DOI: 10.1143/jjap.45.l630. URL: https://doi.org/10.1143/jjap.45.l630.

[95] Y Nagashima et al. "Boundary of the geodesic acoustic eigenmode in the vicinity of the magnetic separatrix". In: *Plasma Physics and Controlled Fusion* 51.6 (May 2009), p. 065019. DOI: 10.1088/0741-3335/51/6/065019. URL: https://doi.org/10.1088/0741-3335/51/6/065019.

[96] Y Nagashima et al. "In search of zonal flows by using direct density fluctuation measurements". In: *Plasma Physics and Controlled Fusion* 49.10 (Aug. 2007), pp. 1611–1625. DOI: 10.1088/0741-3335/49/10/002. URL: https://doi.org/10.1088/0741-3335/49/10/002.

[97] Katerina Jirakova. "Study of edge plasma of tokamak COMPASS and its poloidal variations". MA thesis. Faculty of Nuclear Sciences and Physical Engineering, Czech Technical University, Czech Republic, Sept. 30, 2018.

[98] K. Jirakova et al. "Separatrix detection in tokamaks using electric probes". In: *Fusenet PhD Event 2018, CEA Cadarache, France*. Nov. 6, 2018.

[99] K. Jirakova et al. "Non-magnetic edge diagnostics for detecting the separatrix position". In: *ECPD 2019 Book of Abstracts*. Lisboa University, 2019. URL: https://www.ipfn.tecnico.ulisboa.pt/ECPD2019/pdf/ecpd2019%5C_book%5C_of%5C_abstracts.pdf.

[100] B. Braams. *B2.5 code fact sheet*. accessed on 29 July 2020. URL: https://w3.pppl.gov/topdac/b2.htm.

[101] D. Coster et al. "Further Developments of the Edge Transport Simulation Package, SOLPS". In: *19th Fusion Energy Conference Proceedings*. 2002. URL: https://www-pub.iaea.org/MTCD/publications/PDF/csp%5C_019c/pdf/thp2%5C_13.pdf.

[102] A. S. Kukushkin et al. "Effect of neutral transport on ITER divertor performance". In: *Nuclear Fusion* 45.7 (June 2005), pp. 608–616. DOI: 10.1088/0029-5515/45/7/008. URL: https://iopscience.iop.org/article/10.1088/0029-5515/45/7/008/meta.

[103] A. S. Kukushkin et al. "Finalizing the ITER divertor design: The key role of SOLPS modeling". In: *Fusion Engineering and Design* 86.12 (2011), pp. 2865–2873. ISSN: 0920-3796. DOI: https://doi.org/10.1016/j.fusengdes.2011.06.009. URL: http://www.sciencedirect.com/science/article/pii/S092037961100514X.

[104] F. Reimold et al. "Experimental studies and modeling of complete H-mode divertor detachment in ASDEX Upgrade". In: *Journal of Nuclear Materials* 463 (2015). PLASMA-SURFACE INTERACTIONS 21, pp. 128–134. ISSN: 0022-3115. DOI: https://doi.org/10.1016/j.jnucmat.2014.12.019. URL: http://www.sciencedirect.com/science/article/pii/S002231151400960X.

[105] X. Bonnin, A. Kukushkin, and David Coster. "Code development for ITER edge modelling - SOLPS5.1". In: *Journal of Nuclear Materials - J NUCL MATER* 390 (Jan. 2009), pp. 274–277.

[106] V. Rozhansky et al. "New B2SOLPS5.2 transport code for H-mode regimes in tokamaks". In: *Nuclear Fusion* 49.2 (Jan. 2009), p. 025007. DOI: 10.1088/0029-5515/49/2/025007. URL: https://iopscience.iop.org/article/10.1088/0029-5515/49/2/025007.

[107] I. Paradela Perez et al. "Impact of drifts in the ASDEX upgrade upper open divertor using SOLPS-ITER". In: *Contributions to Plasma Physics* 60.5-6 (2020), e201900166. DOI: 10.1002/ctpp.201900166. eprint: https://onlinelibrary.wiley.com/doi/pdf/10.1002/ctpp.201900166. URL: https://onlinelibrary.wiley.com/doi/abs/10.1002/ctpp.201900166.

[108] B. Gulejova. "SOLPS Modelling of ELMing H-mode". PhD thesis. École Polytechnique Fédérale de Lausanne, 2010.

[109] J. F. Luciani and P. Mora. "Nonlocal heat transport due to steep temperature gradients". In: *Physical Review Letters* 51.18 (1983), pp. 1664–1667.

[110] ITER Organisation. *SOLPS-ITER Github*. accessed in August 2020. URL: https://git.iter.org/projects/BND/repos/solps-iter/browse.

[111] Eurofusion wiki. *Gateway ENEA/CINECA*. accessed in August 2020. URL: https://wiki.eufus.eu/doku.php.

[112] C. K. Tsui et al. "Poloidal asymmetry in the narrow heat flux feature in the TCV scrape-off layer". In: *Physics of Plasmas* 24.6 (2017), p. 062508. ISSN: 1070-664X. DOI: 10.1063/1.4985075. URL: http://aip.scitation.org/doi/10.1063/1.4985075.

[113] T. D. Rognlien et al. "Two-dimensional electric fields and drifts near the magnetic separatrix in divertor tokamaks". In: *Physics of Plasmas* 6.5 (1999), pp. 1851–1857. DOI: 10.1063/1.873488. eprint: https://doi.org/10.1063/1.873488. URL: https://doi.org/10.1063/1.873488.

[114] P. Manz et al. "Origin and turbulence spreading of plasma blobs". In: *Physics of Plasmas* 22.2 (2015), p. 022308. DOI: 10.1063/1.4908272. eprint: https://doi.org/10.1063/1.4908272. URL: https://doi.org/10.1063/1.4908272.

[115] M. Dorf and M. Dorr. "Continuum kinetic modelling of cross-separatrix plasma transport in a tokamak edge including self-consistent electric fields". In: *Contributions to Plasma Physics* 58.6-8 (2018), pp. 434–444. DOI: 10.1002/ctpp.201700137. eprint: https://onlinelibrary.wiley.com/doi/pdf/10.1002/ctpp.201700137. URL: https://onlinelibrary.wiley.com/doi/abs/10.1002/ctpp.201700137.

[116] B. Nold et al. "Generation of blobs and holes in the edge of the ASDEX Upgrade tokamak". In: *Plasma Physics and Controlled Fusion* 52.6 (Apr. 2010), p. 065005. DOI: 10.1088/0741-3335/52/6/065005. URL: https://iopscience.iop.org/article/10.1088/0741-3335/52/6/065005.

[117] G.S. Xu et al. "Blob/hole formation and zonal-flow generation in the edge plasma of the JET tokamak". In: *Nuclear Fusion* 49.9 (Aug. 2009), p. 092002. DOI: 10.1088/0029-5515/49/9/092002. URL: https://iopscience.iop.org/article/10.1088/0029-5515/49/9/092002/meta.

[118] I. P. Perez and F. Hitzler. *SOLPSpy*. accessed in August 2020. URL: https://gitlab.aug.ipp.mpg.de/ipar/solpspy.

[119] The COMPASS team. *pyCDB*. accessed in August 2020. URL: https://cdb.readthedocs.io/en/latest/index.html.

[120] The COMPASS team. *SOLPS-COMPASS*. accessed in August 2020. URL: https://repo.tok.ipp.cas.cz/jirakova/solps-compass.

Appendix A

Article published in JINST, 2019

JINST

Published by IOP Publishing for Sissa Medialab

Received: *June 29, 2019*
Revised: *October 27, 2019*
Accepted: *November 2, 2019*
Published: *November 20, 2019*

3rd European Conference on Plasma Diagnostics (ECPD2019)
6–10 May 2019
Lisbon, Portugal

Systematic errors in tokamak magnetic equilibrium reconstruction: a study of EFIT++ at tokamak COMPASS

K. Jirakova,[a,b,1] O. Kovanda,[a,c] J. Adamek,[a] M. Komm[a] and J. Seidl[a]

[a] *Institute of Plasma Physics, Czech Academy of Sciences, Za Slovankou 3, 182 00 Prague, Czech Republic*

[b] *Faculty of Nuclear Sciences and Physical Engineering, Czech Technical University, Brehova 7, 115 19 Prague, Czech Republic*

[c] *Faculty of Mathematics and Physics, Charles University, Ke Karlovu 3, 121 16 Prague, Czech Republic*

E-mail: jirakova@ipp.cas.cz

Abstract: Uncertainties and errors in magnetic equilibrium reconstructions are a wide-spread problem in interpreting experimental data measured in the tokamak edge. This study demonstrates errors in EFIT++ reconstructions performed on the COMPASS tokamak by comparing the outer midplane separatrix position to the Velocity Shear Layer (VSL) position. The VSL is detected as the plasma potential peak measured by a reciprocating ball-pen probe. A subsequent statistical analysis of nearly 400 discharges shows a strong systematic trend in the reconstructed separatrix position relative to the VSL, where the primary factors are plasma triangularity and the magnetic axis radial position. This dependency is significantly reduced after the measuring coils positions as recorded in EFIT input are optimised to provide a closer match between the "synthetic" coil signal calculated by the Biot-Savart law in a vacuum discharge and the actual coil signal. In conclusion, we suggest that applying this optimisation may lead to more accurate and reliable reconstructions of the COMPASS equilibrium, which would have a positive impact on the accuracy of measurement analysis performed in the edge plasma.

Keywords: Plasma diagnostics - probes; Analysis and statistical methods

[1]Corresponding author.

https://doi.org/10.1088/1748-0221/14/11/C11020

2019 JINST 14 C11020

Contents

1 Introduction

Magnetic equilibrium reconstruction is a vital component in interpreting experimental data collected in the tokamak edge region. However, many tokamak studies have reported problems in interpreting edge data caused by uncertanties in the equilibrium reconstruction (for example [1–5]). The COMPASS tokamak is no exception. One of the known issues of its EFIT++ code reconstructions is the uncertainty of separatrix position at the outer midplane (OMP), whose effect on mapping profiles to the OMP is illustrated in figure 1a. It has been attempted to correct the reconstruction errors by calibrating the edge measurement position against the velocity shear layer (VSL) position instead of the EFIT separatrix [8, 9]. However, efforts to address the issue on the reconstruction level have until recently been lacking.

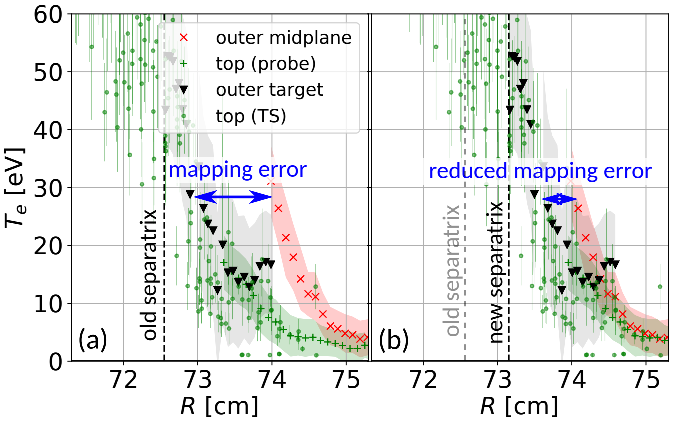

Figure 1. T_e profiles measured at the OMP (reciprocating probe), the plasma top (reciprocating probe and Thomson scattering [6]) and the outer divertor target (probe array [7]), discharge #15182. (a) Mapped to the OMP using the original EFIT reconstruction, (b) mapped to the OMP using the new reconstruction (section 2.1).

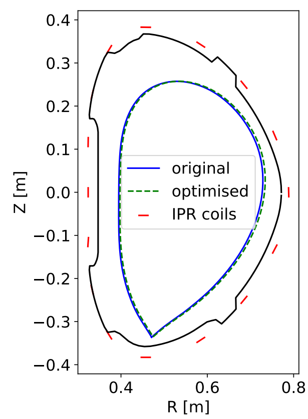

Figure 2. Location of IPR coils providing input data to EFIT, and reconstructions of discharge #15182 separatrix using original and optimised coil positions.

In a companion work [10], Kovanda et al. put forth that reconstruction uncertainties may be affected by inaccurate records of the measuring magnetic coil positions in EFIT input, and they subsequently provide corrected coil positions (detailed in section 2.1). In this article, we systematically benchmark the resulting "corrected" reconstructions by comparing the reconstructed OMP separatrix position to the VSL position detected by electrostatic probes in L-mode. Our goal is to demonstrate systematic differences between the separatrix and the VSL position in the old reconstructions, to show that their disparity depends mainly on plasma geometry, and to corroborate that correcting for the measuring coil geometry substantially reduces the dependency. In conclusion, we recommend that equilibrium reconstructions in all previous COMPASS discharges be retroactively recalculated using the corrected measuring coil positions, as the resulting reconstructions are likely more accurate than the ones in use today.

2 Methods

2.1 EFIT++

EFIT++ is a standard solver of the Grad-Shafranov equation [11]. In reconstructing COMPASS equilibria, local magnetic fields measured by 16 inner partial Rogowski coils (IPR coils) are provided to it as minimal constraining input. The IPR coils are small measuring coils distributed poloidally around the chamber (figure 2). It was recently found that their positions recorded within the EFIT input are inaccurate. [10] Synthetic coil signals calculated by the Biot-Savart law from poloidal field coil currents in the static phase of a vacuum discharge were compared to the measured coil signals, which betrayed disagreements up to $\sim 10\%$. To infer the coil positions more accurately, their R and Z coordinates and the poloidal angle θ were varied so as to achieve a fit between the measured and the calculated coil signal in each individual coil. The match was found to be especially sensitive to coil angles, which were on average corrected by several degrees (not visible in figure 2). Providing EFIT with the corrected coil positions can alleviate the mapping problems (figure 1b).

2.2 Velocity shear layer

The VSL is a region in the edge plasma where the poloidal plasma velocity v_p varies rapidly in the radial direction. The VSL has been shown to affect the magnitude of cross-field transport by regulating the level of plasma turbulence [12] and contributing to the L-H transition [13]. The origin of a steady-state VSL may be, in the first approximation, connected to the transition between closed and open magnetic field lines. As argued in [14], the interplay between the radial force balance (closed field lines) and the sheath potential drop (open field lines) causes the plasma potential Φ to peak near the separatrix, which results in a profile in the radial electric field $E_r = -d\Phi/dr$ and in the poloidal velocity $v_p = E_r \times B_t$ — that is, a VSL. This argumentation is rather crude, but despite that a Φ peak, or the corresponding $E_r = 0$, has been observed in experiment [13, 15], gyrofluid turbulence simulations [16], fluid simulations [17] and continuum kinetic simulations [18] alike.

Refer to [10] for discussion on additional constraining input and reconstruction settings in COMPASS EFIT.

The exact relation of the separatrix and the VSL position is currently unknown — some studies suggest that the VSL forms 0.5–1 cm outside the separatrix [4, 15, 16, 18, 19] while others place it up to 1 cm inside the separatrix [17, 20]. It is likely that their relative position depends on a number of factors, including the connection length, plasma collisionality, attachement/detachment and more. However, section 3 shows that, in original COMPASS reconstructions, $R_{\text{sep}} - R_{\text{VSL}}$

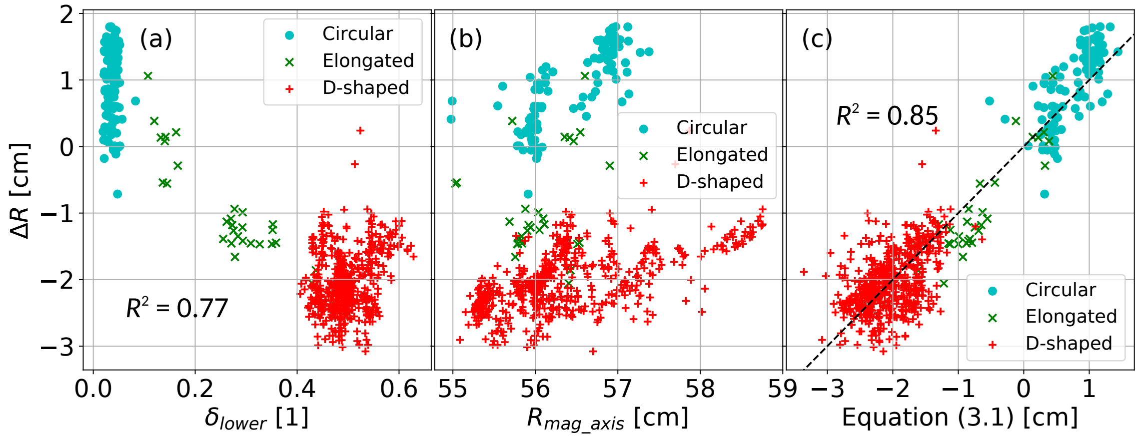

Figure 3. Dependency of $\Delta R = R_{\mathrm{sep}} - R_{\mathrm{VSL}}$ on (a) lower triangularity and (b) magnetic axis radial position, (c) linear regression using equation (3.1). Original EFIT reconstructions.

In this paper, we exploit the fact that COMPASS probes routinely record a Φ peak to carry out a statistical comparison of the VSL position to the magnetically reconstructed separatrix position.

2.3 Probes

The OMP reciprocating probe of the COMPASS tokamak [6] carries a ball pen probe, which is a Langmuir probe variation similar to the ion-sensitive probe both in design and measurement [22]. Its floating potential is close to the plasma potential, $V_{\mathrm{BPP}} = \Phi - (0.6 \pm 0.3)\, T_e$, and for the purposes of this article we assume them equal. A single ball-pen probe can detect the VSL centre (Φ peak) with a spatial uncertainty ±2 mm accounting for the smoothing and the neglected T_e contribution.

3 Results

In this section we present a statistical comparison of the EFIT separatrix radial position R_{sep} to the VSL position R_{VSL}, carried out over a database of 398 COMPASS discharges (53 circular, 19 elongated and 325 D-shaped plasmas). We investigate the difference $\Delta R = R_{\mathrm{sep}} - R_{\mathrm{VSL}}$.

Figure 3a shows that ΔR varies considerably across the COMPASS database, from −3 cm to +2 cm, and that this variation consists of a random component and a systematic component. To find which variables affect the systematic component, we evaluated the dependence of ΔR on the variables listed in table 1 using the Principle component analysis (PCA). We found the 5 largest principle components of the phase space, responsible for 91% of its variance, and with them acting as the independent variables we performed a linear regression of ΔR. The regression matched closely with the data, $R^2 = 0.86$. Subsequently, we transformed the principle components back into the variables of table 1, obtaining the coefficients listed in table 1. In the original EFIT reconstructions, ΔR is observed to depend most strongly on the plasma lower triangularity δ_{lower} and the magnetic

is dominated by geometric factors rather than plasma parameters, reaching values from −3 to +2 cm as opposed the considerably smaller numbers found in literature. And since this systematic dependency is substantially suppressed by correcting the coil positions, which is a purely geometric adjustment, we can surmise that EFIT input inaccuracies impact the interplay between the reconstructed separatrix and VSL position significantly more than physical mechanisms.

Table 1. Coefficients of ΔR linear fit using 5 largest principle components of the independent variable phase space: safety factor, magnetic axis radial and vertical position, elongation, upper and lower triangularity, plasma current, toroidal magnetic field, normalised beta, and the line-averaged plasma density.

EFIT	q_{95}	$R_{\text{mag\_axis}}$	$Z_{\text{mag\_axis}}$	ε	δ_{upper}	δ_{lower}	I_p	B_t	β_N	$\overline{n}_e$
original	−0.1	**0.5**	**−0.3**	0.09	**0.3**	**−1.3**	−0.03	0.03	**0.4**	0.01
new	−0.02	**0.2**	0.06	0.1	**−0.4**	−0.03	0.08	−0.07	**0.2**	−0.007

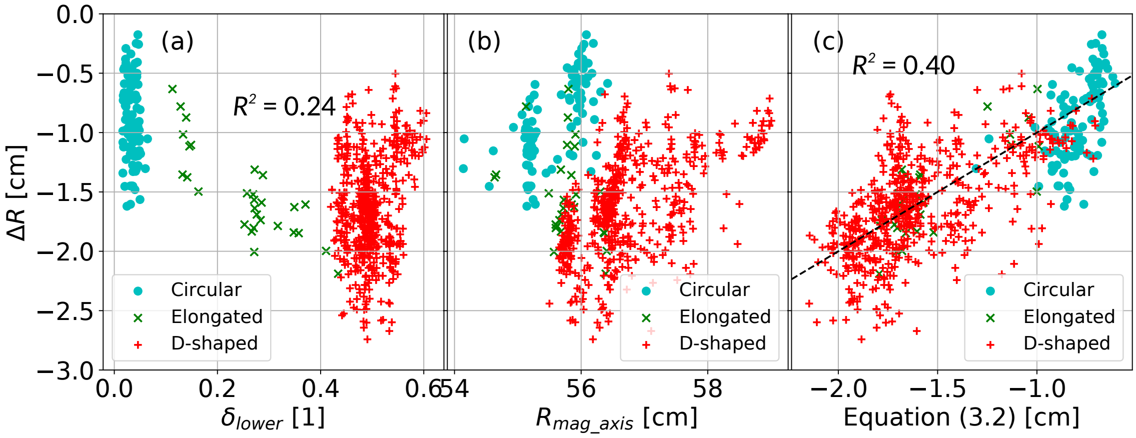

Figure 4. Dependency of $\Delta R = R_{\text{sep}} - R_{\text{VSL}}$ on (a) lower triangularity and (b) magnetic axis radial position, (c) linear regression using equation (3.2). New EFIT reconstructions.

axis radial position $R_{\text{mag\_axis}}$, which both relate to the plasma geometry. In figures 3a and 3b, one may observe both the dependencies. Finally, figure 3c shows the aforementioned linear regression with "reduced" variables — only the emboldened coefficients in table 1 were considered, that is,

$$\Delta R = -1.6 - 1.3\delta_{\text{lower}} + 0.5R_{\text{mag\_axis}} + 0.5\beta_N - 0.3Z_{\text{mag\_axis}} + 0.3\delta_{\text{upper}} \tag{3.1}$$

with an almost unchanged $R^2 = 0.85$. In figure 4, the same plots are presented for the new EFIT reconstructions. We see that purely geometrical adjustments to the EFIT input have a major impact on the reconstructed separatrix position. As observed in table 1, some dependency on triangularity and the magnetic axis position remains, but it is much less pronounced compared to the random error. The "reduced" linear regression of ΔR for the optimised EFIT is

$$\Delta R = -1.5 + 0.2\beta_N + 0.2R_{\text{mag\_axis}} - 0.4\delta_{\text{upper}}, \tag{3.2}$$

with $R^2 = 0.4$, which shows a significant suppression of the systematic component of ΔR.

4 Discussion and conclusions

We have compared the outer-midplane position of the magnetically reconstructed separatrix R_{sep} to the velocity shear layer (VSL) position R_{VSL} and drawn two conclusions: (i) current EFIT reconstructions contain a systematic error dependent on plasma geometry, and (ii) this error can be mitigated by correcting magnetic coil positions recorded in the EFIT input. It should be mentioned

2019 JINST 14 C11020

that although in previous works the VSL has been consistently associated with the separatrix, it is true that they may not coincide. In original COMPASS reconstructions, nevertheless, $R_{sep} - R_{VSL}$ is dominated by geometric factors to the point where other physical dependencies are relatively inconsequential. We thus recommend using the corrected coil positions as a solid step toward more reliable and accurate equilibrium reconstructions in COMPASS. Using this experience, similar problems can be avoided in the future COMPASS-Upgrade tokamak equilibrium reconstructions.

Acknowledgments

This work was carried out within the framework of the EUROfusion Consortium and has received funding from the Euratom research and training programme 2014–2018 and 2019–2020 under grant agreement No. 633053. The views and opinions expressed herein do not necessarily reflect those of the European Commission. This work was supported by the Grant Agency of the Czech Technical University in Prague, grant No. SGS19/180/OHK4/3T/14, project No. CZ.02.1.01/0.0/0.0/16_019/0000768, Czech Science Foundation grant No. GA19-15229S, and co-founded by MEYS projects number 8D15001 and LM2015045.

References

[1] A. Kallenbach, Y. Andrew, M. Beurskens, G. Corrigan, T. Eich, S. Jachmich et al., *EDGE2D modelling of edge profiles obtained in JET diagnostic optimized configuration*, *Plasma Phys. Control. Fusion* **46** (2004) 431.

[2] M. Kocan, R. Pitts, G. Arnoux, I. Balboa, P. de Vries, R. Dejarnac et al., *Impact of a narrow limiter SOL heat flux channel on the ITER first wall panel shaping*, *Nucl. Fusion* **55** (2015) 033019.

[3] B. LaBombard, J. Terry, J. Hughes, D. Brunner, J. Payne, M. Reinke et al., *Divertor heat flux footprints in EDA H-mode discharges on Alcator C-Mod*, *J. Nucl. Mater.* **415** (2011) S349.

[4] C.K. Tsui, J.A. Boedo, F.D. Halpern, J. Loizu, F. Nespoli, J. Horacek et al., *Poloidal asymmetry in the narrow heat flux feature in the TCV scrape-off layer*, *Phys. Plasmas* **24** (2017) 062508.

[5] G.D. Porter, J. Moller, M. Brown and C. Lasnier, *Characterization of the separatrix plasma parameters in DIII-D*, *Phys. Plasmas* **5** (1998) 1410.

[6] V. Weinzettl et al, *Progress in diagnostics of the COMPASS tokamak*, 2017 *JINST* **12** C12015.

[7] J. Adamek, J. Seidl, J. Horacek, M. Komm, T. Eich, R. Panek et al., *Electron temperature and heat load measurements in the COMPASS divertor using the new system of probes*, *Nucl. Fusion* **57** (2017) 116017.

[8] J. Seidl, J. Krbec, M. Hron, J. Adamek, C. Hidalgo, T. Markovic et al., *Electromagnetic characteristics of geodesic acoustic mode in the COMPASS tokamak*, *Nucl. Fusion* **57** (2017) 126048.

[9] J. Brotankova, J. Stockel, J. Horacek, J. Seidl, I. Duran, M. Hron et al., *Measurement of sheared flows in the edge plasma of the CASTOR tokamak*, *Plasma Phys. Rep.* **35** (2009) 980.

[10] O. Kovanda et al, *Dependence of reconstructed equilibiria on input data sets using EFIT on COMPASS and comparison with experimental observations*, talk given at the *46th EPS conference on plasma physics*, Milano, Italy, 8–12 July 2019

[11] L. Appel, M. Bevir and M. Walsh, *Equilibrium reconstruction in the START tokamak*, *Nucl. Fusion* **41** (2001) 169.

[12] S.K. Saha and R. Kumar, *Poloidal velocity shear and decorrelation of the edge fluctuations in tokamak*, in proceedings of the *30th International Conference on Plasma Science*, Jeju, South Korea, 5 June 2003, p. 469.

[13] G.R. Tynan, I. Cziegler, P.H. Diamond, M. Malkov, A. Hubbard, J.W. Hughes et al., *Recent progress towards a physics-based understanding of the H-mode transition*, *Plasma Phys. Control. Fusion* **58** (2016) 044003.

[14] K. Jirakova, *Study of edge plasma of tokamak COMPASS and its poloidal variations*, MSc thesis, Faculty of Nuclear Sciences and Physical Engineering, Czech Technical University, Czech Republic (2018), sections 3.1.2 and 3.1.5.

[15] T.D. Rognlien, D.D. Ryutov, N. Mattor and G.D. Porter, *Two-dimensional electric fields and drifts near the magnetic separatrix in divertor tokamaks*, *Phys. Plasmas* **6** (1999) 1851.

[16] P. Manz, T.T. Ribeiro, B.D. Scott, G. Birkenmeier, D. Carralero, G. Fuchert et al., *Origin and turbulence spreading of plasma blobs*, *Phys. Plasmas* **22** (2015) 022308.

[17] V. Rozhansky, S. Voskoboynikov, E. Kaveeva, D. Coster and R. Schneider, *Simulation of tokamak edge plasma including self-consistent electric fields*, *Nucl. Fusion* **41** (2001) 387.

[18] M. Dorf and M. Dorr, *Continuum kinetic modelling of cross-separatrix plasma transport in a tokamak edge including self-consistent electric fields*, *Contrib. Plasma Phys.* **58** (2018) 434.

[19] B. Nold, G.D. Conway, T. Happel, H.W. Müller, M. Ramisch, V. Rohde et al., *Generation of blobs and holes in the edge of the ASDEX upgrade tokamak*, *Plasma Phys. Control. Fusion* **52** (2010) 065005.

[20] G. Xu, V. Naulin, W. Fundamenski, C. Hidalgo, J. Alonso, C. Silva et al., *Blob/hole formation and zonal-flow generation in the edge plasma of the JET tokamak*, *Nucl. Fusion* **49** (2009) 092002.

[21] A. Field, G. Fussmann and J. Hofmann, *Measurement of the radial electric field in the ASDEX tokamak*, *Nucl. Fusion* **32** (1992) 1191.

[22] J. Adámek, J. Stöckel, M. Hron, J. Ryszawy, M. Tichý, R. Schrittwieser et al., *A novel approach to direct measurement of the plasma potential*, *Czech. J. Phys.* **54** (2004) C95.

[23] J. Adamek, H.W. Müller, C. Silva, R. Schrittwieser, C. Ionita, F. Mehlmann et al., *Profile measurements of the electron temperature on the ASDEX upgrade, COMPASS, and ISTTOK tokamak using Thomson scattering, triple, and ball-pen probes*, *Rev. Sci. Instrum.* **87** (2016) 043510.

Appendix B

List of COMPASS diagnostics

Diagnostic name	Measured quantities	Responsible person	Description	Useful for SOLPS-ITER?
Magnetic coils	B		"Set of several full poloidal rings of magnetic coils, about 300 diagnostic coils from 440 magnetic sensors available in total are routinely connected to data acquisition channels"	unimportant
Probes in the central column			scarcely used (2014-15)	could be used
Vertical reciprocating probe	Phi, T_e, n_e, q_||	Petr Vondráček, Miglena Dimitrova	plasma top, does not work very often, known to cool the edge plasma	could be used
Horizontal reciprocating probe	Phi, T_e, n_e, q_||	Jiří Adámek	outer midplane, works somewhat often, dedicated campaigns	crucial for OMP transport
"New" divertor probe array	Phi, T_e, n_e, q_||	Jiří Adámek	both divertor targets but works well only on the outer, routine measurements	important for divertor heat fluxes
"Old" divertor probe array	T_e, n_e, q_||	Miglena Dimitrova	both divertor targets, but the FDPT has been discredited; request data from Megi and use with caution	important for divertor heat fluxes
Pecker probe 1 & 2	I_sat, Mach number		poloidally between HRCP and VRCP, and between HRCP and divertor, not much data	could be used
U-probe	B, Phi, T_e, n_e, q_||	Karel Kovařík	big and bulky, has been smitten by the plasma more than once	could be used
Retarding field analyser (RFA)	T_e, n_e, T_i, Mach number	Michael Komm	can be embedded in the central column or mounted on a reciprocating manipulator	could be used
Two B/W cameras	visible radiation			not very important
Two colour cameras	visible radiation		"Photron FASTCAM Mini UX100 (1280 × 1024 px @ 4 kfps, 640 × 8 px @ 800 kfps), usually equipped with the endoscope consisting of a wide angle lens (e.g. f = 4.8 mm) to obtain an overview of the vacuum vessel (reaching up to 180° is possible)"	not very important
B/W Photron FASTCAM cameras	visible radiation		can resolve ELMs	not very important
Two infrared cameras	q_||	Petr Vondráček	"The slow Micro-Epsilon TIM-160 is equipped with a bolometric detector (7.5–13 μm, 160 × 120 px @ 120 Hz), the fast camera Telops Fast-IR 2K has an InSb detector (3–5 μm, 320×256 px @ 1.9 kHz, 64×4 px @ 90 kHz). The cameras could be placed to various torus locations securing an observation of the central column limiters (0.5 mm/px) for SOL heat flux studies [8, 29], of the low field side protection limiter (1 mm/px) for runaway studies [27] or of the divertor region (0.5–1.5 mm/px will be reached using a newly developed IR endoscope), where a new graphite divertor tile optimised for IR thermography in ELMy H-mode will be placed (optimized magnetic field incidence angles, embedded tile heating and bulk temperature measurement) [30]."	important for divertor heat fluxes
Thomson scattering	T_e, n_e	Petr Böhm	chord goes vertically through plasma top, one system for core, another dedicated to edge, lately very good data quality, usually available	crucial for n_sep
Interferometer	line-averaged n_e	Ondrej Bogar	usually available	not as important as edge n_e profiles
Tomography from bolometers and from X-rays		Martin Imríšek, Jan Mlynář, Jakub Svoboda, Ondřej Ficker		critical for P_rad and P_SOL estimation, comparison of bolometer line-of-sight with code results
BES		Pavel Háček, Jaroslav Krbec	lithium beam	useful for additional n_e profile
Neutral particle analyser (NPA)	IEDF, T_i	Matej Tomes, Klara Mitosinkova	some neutral particles come from the core, which we don't simulate; can be compared to EIRENE results in charge-exchange neutrals	some neutral particles come from the core, which we don't simulate; can be compared to EIRENE results in charge-exchange neutrals
Neutron detectors	neutron flux		one scintillator, two 3He proportional counters	unimportant
Cherenkov detector	X-rays		for runaway studies	unimportant
CXRS	v_tor, T_i	Matěj Tomeš	"CXRS is not and never will be avaliable on COMPASS."	would be a work horse if it measured in the edge plasma
C-III line spectroscopy	v_pol, T_i	Diana Naydenková	not sure if it works	would be very useful (H_aplha, C-II, C-III)
ECE	T_e		not present	would be very useful

Figure B.1: List of COMPASS diagnostics according to [22]. Diagnostics marked in green routinely provide data of high quality. Diagnostics marked in red are imperative for SOLPS-ITER modelling.